Title
High-performance Semipolar GaN/InGaN light emitting devices with surface gratings

Author
Zhang, Haojun

Publication Date
2020

UNIVERSITY OF CALIFORNIA

Santa Barbara

Semipolar GaN/InGaN light emitting devices with surface gratings

A dissertation submitted in partial satisfaction of the
requirements for the degree Doctor of Philosophy
in Electrical and Computer Engineering

by

Haojun Zhang

Committee in charge:

Professor Steven P. DenBaars, Chair
Professor Jonathan Klamkin
Professor Umesh Mishra
Professor Shuji Nakamura

December 2020

The dissertation of Haojun Zhang is approved.

Jonathan Klamkin

Umesh Mishra

Shuji Nakamura

Steven P. DenBaars, Committee Chair

December 2020

[This page is optional]

Semipolar GaN/InGaN light emitting devices with surface gratings

by

Haojun Zhang

[This page is optional]

ACKNOWLEDGEMENTS

My past seven years at UCSB is not an easy journey, and I am indebted to so many people for helping me along my journey to this destination. I have to first thank my doctoral committee, and first my advisor, Professor Steven DenBaars, for giving me the opportunity to work in his research group and providing all kinds of resources for all of his students to thrive and succeed. I would also like to thank Prof. Shuji Nakmura for his valuable advice and guidance on every corner of my research, which has also inspired me to be a better researcher. I owe great thanks to Prof. Umesh Mishra for serving on my committee. His class has laid a solid foundation of my research and without the crucial knowledge and skills learned from there it would be almost impossible to start anything. Finally I would like to thank Prof. Jonathan Klamkin for helping me understand many critical questions about optical systems and his questions and deep understanding of the big picture has enabled me to smoothly go through some of the most difficult parts of the dissertation.

In addition, I must thank Dr. Daniel Cohen for helping me to plan, practice and finish up all the way from the very beginning of this research journey. His dedication and enthusiasm and deep knowledge have truly impressed me, and it was under his guidance that I brought such work to fruition.

The work presented here will also be impossible from the help and support from the entire SSLEEC group and all the administrative staff, especially those folks who have keep me company through the ups and downs, Dr Daniel Becerra, Dr. Shlomo Mehari, Philip Chan, Shereen Hamdy, Ryan Anderson, Matt Wong, Joonho Back and Dr. Hongjian Li.

The standard of the research facilities that we rely on here at UCSB are without question top-notch, and I would like to thank the incredibly helpful research staff for always doing their best to keep research moving smoothly almost 24/7. Those names include Dr. Stacia Keller, Mike Iza, Dr. Brian Thibeault, Dr. Bill Mitchell and Aidan Hopkins.

I would also like to thank many of my friends and spiritual mentors across the states and Canada. Their encouragement and support meant so much to me. This pandemic has reshaped the world deeply. I am fortunate and truly grateful that I can finish this very important part of my life without too much stress and anxiety because of their enormous care and love.

Finally, my family has always been there for me no matter how the world outside has changed. I know their high expectation of me, and I hope that my achievements so har has not let them down.

Haojun Zhang
E-mail: hzhang@ucsb.edu

EDUCATION

University of California, Santa Barbara
♦ Ph.D. in Electrical and Computer Engineering 2020
Tsinghua University, China
♦ B.S. in Electrical Engineering 2013

TECHNICAL SKILLS

- Material characterization skills: **SEM, AFM, XRD, SIMS**
- Advanced lithography skills: **Electron-beam Lithography, Interference Lithography**
- Epitaxial structure optimization of semipolar III-nitride LEDs and laser diodes
- Programming Language: **C++, Python, Matlab, Mathematica**
- Design of Experiments (DOE): **Labview**
- Optical Modeling, Photonics and Thermal Simulation: **LightTools, Lumerical**
- First-principle Simulation: **Quantum Espresso**

RESEARCH & WORK EXPERIENCE

1. R&D of high-power **blue laser diodes** with **surface grating** and high-performance facet coatings for atomic clocks and quantum computing

Designed and fabricated high-power blue DFB lasers with **first and third order** surface gratings on III-nitride systems.

Solid State Lighting & Energy Electronics Center (SSLEEC), UC Santa Barbara 2016-2020

2. R&D of low-cost high-polarization-ratio dual-color InGaN micro-LEDs with surface gratings

Designed, fabricated and tested monolithic surface grating enhanced semipolar InGaN green and white μLEDs for backlighting LCD displays.

Solid State Lighting & Energy Electronics Center (SSLEEC), UC Santa Barbara 2018-2020

3. R&D of visible III-V photonic integrated circuits

Optimizing the design and simulation of Electro-absorption modulator and Semiconductor Optical Amplifier (SOA) waveguide for **high-speed** high power **laser communication** and **li-fi systems**.

Solid State Lighting & Energy Electronics Center (SSLEEC), UC Santa Barbara 2019-2020

4. First principle simulation and cryogenic testing of two dimensional material transistors

First-principle **simulation, fabrication and testing** of multiple **2D tunneling field-effect transistors** (graphene/MoS_2/WSe_2)

Nanoelectronics Research Lab, UC Santa Barbara 2014-2016

SELECTED PUBLICATIONS AS FIRST OR CORRESPONDING AUTHOR

1. **Zhang, H.**, Zhu, M., Sensale-Rodríguez, B. and Xing, H.G., 2013, April. THz plasmonic absorption in periodically patterned semiconductor ribbons. 2013 *IEEE International Wireless Symposium* (IWS) (pp. 1-3). IEEE.
2. **Zhang, H**., Cao, W., Kang, J. and Banerjee, K., 2016, December. Effect of band-tails on the subthreshold performance of 2D tunnel-FETs. *2016 IEEE International Electron Devices Meeting* (IEDM) (pp. 30-3). IEEE.
3. **Zhang, H.**, Cohen, D.A., Chan, P., Wong, M.S., Mehari, S., Becerra, D.L., Nakamura, S. and DenBaars, S.P., 2019. Continuous-wave operation of a semipolar InGaN distributed-feedback blue laser diode with a first-order indium tin oxide surface grating. *Optics letters*, 44(12), pp.3106-3109.
4. **Zhang, H.**, Li, H., Li, P., Song, J., Speck, J. S., Nakamura, S., & DenBaars, S. P. (2020). Room-Temperature Continuous-Wave Electrically Driven Semipolar $(20\bar{2}1)$ Blue Laser Diodes Heteroepitaxially Grown on a Sapphire Substrate. *ACS Photonics*, 7(7), 1662-1666.
   Featured in Semiconductor's Today
5. **Zhang, H.**, Cohen, D., Chan, P., Wong, M.S., Mehari, S., Nakamura, S. and DenBaars, S.P., 2020, February. Semipolar group III-nitride distributed-feedback blue laser diode with Indium tin oxide surface grating. In Novel In-Plane Semiconductor Lasers XIX (Vol. 11301, p. 1130102). *International Society for Optics and Photonics*.
6. **Zhang, H.**, Cohen, D. A., Chan, P., Wong, M. S., Li, P., Li, H., ... & Denbaars, S. P. (2020). High performance of a semipolar InGaN laser with a phase-shifted embedded hydrogen silsesquioxane (HSQ) grating. *Optics Letters*, 45(20), 5844-5847.
7. **Zhang, H.**, Li, P., Li, H., Song, J., Nakamura, S., & DenBaars, S. P. (2020). High polarization and fast modulation speed of dual wavelengths electroluminescence from semipolar (20-21) micro light-emitting diodes with indium tin oxide surface grating. *Applied Physics Letters*, 117(18), 181105.
   Editor's choice
8. **Zhang, H.**, Li, H., Li, P., Nakamura, S. and DenBaars, S.P., 2020. Analysis of temperature-dependent electroluminescence properties of heteroepitaxial semipolar (20-21) blue laser diodes. *Being reviewed in Optics Letters*.
9. Li, H., Li, P., **Zhang, H.***, Nakamura, S. and DenBaars, S.P., 2020. Demonstration of efficient semipolar 410 nm violet laser diodes heteroepitaxially grown on high-quality low-cost GaN/sapphire substrates. *ACS Applied Electronic Materials*. 2(7), 1874-1879.

OTHER SELECTED IMPORTANT PUBLICATIONS

10. Li, P., **Zhang, H.**, Li, H., Iza, M., Yao, Y., Wong, M.S., Palmquist, N., Speck, J.S., Nakamura, S. and DenBaars, S.P., 2020. Size-independent low voltage of InGaN micro-

light-emitting diodes with epitaxial tunnel junctions using selective area growth by metalorganic chemical vapor deposition. *Optics Express, 28(13)*, pp.18707-18712.

11. Li, H., **Zhang, H.**, Li, P., Wong, M, Chow, Y, Pinna, S, J.S., Nakamura, S. and DenBaars, S.P. 2020. Development of efficient semipolar InGaN long wavelength light-emitting diodes and blue laser diodes grown on high quality semipolar GaN/sapphire template. *Journal of Physics, Photonics.*
12. Li, P., **Zhang, H.**, Li, H., Zhang, Y., Yao, Y., Palmquist, N., ... & DenBaars, S. P. (2020). Metalorganic chemical vapor deposition grown n-InGaN/n-GaN tunnel junctions for micro-light-emitting diodes with very low forward voltage. *Semiconductor Science and Technology*, 35(12), 125023.
13. Li, H., Li, P., **Zhang, H.**, J.S., Nakamura, S. and DenBaars, S.P. 2020. Electrically driven, polarized, phosphor-free white semipolar (20-21) InGaN light-emitting diodes grown on semipolar bulk GaN substrate. *Optics express*, 8, 13569-13575
14. Sarkar, D., Xie, X., Kang, J., **Zhang, H.**, Liu, W., Navarrete, J., Moskovits, M. and Banerjee, K., 2015. Functionalization of transition metal dichalcogenides with metallic nanoparticles: implications for doping and gas-sensing. *Nano letters*, 15(5), pp.2852-2862.
15. Khoury, M., Li, H., **Zhang, H.**, Bonef, B., Wong, M.S., Wu, F., Cohen, D., De Mierry, P., Vennéguès, P., Speck, J.S. and Nakamura, S., 2019. Demonstration of Electrically Injected Semipolar Laser Diodes Grown on Low-Cost and Scalable Sapphire Substrates. *ACS applied materials & interfaces*, 11(50), pp.47106-47111.
16. Lheureux, G., Mehari, S., Cohen, D., Chan, P., **Zhang, H.**, Hamdy, K., ... & Margalith, T. (2019, July). GaN High-Power Lasers for solid-state lighting. In *Optical Devices and Materials for Solar Energy and Solid-state Lighting* (pp. PT2C-1). Optical Society of America.
17. Mehari, S., Cohen, D. A., Becerra, D. L., **Zhang, H.**, Weisbuch, C., Speck, J. S., ... & DenBaars, S. P. (2019, March). Semipolar III-nitride laser diodes for solid-state lighting. In *Novel In-Plane Semiconductor Lasers XVIII* (Vol. 10939, p. 109390G). International Society for Optics and Photonics.
18. Jiang, J., Kang, J., Cao, W., Xie, X., **Zhang, H.**, Chu, J. H., ... & Banerjee, K. (2017). Intercalation doped multilayer-graphene-nanoribbons for next-generation interconnects. *Nano letters*, *17*(3), 1482-1488.
19. Khoury, M., Li, H., Li, P., Chow, Y. C., Bonef, B., **Zhang, H.**, ... & Speck, J. S. (2020). Polarized monolithic white semipolar (20–21) InGaN light-emitting diodes grown on high quality (20–21) GaN/sapphire templates and its application to visible light communication. *Nano Energy*, *67*, 104236.

SELECTED CONFERENCES AND TALKS

1. Invited presentation at SPIE Photonics West 2020, San Francisco, February 2020
2. Invited presentation at NanoTech, UC Santa Barbara, December 2019
3. Presentation at 13th International Conference on Nitride Semiconductors (ICNS), Seattle, July 2019
4. Presentation at 2016 IEEE International Electron Devices Meeting (IEDM), San Francisco, December 2016

PATENTS

1. UC 2019-402, DISTRIBUTED FEEDBACK LASER WITH TRANSPARENT CONDUCTING OXIDE
2. UC 2019-406, LASER RIDGE ON SEMIPOLAR GAN ON SCALABLE SAPPHIRE SUBSTRATES
3. UC 2019-938, LASER DIODE WITH CONTACT SURFACE GRATING

MEDIA COVERAGE

http://www.semiconductor-today.com/news_items/2020/aug/ucsb-060820.shtml

---

AWARDS

2018 UCSB SSLEEC Outstanding Graduate Research Award
2011 National Award in Annual Physics Contest, Beijing, China

ABSTRACT

High-performance Semipolar GaN/InGaN light emitting devices with surface gratings

by

Haojun Zhang

The impact of III-Nitride material and solid-state lighting on the world has been far-reaching. The last decade has seen the III-Nitride LEDs and laser didoes (LDs) steadily becoming essential components in a broad range of applications. Compared with traditional lighting systems, their great improvement in efficiency and portability for lighting systems, the reduced environmental impact as well as the potentials for the future visible light communication systems is profound.

Properly engineered distributed feedback (DFB) laser diodes (LDs) are well known for their excellent portability, easy integration, and ability to offer robust single longitudinal mode stability. Among them, III-nitride material based visible DFB-LDs are gaining special attention due to many emerging applications such as atomic clocks, medical sensing, laser cooling and visible light communication. Previous GaN DFB-LDs have been conventionally fabricated with epitaxially buried gratings, which is often difficult and costly. In this dissertation, the design of DFB-LDs with a novel surface grating structure and their enhanced performance will be presented. Starting with the design and optical simulation of the devices, continuing through nanofabrication and testing, major parts and analysis of these novel III-nitride devices with surface gratings will be discussed. We show that under continuous-wave operation, the 445 nm laser diode with a uniform first-order etched surface grating emits with

a FWHM (full width half maximum) of 5 pm, SMSR (side mode suppression ratio) of more than 25 dB and output power of more than 80 mW from a single facet. Moreover, an enhanced performance has been also achieved in laser diodes with phase-shifted third-order non-etched hydrogen silsesquioxane (HSQ) gratings. These improved single-mode blue lasers achieve a high output power, SMSR of more than 35 dB and FWHM of less than 2 pm even under high current injection.

In addition to the DFB-LDs, surface gratings have also been historically employed in many other optical and photonic devices as an approach to realize novel functions. Efficient polarized light source, as a key component in mainstream LCD displays, plays an important role in energy saving. Specifically, in this dissertation, we also demonstrate that, by combining an ITO surface grating and Al surface coating, a highly polarized dual-wavelength semipolar InGaN micro-LED can be achieved. Such devices exhibit a 1.7-fold enhancement of the polarization ratio as compared to the conventional semipolar micro-LEDs.

[This page is optional]

TABLE OF CONTENTS

I. Introduction

I. Introduction

A. GaN basics

III-nitride materials have gained much attention through the years. [1-4] With broadly tunably bandgap, III-nitride semiconductors have made possible some of the most important applications of this decade including deep UV, near UV, violet, blue, and green light-emitting diodes (LEDs) and laser diodes (LDs) while almost no other semiconductor materials system of any kind is able to cover a similar range of the spectrum. In addition, with a combination of high electron mobilities, high electron velocities, III-nitride semiconductors are good candidates in high-power high-frequency electronic devices. [5]

Before the discoveries of nitride semiconductors, efficient blue LDs were very rare. Blue-green light traditionally could be traditionally generated from ZnSe-based semiconductor materials and the first laser diodes based on ZnSe were first demonstrated in 1991 by Haase et al. [6] However, the short lifetimes and the relatively small bandgaps from II-VI materials due to the ease of dislocation generation in II-VI materials, limits the performance of high-efficiency devices.[7] In 1998 their lifetimes still remained poor for commercial applications. On the contrast, in the first GaN-based semiconductor laser diodes demonstrated in 1996 [8], more 10,000 hour lifetimes were achieved in 1997 and they were also commercially available in 1999. Another solid-state solution for blue LDs is the frequency doubling of semiconductor infrared laser diodes by nonlinear crystals [9]. This can provide high power emission in the blue [10, 11]. However, the cost, size and complexity of the systems is increased over semiconductor laser diodes [12]. Up-conversion by multi-photon pumping of an atomic system can also result in blue light emission [13, 14] which can be realized by optical pumping of a rare-earth doped fiber [15-16]. It also has increased cost and size over semiconductor LDs. This has all changed over the last two decades with the development of III-nitride-based materials and devices. GaN high electron mobility transistors (HEMTs) are already being utilized in microwave and mm-wave communications systems. [17] Blue and green III-nitride LEDs are widely employed in full-color outdoor displays and other signage applications, such as green traffic lights. Likewise, white LEDs based on blue III-nitride LEDs combined with yellow phosphors are being used as backlights in electronic devices as well as automotive, indoor, and outdoor lighting applications. [18] In addition, violet III-nitride LDs are already being widely used for high-capacity optical data storage, [19] while blue and green III-nitride LDs are poised for widespread use in laser-based projection displays. [20-21]

Current most of the state-of-the-art III-nitride devices are grown along the *c*-axis of the wurtzite crystal structure. Due to the absence of inversion symmetry in the wurtzite crystal structure, both spontaneous and piezoelectric polarization fields exist parallelly to the *c*-axis.[22] The *c*-plane, which is depicted in the wurtzite GaN unit cell shown in Fig. 1.1(a, b), is composed of alternating layers of Ga and N atoms. Each unit cell consists of a charge dipole arising from the displacement of the Ga and N atoms, as illustrated in Fig. 1.1(b). When III-nitride heterostructures are grown along the *c*-axis, the dipoles of every layer of unit cells neutralize each other in the bulk, but fixed sheet charges form at surfaces and interfaces within the crystal where there are discontinuities in the net polarization. These fixed sheet charges lead to the accumulation carriers at interfaces of each layers of Ga and N atoms and thus the

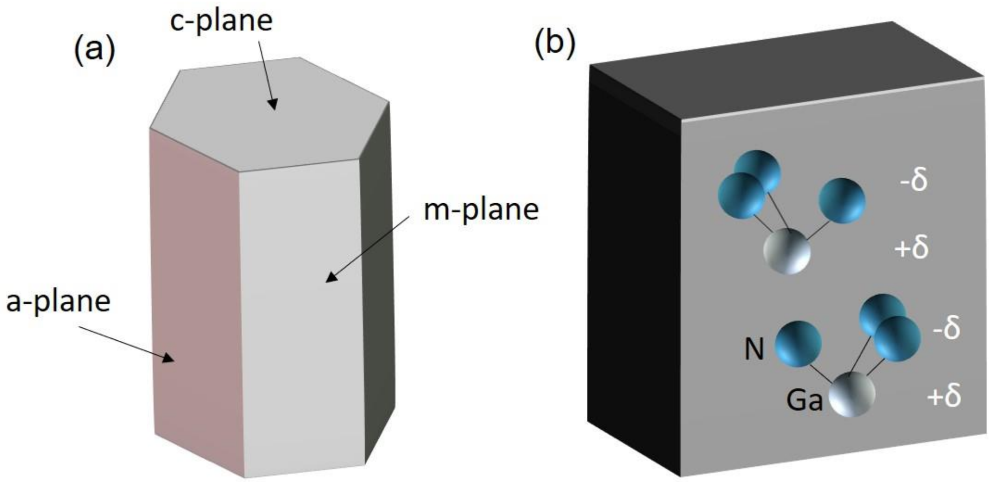

FIG. 1.1. (a) Schematic of the unit cell for wurtzite GaN showing the several planes. (b) The ball-and-stick model depicting the alternating layers of Ga and N atoms in the wurtzite GaN crystal structure.

generation of polarization fields. On conventional c-plane, since the direction of these polarization-induced electric fields is the same as the typical growth direction of III-nitride heterostructures, these fields have the effect of "tilting" the energy bands of III-nitride devices.

One popular approach to eliminate polarization effects is to grow the devices on nonpolar orientations and the main reason is that on such planes there are equal numbers of gallium and nitrogen atoms therefore there is no internal charge. For *c*-plane III-nitride electronic devices, polarization can be sometimes considered as useful since it gives rise to two-dimensional electron gases (2DEGs) with large sheet concentrations.[23] In *c*-plane III-nitride optoelectronic devices, however, the polarization-related electric fields tilt the energy bands inside the active region and spatially separate the electron and hole wavefunctions, as illustrated in Fig. 1.2. This spatial charge separation reduces the oscillator strength of radiative transitions and red-shifts the emission wavelength. Additionally, the large polarization-induced fields can be partially screened by injected carriers, leading to a blue-shift of the emission wavelength with

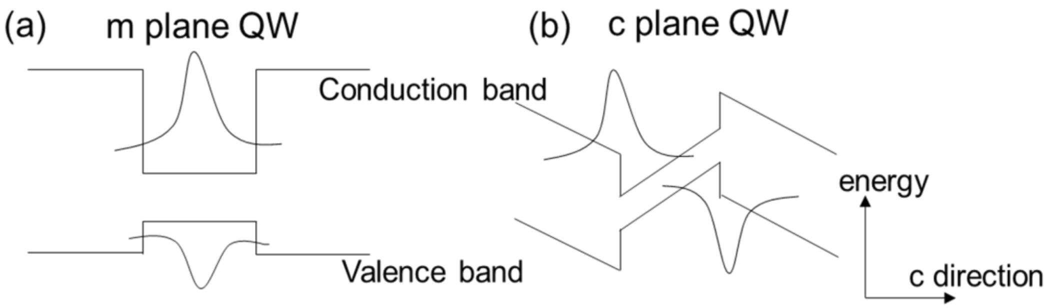

FIG. 1.2. (left image) Schematic of the band profile and the electron and hole wavefunctions for a nonpolar *a*- or *m*-plane QW. (right image) Schematic of the band profile and the electron and hole wavefunctions for a polar *c*-plane QW.

increasing drive current. [24,25] These effects show that the quantum-confined Stark effect (QCSE) [26,27] and have been thoroughly analyzed for III-nitride quantum wells (QWs). [28-41]

Normally on nonpolar layers the material will not be polarized along the growth direction. Thus, the energy bands inside the active region will not be tilted and the electron and hole wavefunctions will at the same position, as illustrated in Fig. 1.2, which enhances the radiative recombination rate and reduce the emission wavelength blue-shift as the drive current increases. Moreover, that uniaxial biaxial in-plane strain, such as that present in strained nonpolar or semipolar orientations, [42] should be very important for further improving the valence band DOS for III-nitride heterostructures. [43] Studies have therefore predicted that the performance and efficiency of III-nitride LDs should improve by growing the devices on nonpolar or semipolar orientations. [39-43]

B. History of Development of GaN Light emitting devices

A LED consists of a semiconductor p-n junction where electrons and holes will recombine to emit light of a particular bandgap corresponding to the bandgap of the material. The first LED was demonstrated by Holonyak with an emission at 710 nm in 1962 based on GaAsP.

[44] Semiconductor lasers were also first demonstrated in 1962 by several groups [47]. These initial demonstrations were GaAs homojunction in-plane laser diodes. In 1963, the idea about the double heterostructure laser design was initiated and such design by combining both optical and electrical confinement have greatly improved the performance [45] of the device. Emission wavelengths have been mostly focused on the long range since GaAs-based and InP-based semiconductors have received most attention because of the availability of high quality, low cost GaAs and InP substrates. Longer wavelength LEDs were also demonstrated up to the green range, but the blue had been difficult for many years. In the early 90s, a breakthrough was made when Shuji Nakamura demonstrated the first blue LED by using InGaN.[45] Once shown successful, the developments in InGaN LEDs started to grow fast. The use of a p-i-n diode structure with quantum wells (QWs) as the active region to further confine carriers led to greatly improved performance. The white LED lights were successfully demonstrated by combining the blue LED with a yellow emitting phosphor. Such LEDs also exhibited high efficiencies. Although, the color gamut was not ideal, improvement of the quality of the light color can be expected by using multiple different colors of LEDs.

Compared to the LEDs, the expansion of semiconductor laser diodes into the visible spectrum has been delayed due to difficulty in materials development. Traditional c-plane laser diodes met with great obstacles when pushing into long wavelength emission. During the summer and fall of 2006, a breakthrough occurred in the nonpolar and semipolar field. [48-52] Mitsubishi Chemical Corporation (MCC) and Furukawa Company, Ltd. were able to fabricate free-standing nonpolar and semipolar GaN substrates by cutting grown thick c-plane GaN crystals into desired orientations. In June 2006, researchers at Nichia reported milliwatt-level blue, green, and amber LEDs on free-standing semipolar GaN substrates provided.

Several years later more researchers at Rohm reported milliwatt-level blue LEDs on free-standing *m*-plane GaN substrates.[53] Starting from November 2006 researchers at UCSB also started to study the devices on nonpolar and semipolar free-standing GaN substrates provided by MCC. Within a year many good results had already come out from these semipolar or nonpolar devices. [54] These exciting LED results were soon transformed into lasers, which has continuously gained large amount of attention thoughout recent years.[55–79]

Out of many important applications, a major one of GaN lasers is laser based lighting systems, of which the idea is to use a laser instead of an LED to illuminate a phosphor. In the field of illumination, III-nitride laser diodes are mostly applications requiring directional illumination, such as mood lighting for large outdoor displays, directional lighting for industrial agriculture, or high-beam car headlights. Compared to LEDs, laser diodes do not face efficiency droop and thus have the benefits of increased efficiency at high current density and a lower form factor than LEDs that can realize lower cost. Its faster modulation speed also makes it very advantageous in Li-Fi applications.

While on the other side, DFB laser diodes have been developed many years ago on other III-V material system, its development on III-nitride materials has been long delayed due to the absence of useful applications-people generally do not need a single wavelength source for lighting uses. Recently, III-nitride materials system based distributed feedback laser diodes (DFB-LD) are gaining attention due to many emerging applications [80–84] in atomic clocks, medical sensing, laser cooling, visible light communications (VLC), and master oscillator power amplifier (MOPA) systems. These applications benefit from single frequency operation, precise wavelength tuning, and high output power afforded by a DFB-LD [85], as well as the improvements in efficiency, size, cost, and reliability compared to current approaches based on expensive and bulky external cavity or Ti-Sapphire solid-state lasers.

C. Dissertation overview

III-nitride material has deeply changed the way we think of visible light, and advances in this field are rapidly moving forward. The goal of the dissertation was to improve the efficiency and performance of light emitting devices based on GaN, with the uses of grating structure. Chapter 2 will discuss the basics of semipolar GaN lasers in detail and the optimized structure on which we based our work. In the first major parts, we will focus on our previously optimized design and characterization of semipolar GaN/InGaN through the years. A significant portion of the later chapters is inspired by the advancements that have occurred since that time. The purpose of Chapter 2 is to also review early processes and device results to provide a context for more recent accomplishments and advancements. Different waveguide designs and processes are presented and the benefits and drawbacks of each are compared.

Chapter 3 will discuss first-generation semipolar DFB-LD with surface gratings by etching the ITO layer. Limitations of the early processes are identified and presented to provide motivation for the development of more advanced processes. Emphasis is placed the development of device fabrication technologies, as these efforts have formed an integral and enabling part of this work and the work of others at the university. Chapter 4 will introduce an improved version of the DFB-LD design with imbedded grating design and compare it with previous structures as well as high-frequency analysis. Chapter 5 discusses a novel LED structure with surface gratings for high polarization emission uses.

References

1. S. Nagahama, Y. Sugimoto, T. Kozaki, and T. Mukai, *Proc. SPIE*, **5738**, 57 (2005).
2. T. Miyoshi, T. Yanamoto, T. Kozaki, S. Nagahama, Y. Narukawa, M. Sano, T. Yamada, and T. Mukai, *Proc. SPIE*, **6894**, 689414 (2008).
3. M. A. Khan, M. Shatalov, H. P. Maruska, H. M. Wang, and E. Kuokstis, *Jpn. J. Appl. Phys., Part 1*, **44**, 7191 (2005).
4. M. S. Shur, *Solid-State Electron.*, **42**, 2131 (1998).
5. U. K. Mishra, L. Shen, T. E. Kazior, and Y. F. Wu, *Proc. IEEE*, **96**, 287 (2008).
6. M. Razeghi and A. Rogalski, *J. Appl. Phys.*, **79**, 7433 (1996).
7. Y. Enya, Y. Yoshizumi, T. Kyono, K. Akita, M. Ueno, M. Adachi, T. Sumitomo, S. Tokuyama, T. Ikegami, K. Katayama, and T. Nakamura, *Appl. Phys. Express*, **2**, 082101 (2009).
8. N. Grandjean, B. Damilano, S. Dalmasso, M. Leroux, M. Laugt, and J. Massies, *J. Appl. Phys.*, **86**, 3714 (1999).
9. A. Avramescu, T. Lermer, J. Muller, C. Eichler, G. Bruederl, M. Sabathil, S. Lutgen, and U. Strauss, *Appl. Phys. Express*, **3**, 061003 (2010).
10. D. A. B. Miller, D. S. Chemla, T. C. Damen, A. C. Gossard, W. Wiegmann, T. H. Wood, and C. A. Burrus, *Phys. Rev. Lett.*, **53**, 2173 (1984).

11. J. Wu, W. Walukiewicz, K. M. Yu, W. Shan, J. W. Ager, E. E. Haller, H. Lu, W. J. Schaff, W. K. Metzger, and S. Kurtz, *J. Appl. Phys.*, **94**, 6477 (2003).

12. O. Ambacher, J. Smart, J. R. Shealy, N. G. Weimann, K. Chu, M. Murphy, W. J. Schaff, L. F. Eastman, R. Dimitrov, L. Wittmer, M. Stutzmann, W. Rieger, and J. Hilsenbeck, *J. Appl. Phys.*, **85**, 3222 (1999).

13. N. Okada, K. Uchida, S. Miyoshi, and K. Tadatomo, Phys. Status Solidi (a) 209, 469 (2012).

14. H. Li, M. Khoury, B. Bonef, A.I. Alhassan, A.J. Mughal, E. Azimah, M.E.A. Samsudin, P.D. Mierry, S. Nakamura, J.S. Speck, S.P. DenBaars, ACS Appl. Mater. Interfaces 9, 36417 (2017).

15. F. Tendille, P. De Mierry, P. Vennéguès, S. Chenot, M. Teisseire, J. Cryst. Growth 404, 177 (2014).

16. J. Song, J. Choi, C. Zhang, Z. Deng, Y. Xie, J. Han, ACS Appl. Mater. Interfaces 11, 33140 (2019).

17. M. Khoury, H. Li, H. Zhang, B. Bonef, M. S. Wong, F. Wu, D. Cohen, P. De Mierry, P. Vennéguès, J.S. Speck, S. Nakamura, S.P. DenBaars, ACS Appl. Mater. Interfaces 11, 47106 (2019).

18. H. Li, P. Li, H. Zhang, S. Nakamura, S.P. DenBaars, ACS Appl. Electron. Mater. 2, 1874 (2020).

19. H. Zhang, H. Li, P. Li, J. Song, J.S. Speck, S. Nakamura, S.P. DenBaars, ACS Photonics 7, 1662 (2020).

20. J. Song, J. Han, Phys. Status Solidi B 257, 1900565 (2020).

20. S. Mehari, D.A. Cohen, D.L. Becerra, S. Nakamura, and S.P. DenBaars, Opt. Express 26, 1564 (2018).

21. K. Tanabe, *Energies*, **2**, 504 (2009).

22. I. Ichimura, F. Maeda, K. Osato, K. Yamamoto, and Y. Kasami, *Jpn. J. Appl. Phys., Part 1*, **39**, 937 (2000).

23. J. S. Im, H. Kollmer, J. Off, A. Sohmer, F. Scholz, and A. Hangleiter, *Phys. Rev. B*, **57**, R9435 (1998).

24. T. Takeuchi, S. Sota, M. Katsuragawa, M. Komori, H. Takeuchi, H. Amano, and I. Akasaki, *Jpn. J. Appl. Phys., Part 2*, **36**, L382 (1997).

25. P. Lefebvre, A. Morel, M. Gallart, T. Taliercio, J. Allegre, B. Gil, H. Mathieu, B. Damilano, N. Grandjean, and J. Massies, *Appl. Phys. Lett.*, **78**, 1252 (2001).

26. M. Suzuki and T. Uenoyama, *Jpn. J. Appl. Phys., Part 1*, **35**, 1420 (1996).

27. E. Yablonovitch and E. O. Kane, *J. Lightwave Technol.*, **4**, 504 (1986).

28. A. E. Romanov, T. J. Baker, S. Nakamura, and J. S. Speck, *J. Appl. Phys.*, **100**, 023522 (2006).

29. M. Suzuki and T. Uenoyama, *Jpn. J. Appl. Phys., Part 2*, **35**, L953 (1996).

30. K. Domen, K. Horino, A. Kuramata, and T. Tanahashi, *Appl. Phys. Lett.*, **70**, 987 (1997).

31. S. H. Park, *J. Appl. Phys.*, **91**, 9904 (2002).

32. S. H. Park, *Jpn. J. Appl. Phys., Part 2*, **42**, L170 (2003).

33. S. H. Park and D. Ahn, *Appl. Phys. Lett.*, **90**, 013505 (2007).

34. W. G. Scheibenzuber, U. T. Schwarz, R. G. Veprek, B. Witzigmann, and A. Hangleiter, *Phys. Rev. B*, **80**, 115320 (2009).

35. K. Kojima, A. A. Yamaguchi, M. Funato, Y. Kawakami, and S. Noda, *Jpn. J. Appl. Phys.*, **49**, 081001 (2010).

36. H. Amano, N. Sawaki, I. Akasaki, and Y. Toyoda, *Appl. Phys. Lett.*, **48**, 353 (1986).

37. B. A. Haskell, F. Wu, M. D. Craven, S. Matsuda, P. T. Fini, T. Fujii, K. Fujito, S. P. DenBaars, J. S. Speck, and S. Nakamura, *Appl. Phys. Lett.*, **83**, 644 (2003).

38. S. Nakamura, M. Senoh, N. Iwasa, and S. Nagahama, *Appl. Phys. Lett.*, **67**, 1868 (1995).

39. S. Nakamura, M. Senoh, N. Iwasa, S. Nagahama, T. Yamada, and T. Mukai, *Jpn. J. Appl. Phys., Part 2*, **34**, L1332 (1995).

40. S. Nakamura, M. Senoh, S. Nagahama, N. Iwasa, T. Yamada, T. Matsushita, H. Kiyoku, and Y. Sugimoto, *Jpn. J. Appl. Phys., Part 2*, **35**, L74 (1996).

41. P. Waltereit, O. Brandt, A. Trampert, H. T. Grahn, J. Menniger, M. Ramsteiner, M. Reiche, and K. H. Ploog, *Nature*, **406**, 865 (2000).

42. M. D. Craven, S. H. Lim, F. Wu, J. S. Speck, and S. P. DenBaars, *Appl. Phys. Lett.*, **81**, 1201 (2002).

43. H. M. Ng, *Appl. Phys. Lett.*, **80**, 4369 (2002).

44. M. D. Craven, S. H. Lim, F. Wu, J. S. Speck, and S. P. DenBaars, *Appl. Phys. Lett.*, **81**, 469 (2002).

45. T. Takeuchi, H. Amano, and I. Akasaki, *Jpn. J. Appl. Phys.*, *Part 1*, **39**, 413 (2000).

46. M. D. Craven, P. Waltereit, F. Wu, J. S. Speck, and S. P. DenBaars, *Jpn. J. Appl. Phys.*, *Part 2*, **42**, L235 (2003).

47. S. Nakamura, *Jpn. J. Appl. Phys.*, *Part 2*, **30**, L1705 (1991).

48. B. A. Haskell, F. Wu, S. Matsuda, M. D. Craven, P. T. Fini, S. P. DenBaars, J. S. Speck, and S. Nakamura, *Appl. Phys. Lett.*, **83**, 1554 (2003).

49. M. D. Craven, F. Wu, A. Chakraborty, B. Imer, U. K. Mishra, S. P. DenBaars, and J. S. Speck, *Appl. Phys. Lett.*, **84**, 1281 (2004).

50. N. F. Gardner, J. C. Kim, J. J. Wierer, Y. C. Shen, and M. R. Krames, *Appl. Phys. Lett.*, **86**, 111101 (2005).

51. T. J. Baker, B. A. Haskell, F. Wu, P. T. Fini, J. S. Speck, and S. Nakamura, *Jpn. J. Appl. Phys.*, *Part 2*, **44**, L920 (2005).

52. T. J. Baker, B. A. Haskell, F. Wu, J. S. Speck, and S. Nakamura, *Jpn. J. Appl. Phys.*, *Part 2*, **45**, L154 (2006).

53. B. A. Haskell, T. J. Baker, M. B. McLaurin, F. Wu, P. T. Fini, S. P. DenBaars, J. S. Speck, and S. Nakamura, *Appl. Phys. Lett.*, **86**, 111917 (2005).

54. A. Chakraborty, B. A. Haskell, S. Keller, J. S. Speck, S. P. DenBaars, S. Nakamura, and U. K. Mishra, *Appl. Phys. Lett.*, **85**, 5143 (2004).

55. A. Chakraborty, T. J. Baker, B. A. Haskell, F. Wu, J. S. Speck, S. P. Denbaars, S. Nakamura, and U. K. Mishra, *Jpn. J. Appl. Phys., Part 2*, **44**, L945 (2005).

56. A. Chakraborty, B. A. Haskell, S. Keller, J. S. Speck, S. P. Denbaars, S. Nakamura, and U. K. Mishra, *Jpn. J. Appl. Phys., Part 2*, **44**, L173 (2005).

57. R. Sharma, P. M. Pattison, H. Masui, R. M. Farrell, T. J. Baker, B. A. Haskell, F. Wu, S. P. DenBaars, J. S. Speck, and S. Nakamura, *Appl. Phys. Lett.*, **87**, 231110 (2005).

58. A. Chakraborty, B. A. Haskell, H. Masui, S. Keller, J. S. Speck, S. P. DenBaars, S. Nakamura, and U. K. Mishra, *Jpn. J. Appl. Phys., Part 1*, **45**, 739 (2006).

59. K. Fujito, S. Kubo, H. Nagaoka, T. Mochizuki, H. Namita, and S. Nagao, *J. Cryst. Growth*, **311**, 3011 (2009).

60. K. Fujito, K. Kiyomi, T. Mochizuki, H. Oota, H. Namita, S. Nagao, and I. Fujimura, *Phys. Status Solidi A*, **205**, 1056 (2008).

61. M. Funato, M. Ueda, Y. Kawakami, Y. Narukawa, T. Kosugi, M. Takahashi, and T. Mukai, *Jpn. J. Appl. Phys., Part 2*, **45**, L659 (2006).

62. K. Okamoto, H. Ohta, D. Nakagawa, M. Sonobe, J. Ichihara, and H. Takasu, *Jpn. J. Appl. Phys., Part 2*, **45**, L1197 (2006).

63. M. C. Schmidt, K. C. Kim, H. Sato, N. Fellows, H. Masui, S. Nakamura, S. P. DenBaars, and J. S. Speck, *Jpn. J. Appl. Phys., Part 2*, **46**, L126 (2007).

64. M. C. Schmidt, K. C. Kim, R. M. Farrell, D. F. Feezell, D. A. Cohen, M. Saito, K. Fujito, J. S. Speck, S. P. Denbaars, and S. Nakamura, *Jpn. J. Appl. Phys., Part 2*, **46**, L190 (2007).

65. K. Okamoto, H. Ohta, S. F. Chichibu, J. Ichihara, and H. Takasu, *Jpn. J. Appl. Phys., Part 2*, **46**, L187 (2007).

66. K. C. Kim, M. C. Schmidt, H. Sato, F. Wu, N. Fellows, M. Saito, K. Fujito, J. S. Speck, S. Nakamura, and S. P. DenBaars, *Phys. Status Solidi RRL*, **1**, 125 (2007).

67. K. C. Kim, M. C. Schmidt, H. Sato, F. Wu, N. Fellows, Z. Jia, M. Saito, S. Nakamura, S. P. DenBaars, and J. S. Speck, *Appl. Phys. Lett.*, **91**, 181120 (2007).

68. D. F. Feezell, M. C. Schmidt, R. M. Farrell, K. C. Kim, M. Saito, K. Fujito, D. A. Cohen, J. S. Speck, S. P. DenBaars, and S. Nakamura, *Jpn. J. Appl. Phys., Part 2*, **46**, L284 (2007).

69. R. M. Farrell, D. F. Feezell, M. C. Schmidt, D. A. Haeger, K. M. Kelchner, K. Iso, H. Yamada, M. Saito, K. Fujito, D. A. Cohen, J. S. Speck, S. P. DenBaars, and S. Nakamura, *Jpn. J. Appl. Phys., Part 2*, **46**, L761 (2007).

70. A. Tyagi, H. Zhong, N. N. Fellows, M. Iza, J. S. Speck, S. P. DenBaars, and S. Nakamura, *Jpn. J. Appl. Phys., Part 2*, **46**, L129 (2007).

71. A. Tyagi, H. Zhong, R. B. Chung, D. F. Feezell, M. Saito, K. Fujito, J. S. Speck, S. P. DenBaars, and S. Nakamura, *Jpn. J. Appl. Phys., Part 2*, **46**, L444 (2007).

72. K. Okamoto, T. Tanaka, M. Kubota, and H. Ohta, *Jpn. J. Appl. Phys., Part 2*, **46**, L820 (2007).

73. M. Kubota, K. Okamoto, T. Tanaka, and H. Ohta, *Appl. Phys. Express*, **1**, 011102 (2008).

74. Y. Tsuda, M. Ohta, P. O. Vaccaro, S. Ito, S. Hirukawa, Y. Kawaguchi, Y. Fujishiro, Y. Takahira, Y. Ueta, T. Takakura, and T. Yuasa, *Appl. Phys. Express*, **1**, 011104 (2008).

75. K. Okamoto, T. Tanaka, and M. Kubota, *Appl. Phys. Express*, **1**, 072201 (2008).

76. H. Zhong, A. Tyagi, N. N. Fellows, F. Wu, R. B. Chung, M. Saito, K. Fujito, J. S. Speck, S. P. DenBaars, and S. Nakamura, *Appl. Phys. Lett.*, **90**, 233504 (2007).

77. H. Sato, A. Tyagi, H. Zhong, N. Fellows, R. B. Chung, M. Saito, K. Fujito, J. S. Speck, S. P. DenBaars, and S. Nakamura, *Phys. Status Solidi RRL*, **1**, 162 (2007).

78. H. Zhong, A. Tyagi, N. N. Fellows, R. B. Chung, M. Saito, K. Fujito, J. S. Speck, S. P. DenBaars, and S. Nakamura, *Electron. Lett*, **43**, 825 (2007).

79. K. Iso, H. Yamada, H. Hirasawa, N. Fellows, M. Saito, K. Fujito, S. P. Denbaars, J. S. Speck, and S. Nakamura, *Jpn. J. Appl. Phys., Part 2*, **46**, L960 (2007).

80. W. Zeller, L. Naehle, P. Fuchs, F. Gerschuetz, L. Hildebrandt, and J. Koeth, *Sensors* 10, **2492** (2010).

81. Y. Shimada, Y. Chida, N. Ohtsubo, T. Aoki, M. Takeuchi, T. Kuga, and Y. Torii, *Rev. Sci. Instrum.* **84**, 063101 (2013)

82. S. Kono, R. Koda, H. Kawanishi, and H. Narui, *Opt. Express* **25**, 14926 (2017).

83. K. Numata, J. R. Chen, S. T. Wu, J. B. Abshire, and M. A. Krainak, *Appl. Opt.* **50**, 1047 (2011).

84. V. Weldon, J. Ogorman, P. Phelan, J. Hegarty, and T. Tanbun-Ek, *Sens. Actuators B Chem.* **29**, 101 (1995).

85. A. Stingl, R. Szipöcs, M. Lenzner, C. Spielmann, and F. Krausz, *Opt. Lett.* **20**, 602 (1995).

II. (2021) plane GaN high power laser diode

In this chapter, we are going to review the designs and development of the semipolar laser diodes we have worked on over the last few years, which also set the foundation for the DFB-LDs work. This section will be into three different parts- the review of basic knowledge of laser diodes, the unique properties of semipolar laser diodes, and the performance of the devices.

A. Laser basics

By design, the structures of LDs are very similar to LEDs in both growth and fabrication yet there are also several key differences. Unlike LEDs, photons coming from electron-hole recombination need to be confined in a resonant cavity with feedback from mirrors or other grating structure which can provide reflections. [1] The injected carriers (electrons and holes) are recombined in the quantum wells and emit photons, when the population of photons reaches a certain threshold, the generated photon will force more photons to be emitted due to population inversion, the stimulated emission starts and the optical amplification ensues. Thus, to confine the photons, there are usually layers of lower refractive index InGaN, GaN, or AlGaN on either side of the high refractive index QWs of the active region. [2-6] The active region of serval quantum wells will typically be surrounded by a separate confining heterostructure (SCH) for this purpose.

1. Terms and Performance Metrics of LDs

Due to the nature of the materials (dopants, bandgaps), certain amount of optical loss (or absorption) will be always present. In order for a laser to reach threshold, the point at which lasing begins, the gain must exceed the loss. When the current density is low, the cavity is absorbing and therefore not transparent. As the current continues to increase and more carriers are pumped in, gain will begin to be greater than the loss (a net gain is greater than zero). The point at which gain is greater than loss is the threshold condition.

Similar to the concept in LED, WPE is wall plug efficiency is the ratio of how much light output power one can get from certain electrical power injected. In general this can be split into three efficiencies for lasers: injection efficiency, differential efficiency, and voltage efficiency. The differential efficiency, η_d, is how efficiently carriers are converted to emitted photons in the active region above threshold. Injection efficiency, η_i, is a measure of the ratio of the number of carriers which can be contributed to the stimulated emission in the active region to all carriers injected to the device. The voltage efficiency, η_v, is the photon energy compared to the working voltage. Equation 2-1 shows the expression for WPE expressed in terms of the other three efficiency terms.

$$\eta_{WPE} = \eta_v \, \eta_d \eta_i \tag{2-1}$$

Then we have some other important parameters that affect the differential efficiency. The mirror loss denotes how many photons coming out of the cavity (normally from a mirror) as output power. The internal loss, α_i , is a material loss due to absorption by free carriers or special designs. The mirror loss can be further calculated as below:

$$\boldsymbol{\alpha_m = \frac{1}{L} ln\left(\frac{1}{R}\right)} \tag{2-2}$$

Specifically, the confining layers that GaN LD also needs to confine photons is a tricky issue. In most c-plane lasers people grow AlGaN as the cladding layer due to its lower refractive index compared to GaN. [7], [8] But there are many challenges when growing AlGaN since the lattice mismatch stress/strain from AlGaN is often large and unavoidable which reduces the material quality of QWs and the overall efficiency. In contrast one could also use low composition InGaN as a waveguiding layer in a separate confining heterostructure configuration and remove AlGaN cladding layers. This is termed an AlGaN-cladding-free design and has been demonstrated by our group many times on various planes of GaN.[9]–[18]

B. Semipolar $(20\overline{21})$ GaN Laser Diodes

Till now the GaAs LDs emitting in the red spectral range are still the most efficient semiconductor lasers with over 70% of WPE that has been achieved long ago.[19] On the contrast, InGaN LD efficiencies remain lower. Research efforts in recent years, primarily focused on improving the material quality of violet to blue c-plane LDs, have shown great progress. To the author's knowledge, the highest WPE InGaN LDs are from Nichia Corp. at about 45%. [20] This laser diode was grown on the c-plane. The threshold efficiency is similar to GaAs state of the art, but voltage and slope efficiencies remain lower. But at longer wavelengths the picture looks far less rosy. A promising route to improve the efficiency, especially at longer wavelengths, is to grow the quantum wells (QWs) on non-c-plane directions, which is predicted to improve the radiative efficiency and gain. [21-25] The reduction of polarization fields from moving to semipolar or nonpolar devices will increase threshold efficiency by increasing the gain parameters and reducing the threshold currents. Both the improved wavefunction overlap and changed density of states will contribute to more efficient lasing. Among the most important advantages of QWs grown on non-basal directions are: high indium incorporation, reduced hole effective mass due to anisotropic strain, and increased electron-hole wavefunction overlap due to lower polarization-related electrical fields. To fully exploit this potential, it is crucial to thoroughly understand the underlying physical mechanisms that deteriorate the LD’s operation.

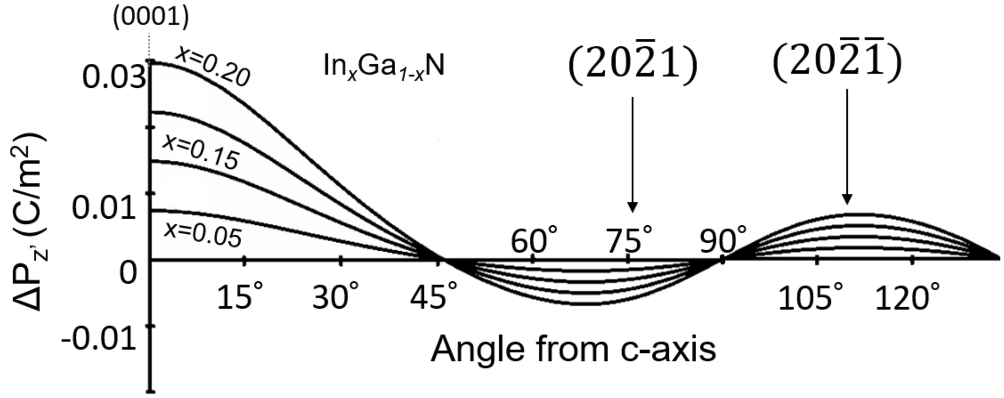

FIG. 2.1. Polarization vs Angle in GaN

On semipolar planes, the valence band degeneracy is broken leading to reduction of hole effective mass and the inversion of more efficient carriers, which should also reduce the transparent carrier density. [26] Additionally, the improved wavefunction overlap will yield higher gain per carrier above transparency, thus the differential gain will be higher. The radiative lifetime is reduced on semipolar planes, from 6 to 9 ns on c-plane to 2 to 3 ns on semipolar planes. This has been experimentally verified by Melo et. al. [27] Prior semipolar LD results at UCSB have shown WPE of a few percent, improvement will be shown throughout this dissertation. Above all the pages must be conceived as a sequence of images with design continuity. The reader should experience the pages as a flow of related events rather than as separate isolated entities.

Growth on semipolar planes has its own distinct advantages and challenges. This dissertation will especially focus on growth on semipolar planes $(20\bar{2}\bar{1})$ due to its recent fast development at UCSB. Much early semipolar growth development was done by Hsu, Hardy, Zhao, Pan, and others.[28]–[32] These semipolar planes have certain polarization properties that have been discussed previously or will be discussed later. For growth on these planes, the conditions of the first epitaxial layer, the template, must first be optimized, and these optimized conditions will be discussed here. During template growth, it is important to maintain a smooth surface for the growth of subsequent layers. The conditions can be different depending on the plane. [33] Growing on bulk GaN substrates simplifies this process, but work must still be done to optimize the template.

The GaN substrates from MCC are polished using a proprietary series of mechanical and/or chemical polishing steps. It is suspected, but cannot be confirmed for proprietary reasons, that there is some weak surface or subsurface damage. Thus, an unoptimized template will propagate this damage in the form of defects such as those seen in Figure 2-2, and such defects will lead to a serious degradation of laser performance. Therefore, the optimization of the template before any useful growth is necessary. To achieve that, the substrate is first heated in hydrogen carrier gas which will weakly etch and smooth out the substrate surface,

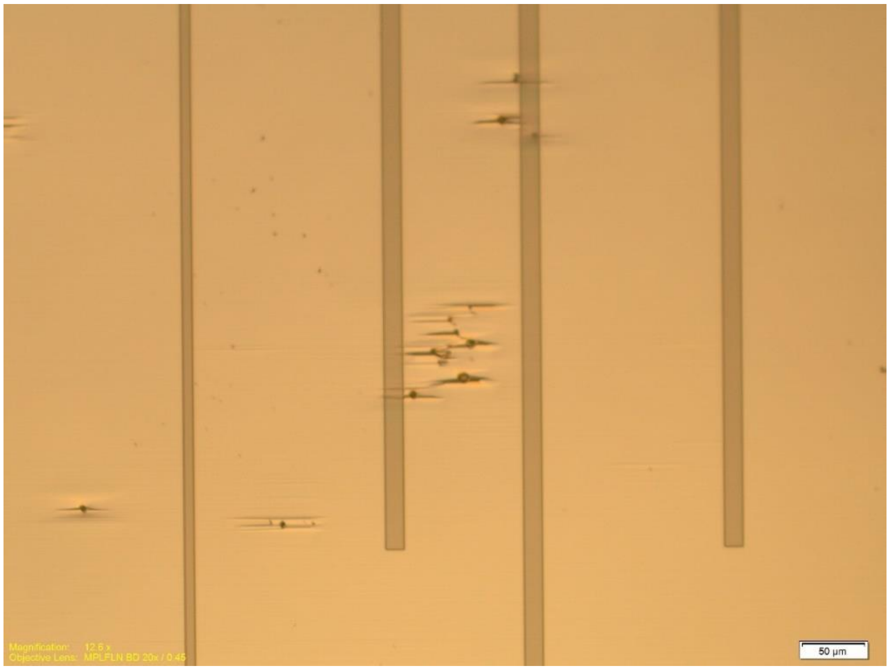

FIG. 2.2. Surface of Device with Poor Template Condition

and then about 1-µm n doped GaN template is grown at high temperatures between 1150 and 1200 degree C heater set temperature.

The substrate for the high power LDs was $(20\overline{21})$, chosen because of the high indium incorporation, low polarization fields, and low wavelength shift demonstrated on devices grown on this plane.[34], [35] Compared to LEDs, certain additional features must be considered when designing the epitaxial structure of LDs. Earlier works at UCSB have tackled many of these issues; In the next chapters, the structure we present will be based on the epitaxial structure developed by Pourhashemi, Farrell, Becerra and Mehari as a guide. [36-38] Figure 2-3 shows this structure.

The epitaxial structure consisted of a 1-µm n-GaN cladding, followed by a 10-nm linear composition grade from n-GaN to 50-nm n-In$_{0.05}$Ga$_{0.95}$N waveguiding layer, and another 10-nm linear grade back down to the first GaN barrier. The active region consisted of an undoped 2-period InGaN/GaN (3.5 nm / 7 nm) multiple quantum well (MQW) emitting at about 440-

445 nm followed by a 10-nm p-$Al_{0.18}Ga_{0.82}N$ electron blocking layer, which was then linearly graded in composition over 10 nm to p-GaN. The p-type waveguiding layer followed with the same composition grading and thicknesses as in the n-type waveguiding layer. The p-GaN cladding was 250 nm thick and capped with a p++ contact layer. The compositional grades are designed to limit voltage drop at the heterointerfaces. By introducing a compositional grade, the band diagram will be smoothed out near the interface and no sharp barrier to charged carrier flow will be present. The waveguiding layers are carefully optimized to provide confinement and the indium composition must also be kept low enough so as to not absorb and of the light from the active region since sub-bandgap absorption may be an issue

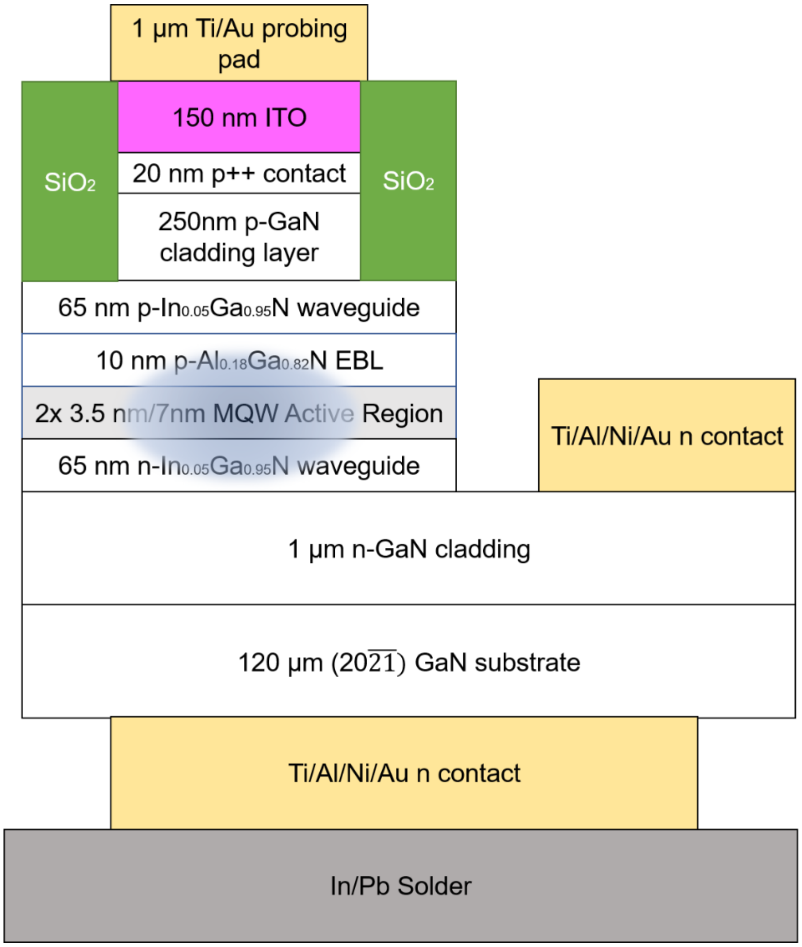

FIG. 2.3. Schematic cross-section of the optimized edge-emitting laser diode

with these layers which it may be explored in future works. The p++ contact layer must also be carefully engineered to obtain an ohmic contact. The doping and composition of the EBL must be carefully selected to create a barrier to electron overflow but no impedance to hole injection. The doping in the EBL is usually kept higher than the doping in the p-type layers on either side for that purpose.

As described in the section A, when designing the laser, it is also important to consider the internal loss and the confinement of carriers and photons. Normally the transfer matrix method [36] was used to model the 1D mode of the vertical waveguide structure and calculate the confinement factor and internal loss contribution of each layer for these LDs. The optical mode profile and layer confinement factors and loss were calculated using inputs from several experimental obserbvations: the bandgap was based on the results from Sakalauskas *et al*.,[37] the refractive indices of GaN and AlGaN were taken from Sanford *et al*., [38] and the refractive indices of InGaN from Bergmann *et al*.[39] A carrier density in the quantum wells of 1×10^{19} cm^{-3} was assumed, The confinement factor, calculated as the overlap of the mode with the active region in this design is 3%. Figure 2-3 (a) shows a plot of refractive index versus depth, a simulated mode profile (black dashed line), and the calculated modal absorption (green area) in each layer. The effective index of the mode is also indicated (horizontal dotted line). The calculated QW confinement factor was 0.03 and the calculated internal loss was close to 9.5 cm^{-1}, which in previous reports showed good agreement with the experimental results. [42]

C. Optimization of p-cladding and waveguide in semipolar GaN Laser Diodes

Two big hurdles for the improvement of semipolar laser diodes are the poor voltage performance and low injection efficiency. For III-nitride devices, the Mg doping levels in the p-GaN layer is crucial- it cannot be too high or else it would increase the optical loss yet reducing Mg doping levels will also lead to a penalty of voltage performance. Instead, the p-GaN thickness and replaced the metallic p-contact with a low absorption ITO contact. As shown in Figure 2-3 (b), previous experiments have shown that when the p-GaN thickness was decreased from 650 nm to 250 nm the CW operating voltage significantly decreased without impacting the light output characteristic. A further reduction in the p-GaN thickness from 250 nm to 150 nm will lead to an additional decrease in the operating voltage, as shown in summary of characteristics of 8x1200 μm LDs (Figure 2.3 (b)). However, the light output power at this point started to decrease due to higher loss in the ITO area which will be covered in the next chapter in greater details.

Due to the low hole mobility of the p-GaN, low current injection has also been a lingering issue which leads to low threshold efficiency and higher threshold current. Therefore, in order to improve the current injection and suppress a possible carrier sink while still benefiting from lower optical losses, we also studied on the location of the EBL. As shown in Figure 2.4, pushing the EBL to a farther distance from the quantum wells will not improve the overall performance and the threshold current density increases to more than 2 times, indicating that the injection efficiency was seriously affected. But considering that the slope efficiency was also improved the optical losses are possibly lower than the standard LDs. Such effect of locations of the EBL, together with its doping concentration are wroth further exploration.

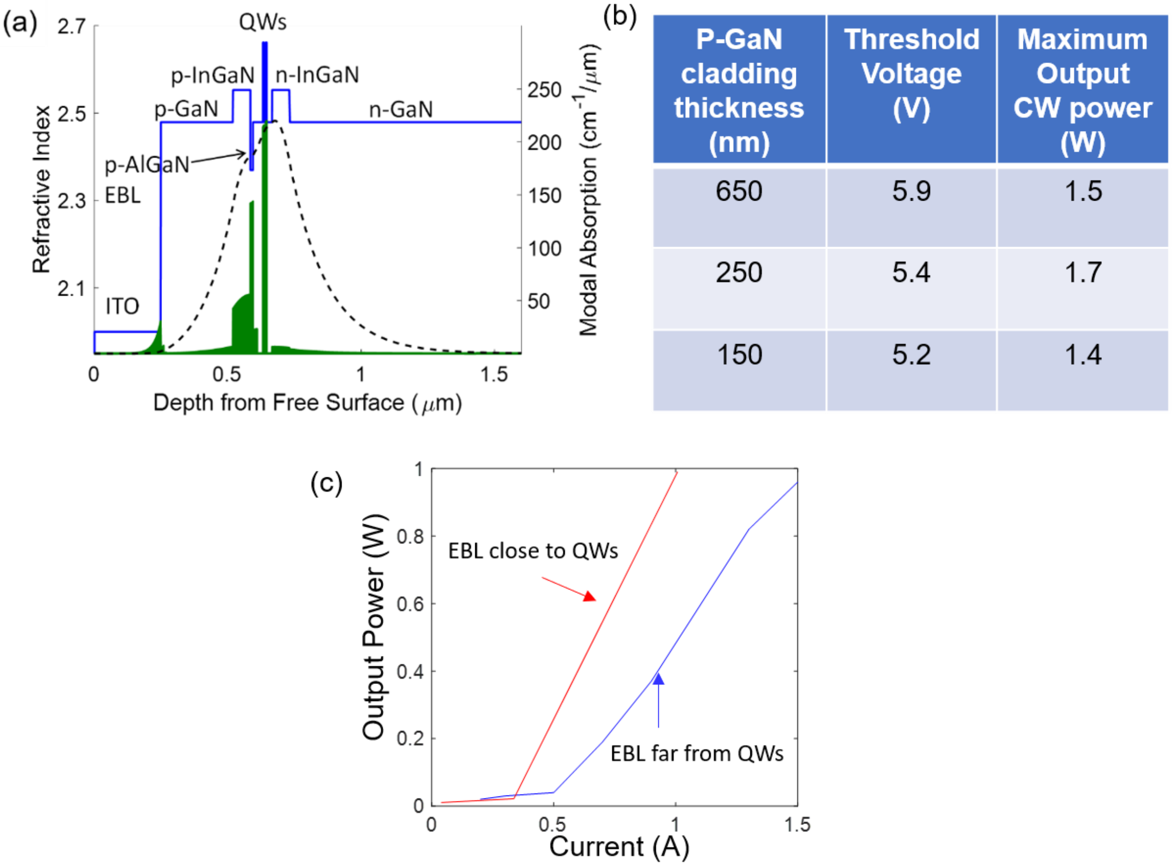

P-GaN cladding thickness (nm)	Threshold Voltage (V)	Maximum Output CW power (W)
650	5.9	1.5
250	5.4	1.7
150	5.2	1.4

FIG. 2.3. (a) Optical mode profile calculation along our baseline LD layers with their associated optical loss (shaded green). (b) Absorption spectra of two LDs, one with an EBL close to the QWs and a high Mg doping profile, and a second with a remote EBL and a low Mg doping profile. b) L-I curves of LDs with different p-WG designs.

D. DFB-LDs basics

Instead of using mirrors DFB (Distributed feedback), laser diodes use grating structure to provide feedback to reach threshold. Gratings are generally fabricated on the bare substrates before processing and the full laser structure is regrown afterward. A primary reason that people are interested DFB lasers is their relatively simple fabrication and ability to schieve single-frequency operation. To measure the purity and quality of a single-frequency laser diode, a characteristic called the mode suppression ratio (MSR), is normally used. Mode suppression ratio is the ratio of the output power in the primary laser mode to that in the next strongest mode from one end of the laser, which can be given as [43]:

$$\boldsymbol{MSR} = \frac{\boldsymbol{P(\lambda_0)}}{\boldsymbol{P(\lambda_1)}} \tag{2-3}$$

Where λ_0 and λ_1 are the primary and second strongest mode of the emission spectrum. Furthermore, in a DFB laser diode, the MSR can be expressed as:

$$\boldsymbol{MSR} = \frac{\boldsymbol{\Delta\alpha+\Delta g}}{\boldsymbol{\delta g}}+1 \tag{2-4}$$

Where $\boldsymbol{\Delta\alpha}$ is the mirror loss margin $\boldsymbol{\delta g}$ is net modal gain for the main mode, and $\boldsymbol{\Delta g}$ is the modal gain margin In the following chapters, we will go through all the important parameters that will affect the MSR and DFB laser performance.

References

1 J. J. Wierer, J. Y. Tsao, and D. S. Sizov, “Comparison between blue lasers and light-emitting diodes for future solid-state lighting,” Laser Photon. Rev., vol. 7, no. 6, pp. 963–993, Nov. 2013.

2 A. Pourhashemi, R. M. Farrell, M. T. Hardy, P. S. Hsu, K. M. Kelchner, J. S. Speck, S. P. Denbaars, and S. Nakamura, “Pulsed high-power AlGaN-cladding-free blue laser diodes on semipolar (20-2-1) GaN substrates,” Appl. Phys. Lett., vol. 103, p. 151112, 2013.

3 P. Waltereit, O. Brandt, A. Trampert, H.T. Grahn, J. Menniger, M. Ramsteiner, M. Reiche, and K.H. Ploog, Nature 406, 865 (2000).

4. M.T. Hardy, C.O. Holder, D.F. Feezell, S. Nakamura, J.S. Speck, D.A. Cohen, S.P. DenBaars, Appl. Phys. Lett. 103, 081103 (2013).
5. Y. Zhao, H. Fu, G.T. Wang, and S. Nakamura, Adv. Opt. Photonics 10, 246 (2018).
6. W. G. Scheibenzuber, U. T. Schwarz, R. G. Veprek, B. Witzigmann, A. Hangleiter, Phys. Rev. B 80, 115320 (2009).
7. C. Lee, C. Zhang, D.L. Becerra, S. Lee, C. A. Forman, S. Ho Oh, R. M. Farrell, J. S. Speck, S. Nakamura, J. E. Bowers, and S. P. DenBaars, Appl. Phys. Lett. 109, 101104 (2016).
8. H. Li, P. Li, H. Zhang, Y.C. Chow, M.S. Wong, S. Pinna, J. Klamkin, J.S. Speck, S. Nakamura, S.P. DenBaars, Opt. Express 28, 13569 (2020).
9. N. F. Gardner, J. C. Kim, J. J. Wierer, Y. C. Shen, and M. R. Krames, Appl. Phys. Lett. 86, 111101 (2005).
10. M. Cantore, N. Pfaff, R. M. Farrell, J. S. Speck, S. Nakamura, and S. P. DenBaars, "High luminous flux from single crystal phosphor-converted laser-based white lighting system," Opt. Express, vol. 24, no. 2, p. A215, 2016.
11. S. Masui, T. Miyoshi, T. Yanamoto, and S. Nagahama, "Blue and green laser diodes for large laser display," in 2013 Conference on Lasers and Electro-Optics Pacific Rim (CLEOPR), 2013, p. SA1-3.

12. C. A. Hurni, A. David, M. J. Cich, R. I. Aldaz, B. Ellis, K. Huang, A. Tyagi, R. A. Delille, M. D. Craven, F. M. Steranka, and M. R. Krames, “Bulk GaN flip-chip violet light-emitting diodes with optimized efficiency for high-power operation,” Appl. Phys. Lett., vol. 106, no. 3, pp. 0–4, 2015.

13. P. Crump, G. Erbert, H. Wenzel, C. Frevert, C. M. Schultz, K.-H. Hasler, R. Staske, B. Sumpf, A. Maassdorf, F. Bugge, S. Knigge, and G. Trankle, “Efficient High-Power Laser Diodes,” IEEE J. Sel. Top. Quantum Electron., vol. 19, no. 4, pp. 1–11, 2013.

14. W. Scheibenzuber, U. Schwarz, R. Veprek, B. Witzigmann, and a. Hangleiter, “Calculation of optical eigenmodes and gain in semipolar and nonpolar InGaN/GaN laser diodes,” Phys. Rev. B, vol. 80, no. 11, p. 115320, Sep. 2009.

15. D. F. Feezell, J. S. Speck, S. P. Denbaars, and S. Nakamura, “Semipolar 2021 InGaN / GaN Light-Emitting Diodes for High-Efficiency Solid-State Lighting,” J. Disp. Technol., vol. 9, no. 4, pp. 190–198, 2013.

16. C.-C. Pan, S. Tanaka, F. Wu, Y. Zhao, J. S. Speck, S. Nakamura, S. P. DenBaars, and D. Feezell, “High-Power, Low-Efficiency-Droop Semipolar ($20\bar{2}\bar{1}$) Single-Quantum-Well Blue Light-Emitting Diodes,” Appl. Phys. Express, vol. 5, no. 6, p. 62103, Jun. 2012.

17. A. Pourhashemi, R. M. Farrell, D. A. Cohen, J. S. Speck, S. P. DenBaars, and S. Nakamura, “High-power blue laser diodes with indium tin oxide cladding on semipolar (202¯1¯) GaN substrates,” Appl. Phys. Lett., vol. 106, p. 111105, 2015.

18. D. L. Becerra, L. Y. Kuritzky, J. Nedy, A. S. Abbas, A. Pourhashemi, R. M. Farrell, D. A. Cohen, S. P. DenBaars, J. S. Speck, and S. Nakamura, “Measurement and analysis of internal loss and injection efficiency for continuous-wave blue semipolar (20$\bar{2}\bar{1}$) III-nitride laser diodes with chemically assisted ion beam etched facets,” Appl. Phys. Lett., vol. 108, p. 91106, 2016.

19. H. Y. Ryu, K. H. Ha, J. K. Son, S. N. Lee, H. S. Paek, T. Jang, Y. J. Sung, K. S. Kim, H. K. Kim, Y. Park, and O. H. Nam, “Determination of internal parameters in blue InGaN laser diodes by the measurement of cavity-length dependent characteristics,” Appl. Phys. Lett., vol. 93, no. 1, pp. 10–13, 2008.

20. R. M. Farrell, D. a. Haeger, P. S. Hsu, K. Fujito, D. F. Feezell, S. P. DenBaars, J. S. Speck, and S. Nakamura, “Determination of internal parameters for AlGaN-cladding-free m-plane InGaN/GaN laser diodes,” Appl. Phys. Lett., vol. 99, no. 17, p. 171115, 2011.

21. L. A. Coldren, S. W. Corzine, and M. L. Mašanović, Diode Lasers and Photonic Integrated Circuits. Hoboken, NJ, USA: John Wiley & Sons, Inc., 2012.

22. D. L. Becerra, D. A. Cohen, R. M. Farrell, S. P. Denbaars, and S. Nakamura, “Effects of active region design on gain and carrier injection and transport of CW (20-2-1) semipolar InGaN laser diodes,” Appl. Phys. Express, vol. 9, p. 92104, 2016.

23. L. Y. Kuritzky, D. L. Becerra, A. S. Abbas, J. G. Nedy, S. Nakamura, D. A. Cohen, and S. P. DenBaars, “Chemically assisted ion beam etching of laser diode facets on

nonpolar and semipolar orientations of GaN," Semicond. Sci. Technol., vol. 31, no. 7, pp. 1–7, 2016.

24. P. Kozodoy, H. Xing, S. P. DenBaars, U. K. Mishra, A. Saxler, R. Perrin, S. Elhamri, and W. . Mitchel, "Heavy doping effects in Mg-doped GaN," J. Appl. Phys., vol. 87, no. 4, pp. 1832–1835, 2000.
25. M. Kneissl, D. Hofstetter, D. P. Bour, R. Donaldson, J. Walker, and N. M. Johnson, "Dry-etching and characterization of mirrors on III-nitride laser diodes from chemically assisted ion beam etching," J. Cryst. Growth, vol. 189–190, pp. 846–849, Jun. 1998.
26. E. Kioupakis, P. Rinke, K. T. Delaney, and C. G. Van de Walle, "Indirect Auger recombination as a cause of efficiency droop in nitride light-emitting diodes," Appl. Phys. Lett., vol. 98, no. 16, p. 161107, 2011.
27. A. David, M. J. Grundmann, J. F. Kaeding, N. F. Gardner, T. G. Mihopoulos, and M. R. Krames, "Carrier distribution in (0001) InGaNGaN multiple quantum well light-emitting diodes," Appl. Phys. Lett., vol. 92, no. 5, pp. 1–4, 2008.
28. A. Bojarska, Ł. Marona, I. Makarowa, R. Czernecki, M. Leszczynski, T. Suski, and P. Perlin, "Negative-T0 InGaN laser diodes and their degradation," Appl. Phys. Lett., vol. 106, no. 17, p. 171107, 2015.
29. Y. Kawaguchi, C. Huang, Y. Wu, Q. Yan, C. Pan, Y. Zhao, S. Tanaka, K. Fujito, D. Feezell, C. G. Van De Walle, S. P. Denbaars, and S. Nakamura, "Influence of polarity

on carrier transport in semipolar (2021) and (20 21) multiple-quantum-well light-emitting diodes," Appl. Phys. Lett., vol. 100, p. 231110, 2012.

30. M. Kneissl, D. P. Bour, N. M. Johnson, L. T. Romano, B. S. Krusor, R. Donaldson, J. Walker, and C. Dunnrowicz, "Characterization of AlGaInN diode lasers with mirrors from chemically assisted ion beam etching," Appl. Phys. Lett., vol. 72, no. 13, p. 1539, 1998.

31. S. C. Cruz, S. Keller, T. E. Mates, U. K. Mishra, and S. P. DenBaars, "Crystallographic orientation dependence of dopant and impurity incorporation in GaN films grown by metalorganic chemical vapor deposition," J. Cryst. Growth, vol. 311, no. 15, pp. 3817–3823, Jul. 2009.

32. M. Scherer, V. Schwegler, M. Seyboth, F. Eberhard, C. Kirchner, M. Kamp, G. Ulu, M. S. Ünlü, R. Gruhler, and O. Hollricher, "Characterization of etched facets for GaN-based lasers," J. Cryst. Growth, vol. 230, no. 3–4, pp. 554–557, Sep. 2001.

33. L. Y. Kuritzky, D. L. Becerra, A. S. Abbas, J. G. Nedy, S. Nakamura, D. A. Cohen, and S. P. DenBaars, "Chemically assisted ion beam etching of laser diode facets on nonpolar and semipolar orientations of GaN," Semicond. Sci. Technol., vol. 31, no. 7, pp. 1–7, 2016.

34. Y. Kawaguchi, C. Huang, Y. Wu, Q. Yan, C. Pan, Y. Zhao, S. Tanaka, K. Fujito, D. Feezell, C. G. Van De Walle, S. P. Denbaars, and S. Nakamura, "Influence of polarity on carrier transport in semipolar (2021) and (20 21) multiple-quantum-well light-emitting diodes," Appl. Phys. Lett., vol. 100, p. 231110, 2012.

35. R. M. Farrell, P. S. Hsu, D. a. Haeger, K. Fujito, S. P. DenBaars, J. S. Speck, and S. Nakamura, “Low-threshold-current-density AlGaN-cladding-free m-plane InGaN/GaN laser diodes,” Appl. Phys. Lett., vol. 96, no. 23, p. 231113, 2010.

36. H. Y. Ryu, K. H. Ha, S. N. Lee, T. Jang, H. K. Kim, J. H. Chae, K. S. Kim, K. K. Choi, J. K. Son, H. S. Paek, Y. J. Sung, T. Sakong, O. H. Nam, and Y. J. Park, “Highly stable temperature characteristics of InGaN blue laser diodes,” Appl. Phys. Lett., vol. 89, p. 31122, 2006.

37. V. Savona, “Linear Optical Properties of Semiconductor Microcavities with Embedded Quantum Wells,” in Confined Photon Systems Lecture Notes in Physics, no. vol 531, H. Benisty, C. Weisbuch, J. M. Gerard, R. Houdre, and J. Rarity, Eds. Berlin Heidelberg: Springer, 1999, pp. 173–82.

38. E. Sakalauskas, Ö. Tuna, a. Kraus, H. Bremers, U. Rossow, C. Giesen, M. Heuken, a. Hangleiter, G. Gobsch, and R. Goldhahn, “Dielectric function and bowing parameters of InGaN alloys,” Phys. Status Solidi, vol. 249, no. 3, pp. 485–488, Mar. 2012.

39. N. a. Sanford, L. H. Robins, a. V. Davydov, a. Shapiro, D. V. Tsvetkov, a. V. Dmitriev, S. Keller, U. K. Mishra, and S. P. DenBaars, “Refractive index study of Al[sub x]Ga[sub 1−x]N films grown on sapphire substrates,” J. Appl. Phys., vol. 94, no. 5, p. 2980, 2003.

40. M. J. Bergmann and H. C. Casey, “Optical-field calculations for lossy multiple-layer AlxGa1−xN/InxGa1−xN laser diodes,” J. Appl. Phys., vol. 84, no. 3, p. 1196, 1998.

41. E. Kioupakis, P. Rinke, and C. G. Van de Walle, “Determination of Internal Loss in Nitride Lasers from First Principles,” Appl. Phys. Express, vol. 3, no. 8, p. 82101, Jul. 2010.

42. D L. Becerra, L. Y. Kuritzky, J. Nedy, A. S. Abbas, A. Pourhashemi, R. M. Farrell, D. A. Cohen, S. P. DenBaars, J. S. Speck, and S. Nakamura, “Measurement and analysis of internal loss and injection efficiency for continuous-wave blue semipolar (20$\bar{2}\bar{1}$) III-nitride laser diodes with chemically assisted ion beam etched facets,” Appl. Phys. Lett., vol. 108, p. 91106, 2016.

43. L.A. Coldren, S.W. Corzine, and L.M Mashanovitch, Diode Lasers and Photonic Integrated Circuits, Wiley, New York (2012).

III. First order distributed feedback laser diode with etched grating

A. Inspiration and design

Instead of achieving the narrow linewidth and robust wavelength emission, the first few works on GaN DFB-LD focused on the use of grating to provide feedback and enhance the reflectivity of the mirrors due to the complexity of fabricating facets on GaN. Most previous GaN DFB-LDs have been fabricated with epitaxially buried group III-N gratings. Regrowth technique, which has been widely used on InP or GaAs DFB laser diodes, is still a relatively difficult and expensive method for GaN due to the occurrence of lattice mismatch and high defect density. An obvious result of such method was the poor output power.

In history, the first DFB-LD on GaN was based on a holographically defined third-order grating on sapphire. The 3rd order grating was dry etched into the upper waveguiding layer by chemically assisted ion beam etching and then the rest of the cladding layer was regrown. A high threshold current and voltage was observed, and the device exhibited a plausible single-mode lasing under pulsed operation with less than 20 dB SMSR. Later on, in 2004 the DFB-LDs with first order grating was successively demonstrated on GaN substrates under continuous wave operation. Compared to the previous pulsed work, the first order DFB-LDs exhibit a significant increase in voltage and power performance yet still faced low SMSR. Due to the emergence of new applications that require high-power single-mode visible laser beams, lasers with novel designs were invented after a long hiatus. Among them, laser with lateral V-shaped groove gratings was the most successful and popular one to reduce the regrowth cost and simplify the fabrication process, however it could potentially add additional optical loss from the etching and reduce the optical confinement alongside the ridge. Most of the results reported so far showed the maximum power output of less than 100 mW, which is unsatisfactory given that the Watt-class single GaN laser diode has been nearly commercialized. Table 1 listed a comparison of previously published results on GaN DFB-LDs through the last two decades.

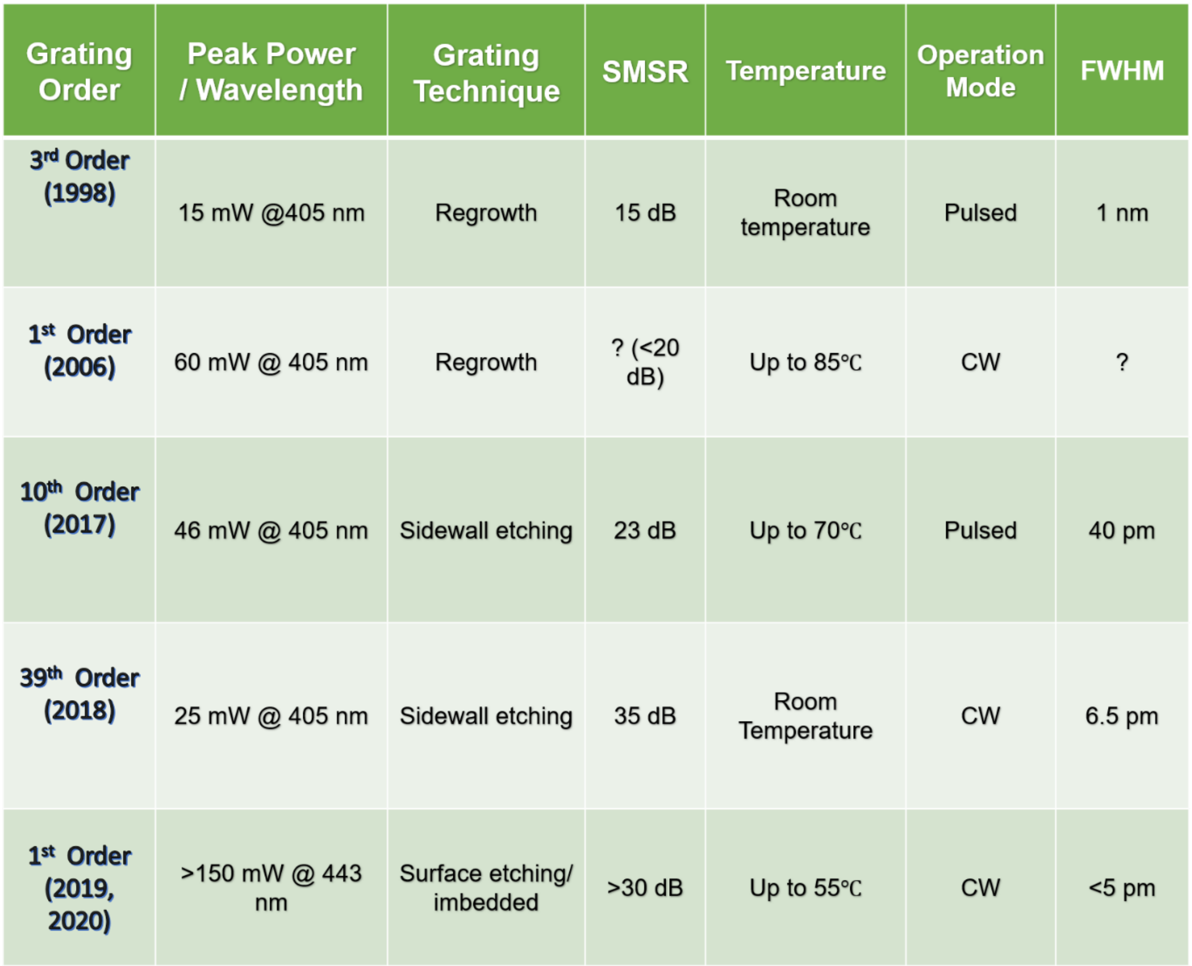

Grating Order	Peak Power / Wavelength	Grating Technique	SMSR	Temperature	Operation Mode	FWHM
3rd Order (1998)	15 mW @405 nm	Regrowth	15 dB	Room temperature	Pulsed	1 nm
1st Order (2006)	60 mW @ 405 nm	Regrowth	? (<20 dB)	Up to 85℃	CW	?
10th Order (2017)	46 mW @ 405 nm	Sidewall etching	23 dB	Up to 70℃	Pulsed	40 pm
39th Order (2018)	25 mW @ 405 nm	Sidewall etching	35 dB	Room Temperature	CW	6.5 pm
1st Order (2019, 2020)	>150 mW @ 443 nm	Surface etching/ imbedded	>30 dB	Up to 55℃	CW	<5 pm

Table 3.1. Recent progress and comparison of the III-nitride distributed feedback laser diodes with different techniques.

On the other hand, simulation shows that significant amount of mode overlaps with the ITO cladding layer due to now thinned p-cladding layer. Previous chapter has shown that such increase of overlap makes it difficult to further reduce the threshold voltage due to the lossy nature of ITO layer, however, can be beneficial if we want to take advantage of the overlap in

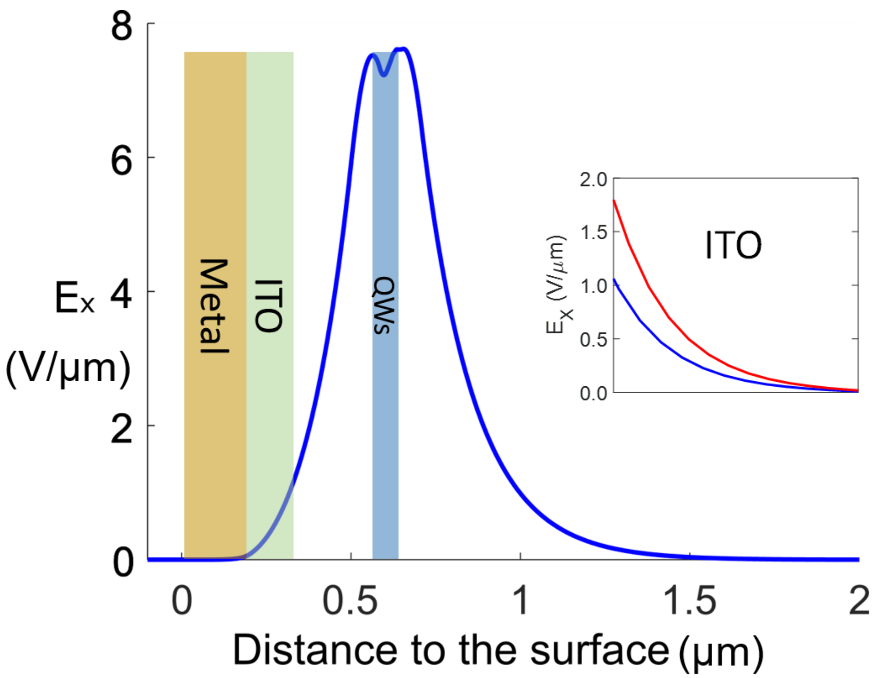

Figure 3.2. The calculated optical mode profiles in LDs structures with a 250 nm p-GaN thickness (standard structure). Significant overlap of the mode can be found in the green region. The zoom-in figures (right side) show the increased overlap of the optical mode with the ITO contact as the p-GaN thickness is reduced to 150 nm (distance scales on all graphs).

building up distributed feedback by fabricating surface gratings on the top of the area. One can speculate that if the overlap is large enough, gratings fabricated on the top of the ITO layer can contribute adequate reflection for laser to reach threshold, even without the uses of facets. Such approach with surface gratings, which potentially combines the benefits of both scalability and low cost due to no need for regrowth, still have not been fully explored before. On the other hand, to meet the needs of high-speed communication applications, the power and efficiency of the visible III-Nitride DFB-LDs must also be further improved. In III-nitride systems, as we have introduced in the previous chapters, a promising route to improve the total power and efficiency is to grow the quantum wells on non-c-plane directions, which is predicted to improve the radiative efficiency and differential gain due to increased electron-

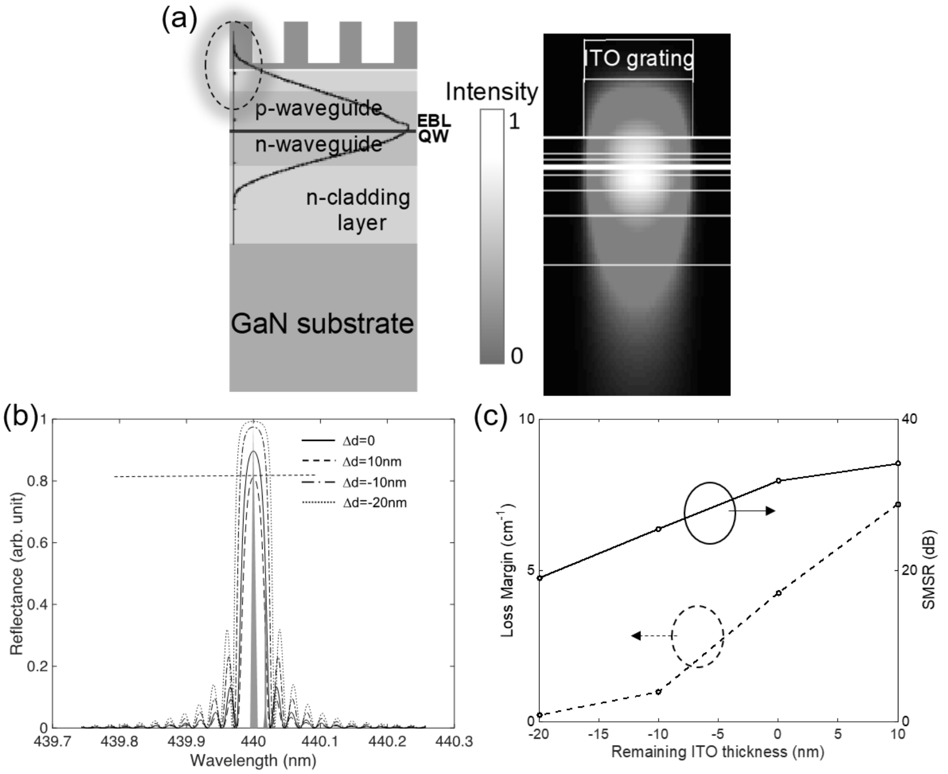

Figure 3.3. Black curve and the bright blue region shown in (a) indicates the intensity of the fundamental mode, where the penetration into ITO gratings can be seen (simulated in Fimmwave). (b, c) show the dependence of grating reflectance, loss margin and SMSR on the thickness of remaining ITO layer. A negative remaining thickness denotes the over-etching into GaN. Loss margin is defined as the difference between mirror losses of main and the first side mode.

hole wavefunction overlap and lower polarization-related electrical fields. To fully exploit this potential and combine the benefits from surface gratings and semipolar GaN, we firstly built on our laser structure on the ITO cladding based $(20\bar{2}\bar{1})$ epitaxial structure as optimized and detailed in the Chapter 2. To further the verify the strength of the coupling and understand the dimension requirement of the grating, we first use finite element method to estimate the important parameter, coupling coefficient κ. κ is historically an important parameter in determining the working condition of a DRB or DBR laser, and more specifically for a square wave conjugated grating, it can be defined as: as $\kappa = \frac{2\delta n}{\lambda}$, where δn is the index difference across the grating and λ is the Bragg wavelength. Since the index of the structure is directly dependent on the ITO fim thickness, therefore the coupling constant was presented here as a variable to the remaining thickness of ITO. As can be seen from Figure 3.3, the mode suppression ratio (MSR) is very senstive to the remaining ITO thickness.

A big challenge to realize single longitudinal mode operation with such semiconductor laser diodes is the very narrow spacing of Fabry-Perot (FP) modes arising from long cavity and shorter wavelength, one order smaller than in state of art InP laser diodes. In general, the lateral mode spacing for a semiconductor laser diode can be given as:

$$\Delta\lambda = \frac{\lambda^2}{2\, n_g L} \qquad (3\text{-}1)$$

Where the L is the cavity length, n_g is the group index and λ is the emission wavelength. Due to the much shorter wavelength, it can be expected that the mode spacing Δλ is at least 8 time smaller. To ensure the suitability of our DFB lasers for single wavelength operation, calculation of the coupling coefficient was made based on the effective modal indices, which were obtained using a two-dimensional (2D) optical mode solver Fimmwave [20] for both perturbed (etched) and unperturbed sections of the waveguide. Due to the small values of the interface effective index differences (about 0.1 ‰ for a single grating interface), the low reflection limit condition within coupled mode theory can be satisfied and the coupling constant κ and reflectance of the grating [Fig. 2(a)] can be readily calculated once the refractive indices of perturbed and unperturbed structure are known. Furthermore, the wavelengths for the fundamental mode and side modes can also be obtained from the characteristic equations [21] once the coupling constant is known, so the SMSR (side mode suppression ratio) can also be estimated.

B. Fabrication

This design used a self-aligned process to form a shallow ridge waveguide. The steps are as follows. A series of 2.5, 8 and 15 μm wide ridges with different lengths were then etched by Cl_2 reactive ion etching (RIE) oriented parallel to the projection of the c-axis, and a 225 nm self-aligned layer of SiO2 for ridge isolation was deposited using ion beam deposition and liftoff. Next, about 110 nm ITO was deposited on the top of the ridge by e-beam evaporation from an In_2O_3:SnO_2 90:10 wt % source. Later, a 35 nm SiO2 layer was sputter deposited as a hard mask. In the center area of the ridges the grating patterns with different pitches were then defined by electron beam lithography (JEOL JBX-6300FS system with 1 nm step resolution and 500 μm scan field), and such resist patterns were then transferred into the hard mask by CHF_3/CF4/O_2 inductively coupled plasma (ICP) etching. More specifically, the resist was then stripped, and the ITO gratings were formed using Ar/CH_4/H_2 (MHA) reactive ion etching. Nominally 100 nm of ITO was etched, and a 10 nm layer of ITO was left. A metal pad (Ti/Au) for probing was then deposited by e-beam evaporation on the ITO to the side of the ridge and extending up one sidewall to the unetched edge of the ridge top (∼1.5 μm) [Fig. 1(a)] for both better current conduction and suppression of the higher order lateral modes. Facets were later formed by chemically assisted ion beam etching (CAIBE) in Cl2 chemistry, which is optimized for forming laser facets on semipolar oriented GaN devices. During the lithography, due to the grating is written on the top surface of the ridge directly, the accurate height measurement and manual focus adjustment of the electron beam is necessary, and the grating pattern must be well aligned along the center of the ridge with a tolerance of less than 1 μm. A diffusion barrier of Ni was inserted between the Al and Au to maintain stability under testing. Additionally, the fabricated lasers was then be lapped to less than 120 um thick and

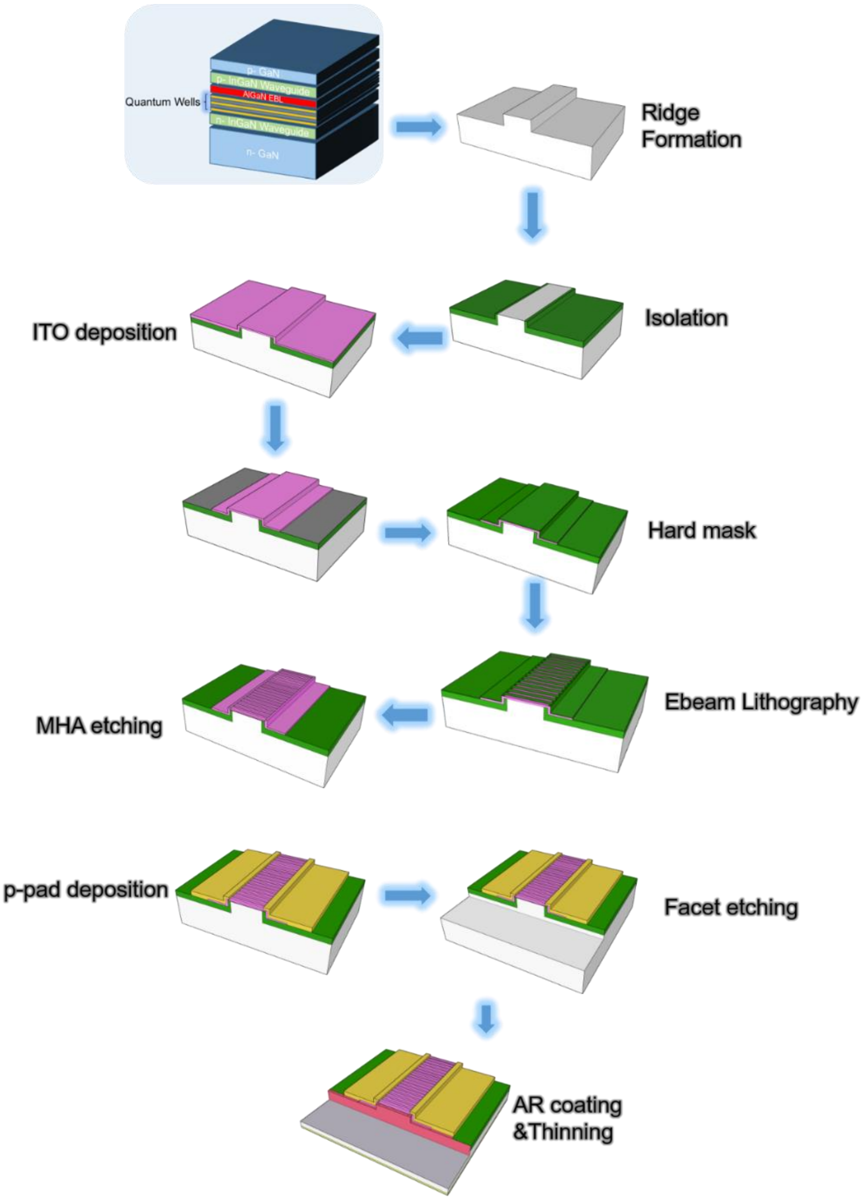

Figure 3.4. The complete process flow for the first generation DFB-LD with etched ITO gratings.

soldered to a heatsink to dissipate heat during testing to achieve CW operation. The lapping process was done on a customized polishing machine using 6 um lapping pad and 3 um diamond slurries. The lapped backside will then be further dry etched in RIE system for another 10 um to remove the damage layer caused by mechanical forces during polishing. Then an Al/Ni/Au metal contact was deposited on the RIE treated backside and Pd/Sn/Ag solder was then used to attach the fabricated laser bar to the heatsink. It is therefore necessary to provide alignment marks that will remain sharp following the ridge formation. The detailed process steps are outlined in Appendix.

In order to evaluate the duty cycle and to keep it close to 50%, I employed both scanning electron microscopy and atomic force microscopy. Both techniques are useful in providing information on the grating duty cycle. The AFM provides more quantitative analysis such as grating depth. This can aid in determining whether the etching is complete. The AFM cannot completely resolve the grating cross section due to convolution of the profile with the AFM tip shape. The tip quality varies and can mislead if one is not cautious. Planer view of SEM can also provide information on the duty cycle, yet SEM cannot provide this depth information as easily. Cross section images to verify depth are possible but the significant charging of the resist and ITO grating can still distort the results. This can be overcome by coating with thin conducting films, such as Pd/ Au mixtures, however this cannot be done on the actual samples.

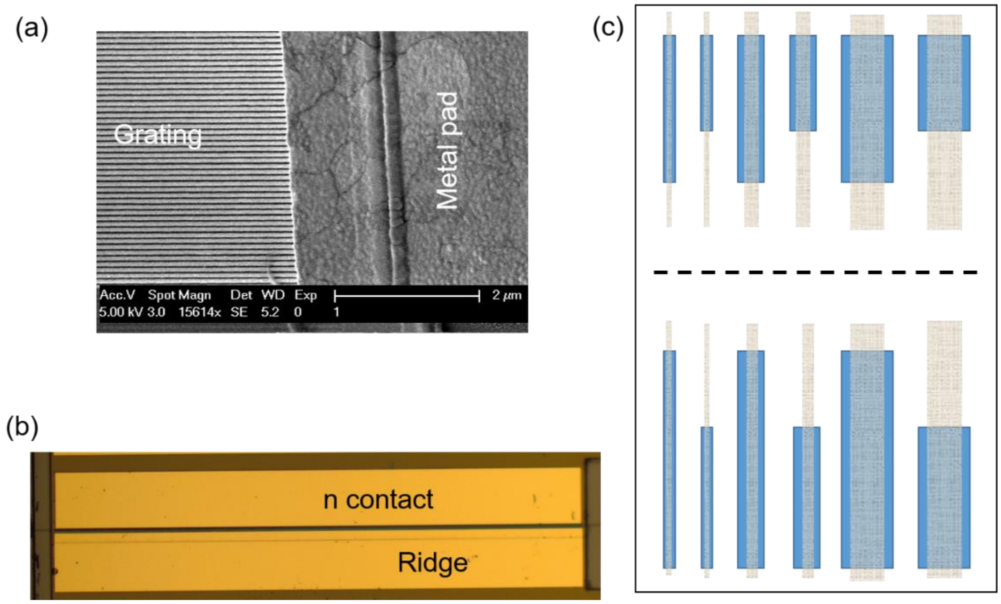

Figure 3.5. (a) the SEM image showing a laser ridge with metal contact on the ridge and grating on the top. (b) microscopic top view of a 1500 um long, 8 um wide laser diode. (c) A complete die for lithography during the process, each sample has about 4-5 dies in total. The blue areas denote the ridge, and the brown blurred ones are the where gratings are to be written.

C. Challenges of the process

Several challenges existed for the fabrication of the first-order DFB-LDs with etched gratings. In this section, they will be discussed in detail.

1. Optimization of the surface roughness of ITO

The dimension of grating requires ultra-fine focusing of the electron beam during lithography, which furthermore needs a very smooth surface. However, in general the surface of the e-beam evaporated ITO films is very rough, with a RMS roughness on the order of 0.5-6 nm, a transparency of ~90 % at 445 nm, Sputtered ITO can greatly reduce the surface roughness but more than often the p-GaN contact resistances are still much higher than the ebeam evaporated contacts (10^{-2}-10^{-3} $\Omega\cdot$cm), partially due to the powerful sputtering of indium atoms will damage the delicate p-GaN surface. Conventional deposition method requires the substrates to be heated. When ITO is deposited at room temperature, however, the films are typically smooth with < 1 nm RMS roughness, but unfortunately, they exhibit very poor optoelectronic properties, which would lead to large absorption losses. There are many reports on improving the optoelectronic properties of e-beam deposited ITO films by varying the post deposition annealing conditions, however annealing in RTA has been often reported to generate indium dots agglomeration making the surface unsuitable for grating fabrication.

The e-beam chamber we used for ITO deposition was a standard bell jar chamber. In_2O_3/SnO_2 (90/10 wt. %) source material purchased from Kurt J. Lesker was used as the evaporation source. The source to substrate distance was ~33 cm. Substrate heating was achieved using a custom-built resistive heater wired to a Variac AC controller. The maximum heater temperature was 400 degree Celsius. Samples were held using metal clips and the temperature was measured using a thermocouple inserted into the metal chuck between the heating block and the substrate. The chamber was evacuated to $< 3 \times 10^{-6}$ Torr before introducing O_2. The chamber pressure was controlled by the oxygen flow. After the deposition was completed, the O_2 flow and chamber pressure were held constant, then the samples were unloaded in atmosphere. The deposition rate was monitored in-situ using a quartz crystal monitor and ex-situ thickness measurements were made using a J. Woollam Spectroscopic Ellipsometer. We also measured some test samples using confocal microscopy and stylus profilometry to confirm the deposition rate measured by the QCM.

The ellipsometer measured thickness was used to calculate the resistivity from the 4-point probe measured sheet resistance. Prior to deposition, it is important that the surface gallium oxide layer was removed so each sample was dipped in 1:1 HCl:H_2O solution for 30 sec., and then rinsed in DI water. The ITO ellipsometer measurements were carried out at several different angles over a spectral range of 420 nm to 870 nm to get rid of the absorption peak noises. A J. Woollam model was used to analyze the measured psi, Ψ, and delta, Δ, vs. wavelength information.

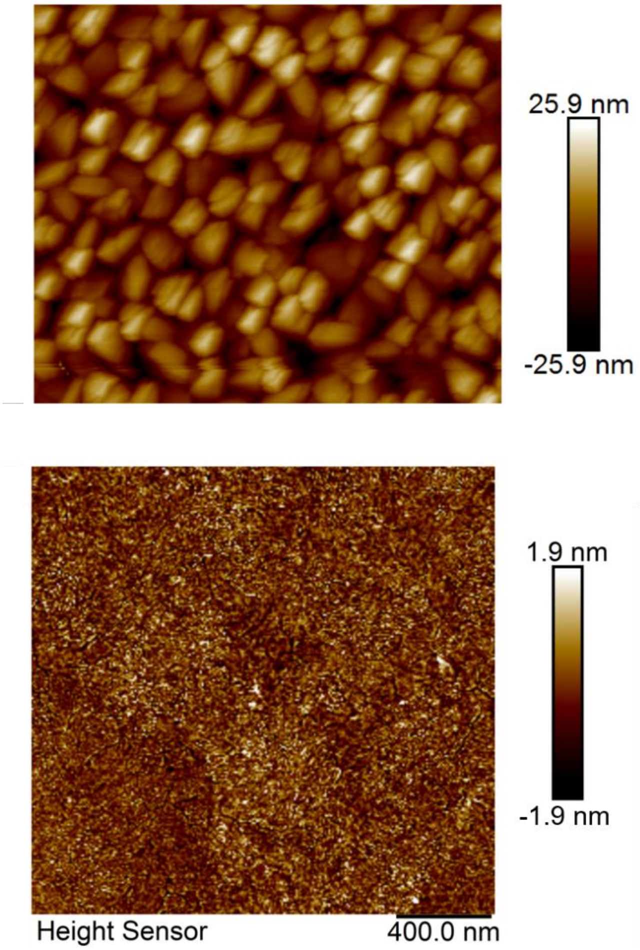

Figure 3.6. The AFM image showing the surface of ITO layer under different growth temperatures. The top one is regular 250 ℃ deposition, the bottom one is the result from two-step deposition (50℃ for the first 12 nm and 300℃ for the rest of thickness).

Previous studies have shown that the deposition temperature has a significant effect on the surface roughness. To analyze the dependence of the ITO film properties on the deposition temperature, 12 nm ITO films were deposited at 30 sccm O_2 flow at a rate of 0.1 Å/sec, over a range of temperatures from 25 to 400 degree C. Figure 3.7 summarizes the properties of the ITO samples from the temperature series. We find that below 100 degree Celsius, the films appear to be amorphous with large crystalline clusters. Similar results have been seen in previous studies where a crystallization temperature of ITO is close to the melting point of indium is commonly reported [21]. Additionally, some previous x-ray diffraction measurements

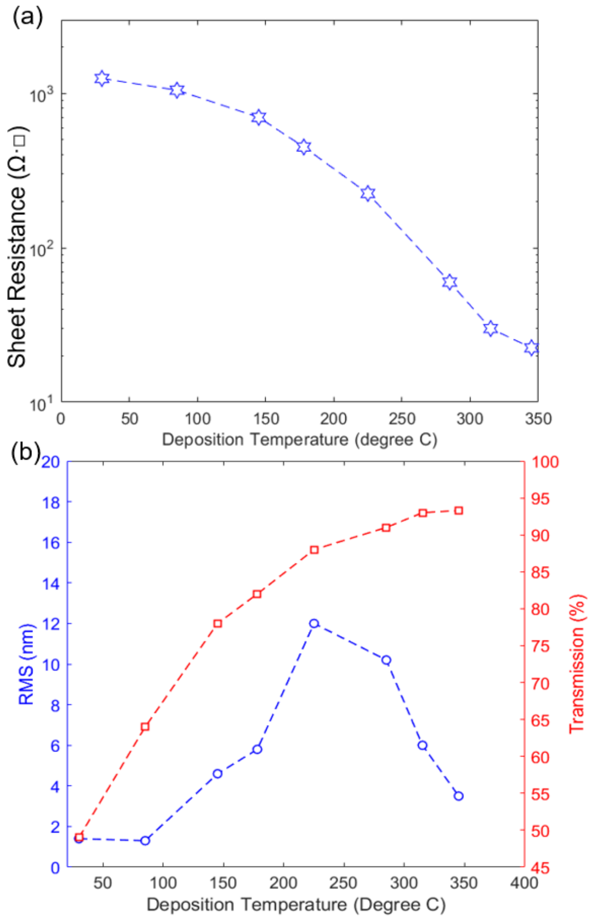

Figure 3.7. The temperature dependence of 60 nm ITO films deposited at 30 sccm O2 flow. (a) sheet resistance vs. temperature measured on ITO/DSP sapphire samples. RMS roughness, corresponding to the AFM images shown in Figure 3.5, and the % transmission at 445 nm (b).

also shows that low temperature ITO films are amorphous with small periodic crystalline island regions and large crystalline clusters are less common when the temperature is low.[22] Excluding the large crystalline clusters from the RMS roughness analysis, Figure 3.6 indicates that the amorphous regions on the films deposited below 100 ℃ have an RMS roughness of < 4 nm. Both figure 3.6 and Fig. 3.7 show the RMS roughness with the large crystalline clusters where one can see the crystalline clusters cause the RMS roughness to be > 4 nm for the 135 ℃. One another important feature we can see is that these low-temperature films also have a high resistivity as shown in Figure 3.7(a).

It can be expected that the crystallinity condition and the Sn concentration of the films will have an influence on resistivity. Moreover, previous studies have also suggested that increasing the deposition temperature may also increase the oxygen vacancy concentration, thereby contributing to the reduction in the resistivity observed with increasing temperature in Figure 3.7(a).

Considering the temperature effects on transparency, shown in Figure 3.7(b), we note that the transparency increases as temperature increases. This can be caused by a small increase in the crystallinity thus better surface smoothness of the ITO film. Starting from 135 ℃ near the melting point of indium, the crystallization starts, with a large number of grains surrounded by amorphous regions, as seen in Figure 3.6(a). At this temperature, the nucleation of grains leads to an increase of the surface roughness to >10 nm. As the temperature is increased further to 200 ℃, the grain size will continue to increase, and the amorphous regions will become fewer and fewer. At 200 ℃, the RMS roughness reaches its peak of around 12 nm (Fig 3.7(b)) Above 200 ℃ the RMS roughness begins to decrease. The decrease of the RMS can be attributed to the heat-induced grain separation, yet still needs further study and verifications.

2. Control of Over-etching into ITO

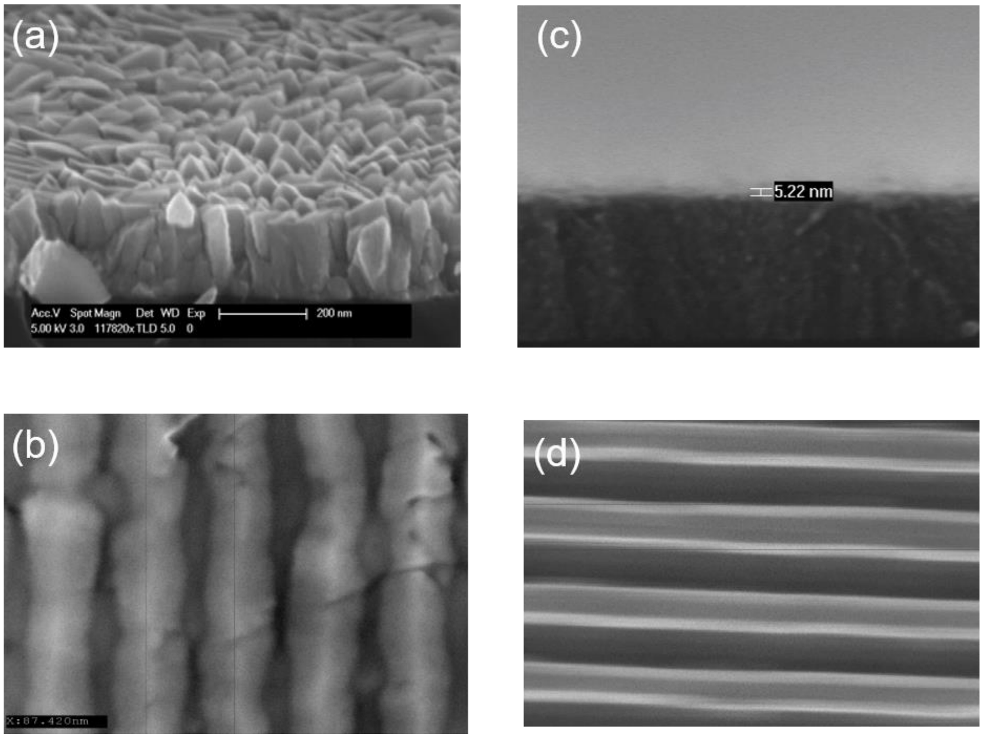

Figure 3-8 The SEM images of the surface and grating of (a,b) ITO deposited under normal heating (250℃) condition and (c,d) optimized two-step deposition

For the DFB-LDs with etched gratings, the remaining ITO thickness is important in our structure with regards to coupling strength and side mode suppression. An incompletely etched ITO layer can act as a current spreading layer and help improve the contact performance, yet with a lower coupling constant, while over-etching the ITO into the GaN can increase the coupling coefficient and grating reflectance but could potentially damage the p-GaN contact layer and increase the operating voltage. On the other hand, in the fabrication process, the gratings were formed from dry etching using a mixture of methane, hydrogen and argon, which also etches GaN aggressively once the ITO is etched completely. In addition, due to the microloading effect, dry etching leads to a non-uniform etching rate across the sample, which further reduces the yield of DFB-LDs. Fig. (3) shows the cross-sectional views of three types of gratings observed on the same sample under a stable etching condition. The SMSR reaches its maximum when ITO is fully etched but not over-etched, and as the etching

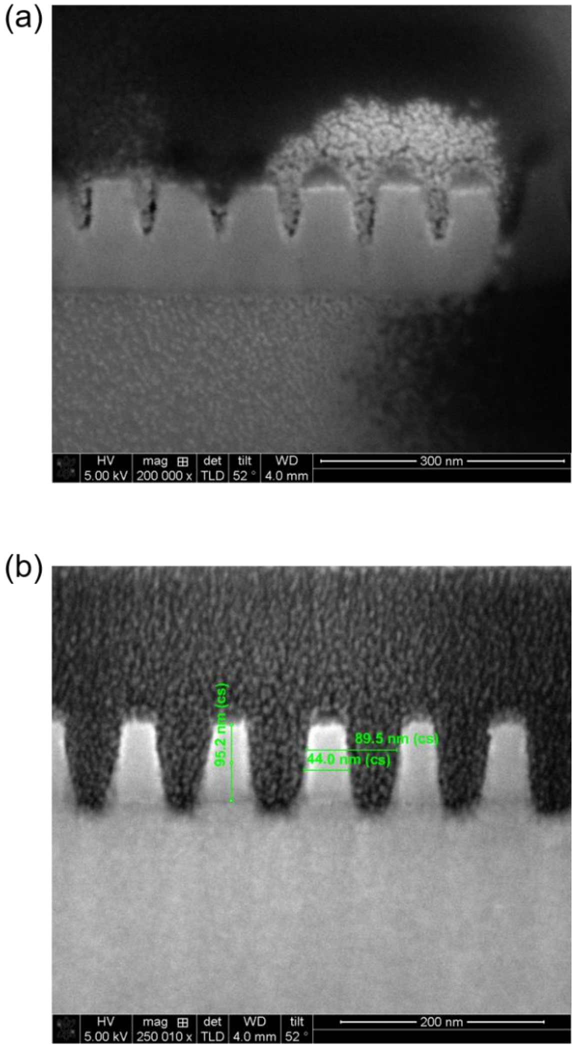

Figure 3-9 The focused ion beam image showing under-etched (a) and over-etched gratings (b). The dark background is from the platinum atoms redeposition.

Furthermore, overetching into the p-GaN damages the contact and increases the operating voltage. Therefore, it is beneficial to keep a very thin layer of unetched ITO. If the layer is under etched and too thick, the grating is too distant from the peak of the optical mode and the grating coupling constant becomes too low.

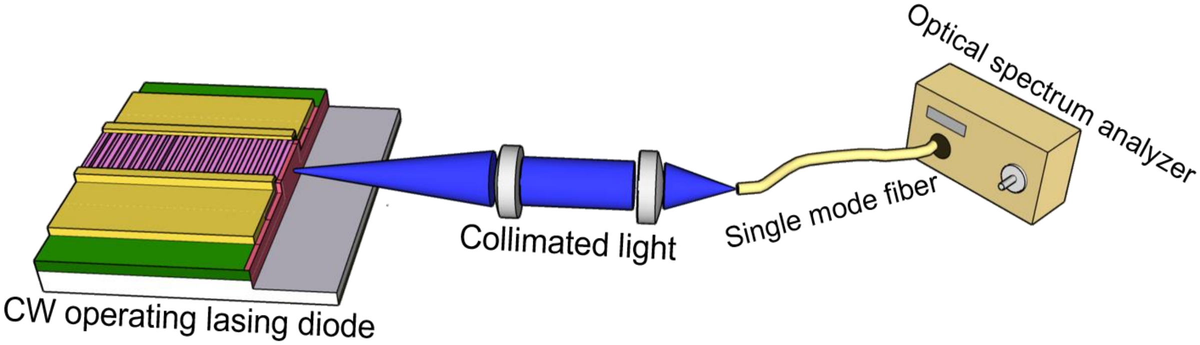

Figure 3-10 The testing setup for high resolution spectrum measurement

D. Performance of the lasers

The laser diode was tested in both pulsed and continuous wave operation. The emission spectra were obtained using a high-resolution optical spectrum analyzer (Advantest Q8347 with resolution of 1 pm near 440 nm). The laser current and voltage were measured using a Keithley 2400. source meter and output light was collimated and collected using an integrating sphere and calibrated silicon photodetector.

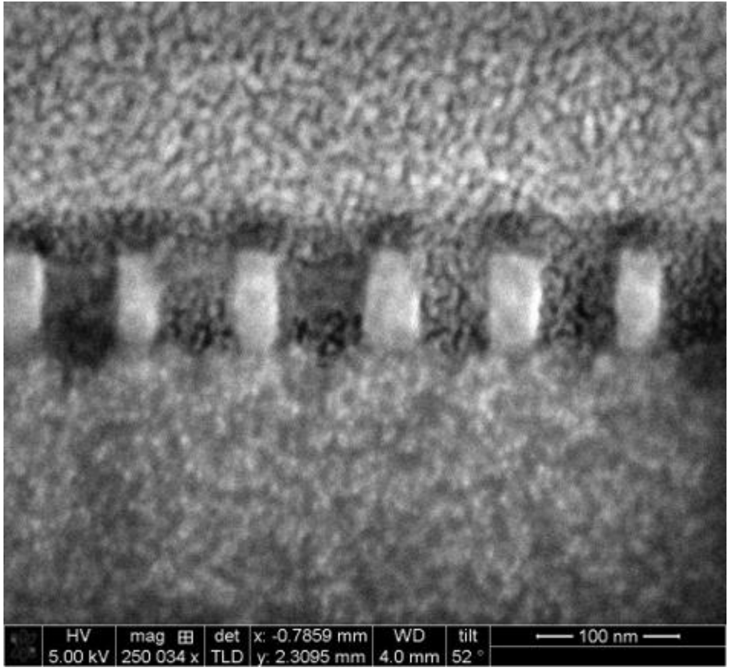

Figure 3-11 The 3D Schematic views of an etched grating DFB laser diode

The results of two different cavity lengths (1500/1800 µm) were studied here. For a 1500 µm long DFB-LD with grating period of around 89 nm and pitch size of 44 nm (about 50% duty cycle), the single mode emission spectrum at a drive current of 480 mA, and SMSR of 24 dB were obtained (Fig. 4). The spectral performance for a longer DFB laser diode is later shown in Fig. 7. It is also worth mentioning that from the spacing of the comb-shaped side FP modes, an important parameter–the effective group index ng can be calculated to be about 3.4. Under higher resolution mode, the FWHM (full width at half maximum) can be resolved to narrower than 5 pm.

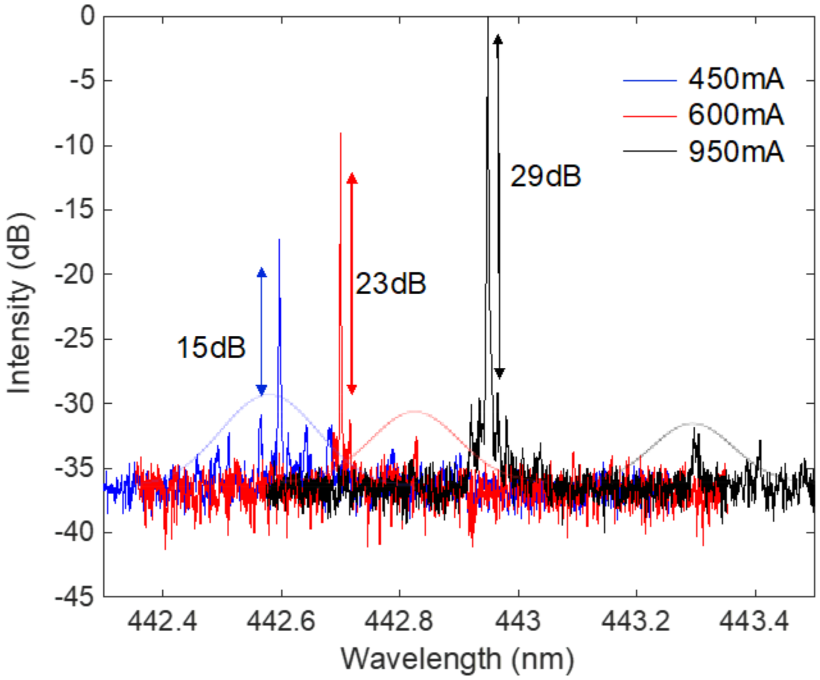

Figure 3-12 Spectra of a laser diode at different driving currents with the heat sink temperature fixed at 23°C. The laser cavity length/width is 1800 μm/8 μm, and threshold current is about 445 mA. At about twice of the threshold current, the mode suppression ratio is more than 29 dB. The spectra are offset 30 dB for clarity.

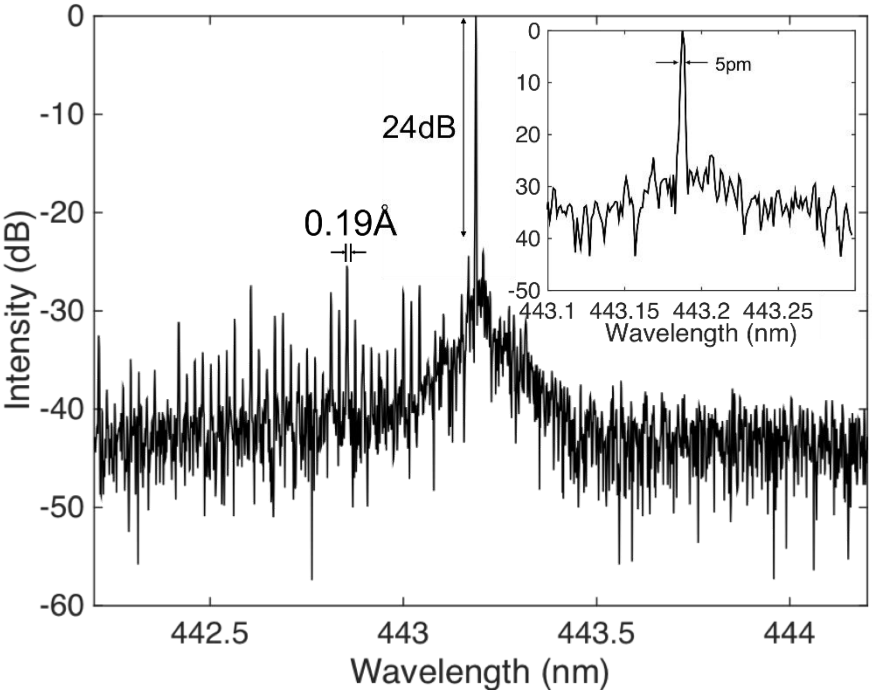

Figure 3-13 The mode comb spectrum of a lasing DFB-LD under room temperature (1500 µm long and 8 µm wide) with grating cycle of about 50% and period of 89 nm, at a drive current of 1.2 I_{th}.

The voltage and light output power versus current of a longer DFB laser diode (1800 µm long) is shown in Fig. 6. The measured threshold current was 445 mA, and the slope efficiency near threshold was 0.23 W/A for the AR coated facet (0.2 W/A for the uncoated facet). The optical output power rolled off at higher current due to self-heating, and the maximum power from the AR coated facet was more than 80 mW. The slope efficiency was twice lower than that of an equivalent FP semi-polar GaN laser diodes (0.45 W/A) [15], and the voltage was twice as high, probably due to reduced contact area and damage from the over-etched ITO and damaged p-GaN contact layers. Over-etching was confirmed by focused ion beam imaging of the grating [Fig. 3(a)]–the ITO is fully etched and a difference in color can be observed near the very top surface of GaN. It is worth noting that such damage was non-uniform along the ridge and the damaged layers. As seen from Fig. 2(a), although the coupling coefficient increases as the grating goes from under-etched to over-etched, the additional reflectance from the higher coupling coefficient only adds less than 15 percent of the total, given a uniform 10 nm GaN layer is etched, which implies that the main contribution of the reflectance of a lasing DFB-LD is still from the ITO gratings instead of GaN. Additionally, the SMSR starts to drop after the ITO is fully etched [Fig. 2(b)], which indicates that by accurately controlling the etching thickness one can even achieve a higher SMSR and better voltage performance. The devices were then tested under different drive currents with temperature being fixed by the temperature controller. Close to the lasing threshold, the FP modes are still observable near the single DFB mode at 442.6 nm. As the current continues to increase, the side mode suppression ratio gets enhanced, and due to self-heating the DFB and FP modes are all red sifted. At near twice the threshold (880 mA), the mode suppression ratio reaches 29.3 dB (Fig. 7).

Another important feature of DFB-LD is its wavelength stability with temperature. To verify the weak temperature dependence, a series of spectra were measured from 12°C to 40°C while keeping the current fixed at 600 mA (Fig. 8). The laser was operating in single mode over the whole temperature range and a small red shift of the DFB mode was observed as expected from the variation of refractive index.

The temperature dependence is calculated to be about 0.013 nm/K, which is similar to what has been observed in literature on other GaN DFB-LDs [9]. On the other hand, the shift of the gain spectrum (gain detuning) is normally much faster than the DFB mode (about 0.03 nm/K). As a result, when the device temperature increased, the peak intensity decreased due to lower gain at the DFB mode and higher internal loss from the required higher carrier densities needed to reach threshold, and the mode suppression also degraded as a result from misalignment between the gain peak and grating filter center.

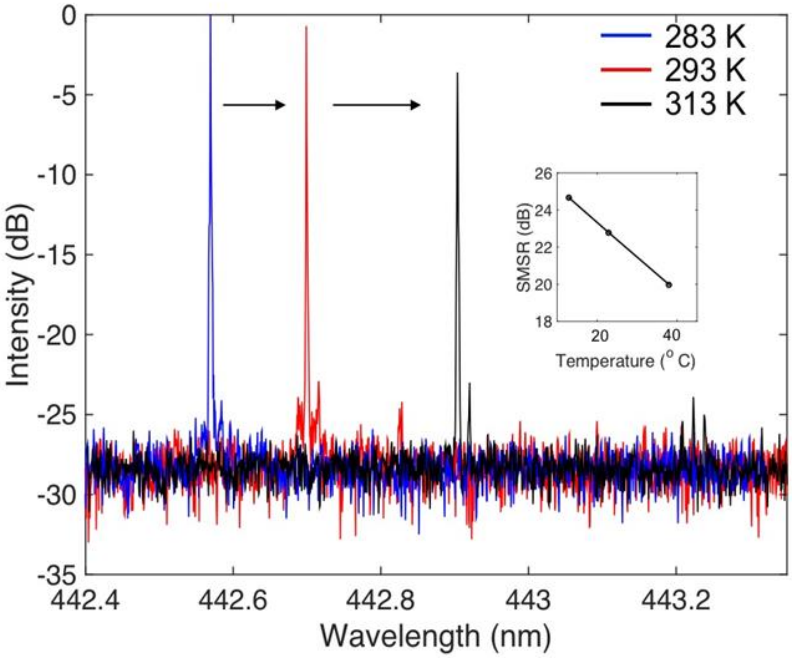

Figure 3-14 The temperature dependent spectra of a laser diode (1800 µm long and 8 µm wide) from 283 K up to 313 K while keeping current fixed at 600 mA. The spectra are offset 30 dB for clarity.

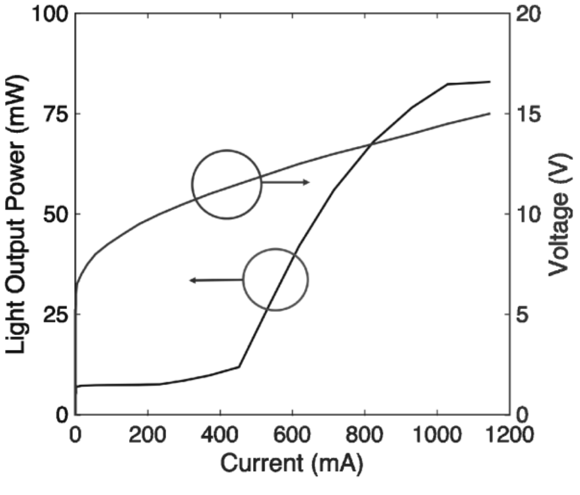

Figure 3-15 The CW L-I and V-I characteristics of a DFB laser diode from AR coated facet (1800 µm long and 8 µm wide) at a heat sink temperature fixed at 293 K.

References:

[1] S. Nakamura, M. Senoh, S. Nagahama, N. Iwasa, T. Yamada, T. Matsushita, H. Kiyoku, and Y. Sugimoto, “InGaN-Based Multi-Quantum-Well-Structure Laser Diodes,” Jpn. J. Appl. Phys., vol. 35, pp. L74–L76, 1996.

[2] C. Lee, C. Zhang, M. Cantore, R. M. Farrell, S. H. Oh, T. Margalith, J. S. Speck, S. Nakamura, J. E. Bowers, and S. P. DenBaars, “4 Gbps direct modulation of 450 nm GaN laser for high-speed visible light communication,” Opt. Express, vol. 23, no. 12, p. 16232, 2015.

[3] J. J. Wierer, J. Y. Tsao, and D. S. Sizov, “Comparison between blue lasers and light-emitting diodes for future solid-state lighting,” Laser Photon. Rev., vol. 7, no. 6, pp. 963–993, Nov. 2013.

[4] A. Pourhashemi, R. M. Farrell, M. T. Hardy, P. S. Hsu, K. M. Kelchner, J. S. Speck, S. P. Denbaars, and S. Nakamura, “Pulsed high-power AlGaN-cladding-free blue laser diodes on semipolar (20-2-1) GaN substrates,” Appl. Phys. Lett., vol. 103, p. 151112, 2013.

[5] W. W. Chow and M. H. Crawford, “Analysis of lasers as a solution to efficiency droop in solid-state lighting,” Appl. Phys. Lett., vol. 107, no. 14, p. 141107, 2015.

[6] L. Y. Kuritzky and J. S. Speck, “Lighting for the 21st century with laser diodes based on non-basal plane orientations of GaN,” MRS Commun., vol. 5, no. 3, pp. 463–473, 2015.

[7] S. Masui, T. Miyoshi, T. Yanamoto, and S. Nagahama, “Blue and green laser diodes for large laser display,” in 2013 Conference on Lasers and Electro-Optics Pacific Rim (CLEOPR), 2013, p. SA1-3.

[8]. J.H. Kang, H. Wenzel, V. Hoffmann, E. Freier, L. Sulmoni, S. Einfeldt, T. Wernicke, M. Kneissl, and R.-S. Unger, Novel In-Plane Semiconductor Lasers XVII (2018).\

[9]. T.J. Slight, S. Stanczyk, S. Watson, A. Yadav, S. Grzanka, E. Rafailov, P. Perlin, S.P. Najda, M. Leszczyński, S. Gwyn, and A.E. Kelly, Appl. Phys. Express **11**, 112701 (2018).

[10]. Y. Lu, W. H. Guo, R. Phelan, D. Byrne, J. F. Donegan, P. Lambkin, and B. Corbett, IEEE Photonics Technol. Lett. **18**, 2605 (2006).

[11]. W.G. Scheibenzuber, U.T. Schwarz, R.G. Veprek, B. Witzigmann, and A. Hangleiter, Phys. Rev. B **80**, 115320 (2009).

[12]. Y. Zhao, Q. Yan, C.-Y. Huang, S.-C. Huang, P.S. Hsu, S. Tanaka, C.-C. Pan, Y. Kawaguchi, K. Fujito, C.G.V.D. Walle, J.S. Speck, S.P. Denbaars, S. Nakamura, and D. Feezell, Appl. Phys. Lett. **100**, 201108 (2012).

[13]. F. Feezell, J.S. Speck, S.P. Denbaars, and S. Nakamura, J. Disp. Technol **9**, 190 (2013).

[14]. K.W. Yoon and N.Y. Ha, Opt. Express **24**, 516 (2016).

[15]. S. Mehari, D.A. Cohen, D.L. Becerra, S. Nakamura, and S.P. Denbaars, Opt. Express **26**, 1564 (2018).

[16]. S. Mehari, D.A. Cohen, D.L. Becerra, S. Nakamura, and S.P. Denbaars, Jpn. J. Appl. Phys **58**, 020902 (2019).

[17]. A. Myzaferi, A. H. Reading, D. A. Cohen, R. M. Farrell, S. Nakamura, J. S. Speck, and S. P. Denbaars, Appl. Phys. Lett. **109**, 061109 (2016).

[18]. L.Y. Kuritzky, D.L. Becerra, A.S. Abbas, J. Nedy, S. Nakamura, S.P. Denbaars, and D.A. Cohen, Semicond. Sci. Technol **31**, 075008 (2016).

[19]. H. Zhao, S. Pinna, B. Song, L. Megalini, S.T.S. Brunelli, L.A. Coldren, and J. Klamkin, IEEE J. Sel. Top. Quantum Electron **24**, 1 (2018).

[20]. A. Choudhury, T. Stanczyk, D. Richardson, A. Donval, R. Oron, and M. Oron, IEEE Photonics Technol. Lett. **17**, 1881 (2005).

[21]. L.A. Coldren, S.W. Corzine, and L.M Mashanovitch, Diode Lasers and Photonic Integrated Circuits, Wiley, pp. 602-603, New York (2012).

[22]. J.A. Hoffnagle, W.D. Hinsberg, M. Sanchez, and F.A. Houle, J Vac Sci Technol B Nanotechnol Microelectron **17**, 3306 (1999).

IV. Third order distributed feedback laser diode with imbedded dielectric grating

In the previous chapter, we talked about that challenges of the etched surface grating. The difficulty in controlling the etching makes the process complicated and, in this chapter,, we will focus on a design with a non-etched approach, which can theoretically boost the voltage performance. In addition to that, we are also going to explore different designs to enhance the performance as well as different characterizations to better understand the properties arising from the III-nitride laser diodes.

A. Imbedded Grating Design and Fabrication

The DFB-LD structures presented here were grown by MOCVD deposition on free-standing bulk semipolar ($20\overline{2}\overline{1}$) n-GaN substrates using the same expitaxy recipe introduced in Chapter 2 and 3 which included a double quantum well structure and symmetrical InGaN waveguides. The substrates were then processed into surface grating DFB-LDs following two different approaches. The first approach is our reference sample, as shown in Fig. (1a)-a thin 250 nm p-GaN cladding was epitaxially grown on the top of the waveguide documented after the 100 nm ITO was deposited onto p-GaN, the gratings in the ITO layer were formed using Ar/CH4/H2 reactive ion etching and a probing pad was deposited only on the sides of the ridges without directly contacting the gratings to avoid the absorption loss from the metal. In the second approach, In the modified third-order grating structure, the thickness of the p-GaN cladding layer was reduced to 200 nm to increase the optical mode overlap to compensate for the reduced Fourier component of the third order grating. Following the epitaxial growth, the samples were then processed into a DFB-LD structure with an embedded surface grating (Fig 1(a, b)). After the laser ridge was formed, a thin (~10 nm) layer of ITO was first deposited on the p-GaN. During the deposition, the substrate wafer was kept at 50 degree C to ensure the smoothness of the surface. Then the samples were spin-coated with 30 nm hydrogen silsesquioxane (HSQ) resist and three different types of grating patterns were written by e-beam lithography, which will be detailed in the next section. To keep the testing thermally stable, a thermoelectric temperature controller was connected to the stage to maintain stage and heat sink at the desired temperature. For both approaches, an anti-reflective coating was deposited on one facet to break the degeneracy of the modes. For the lasers fabricated using the first approach, both pulsed and continuous-wave (CW) electrical injection were employed in the testing and the pulsed electrical and luminescence characteristics were measured using a pulse width of 1 μsec with a repetition rate of 10 kHz. To measure the CW spectrum, the light was coupled into a single mode fiber and fed into a high-resolution optical spectrum analyzer Advantest Q8347 with resolution of 1 pm at 440 nm (For pulsed spectra, an Ando AQ6315A spectrometer with resolution of 0.05 nm at 440 nm was used). For both the pulsed and CW light, the light output power was measured by collecting the light emitted with a calibrated Si photodiode and integrating sphere.

Instead of directly etching gratings into the ITO layer, gratings can be deposited by normal lift-off technique, yet for first order gratings, the scale (89 nm pitch size, 50% duty cycle) is difficult to achieve using conventional lift-off techniques. Therefore, another route was employed to create the imbedded gratings. Hydrogen silsesquioxane (HSQ) has been widely used as a negative resist in electron beam lithography (EBL) and also hard mask material during ICP dry etching for nanoscale device fabrication due to its high resolution and high etching resistance. Previously, ultra-dense nanometer-scale gratings using HSQ has been reported on various substrates.[1] It has a relatively low refractive index compared to GaN and can be annealed up to 450 ℃. In our design, after the HSQ gratings were formed by EBL, they were immediately annealed at 400°C for 5 mins in N_2/O_2 atmosphere. During the annealing process the HSQ condenses and transforms into SiOx, which is an ideal low refractive index material (compared to ITO) to induce variation in refractive index. Then another layer of ITO was deposited to imbed the p-GaN and gratings (Fig. 4-1(a)) and a probing pad of Ti/Au was later deposited, covering both the top and side of the ridges.

From Chapter 3, we have shown that the surface morphology of ITO is important to the yield and outcome of this process. Besides the previously reported two-step temperature

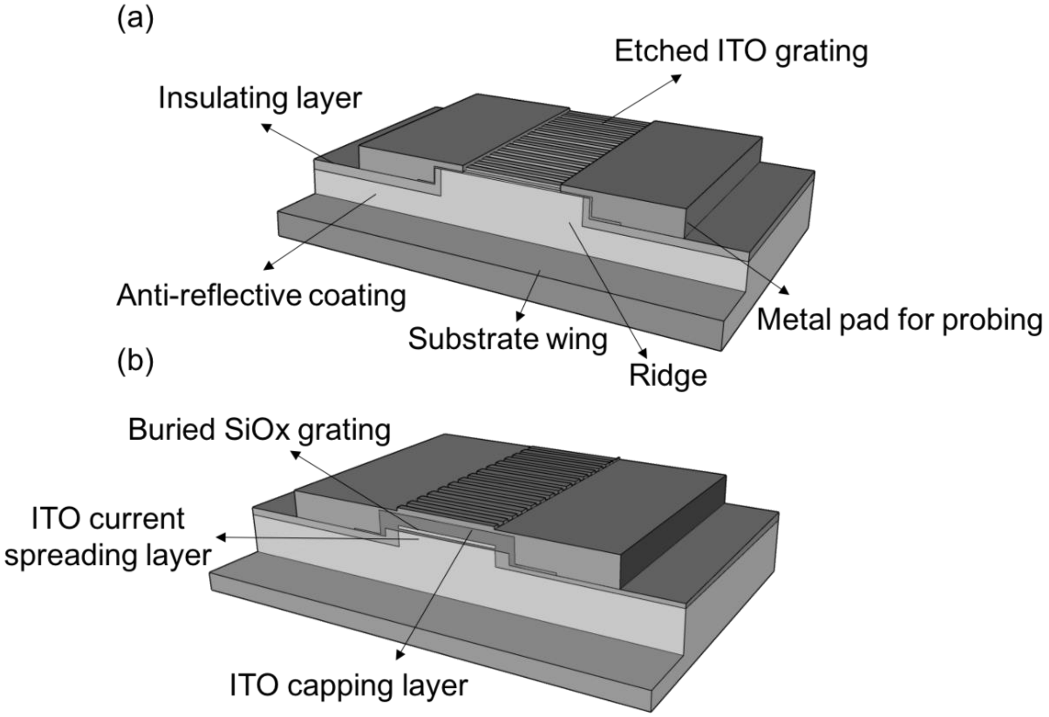

Figure 4-1 The 3D Schematic views of an etched grating DFB laser diode (a) and an imbedded grating DFB laser diode (b).

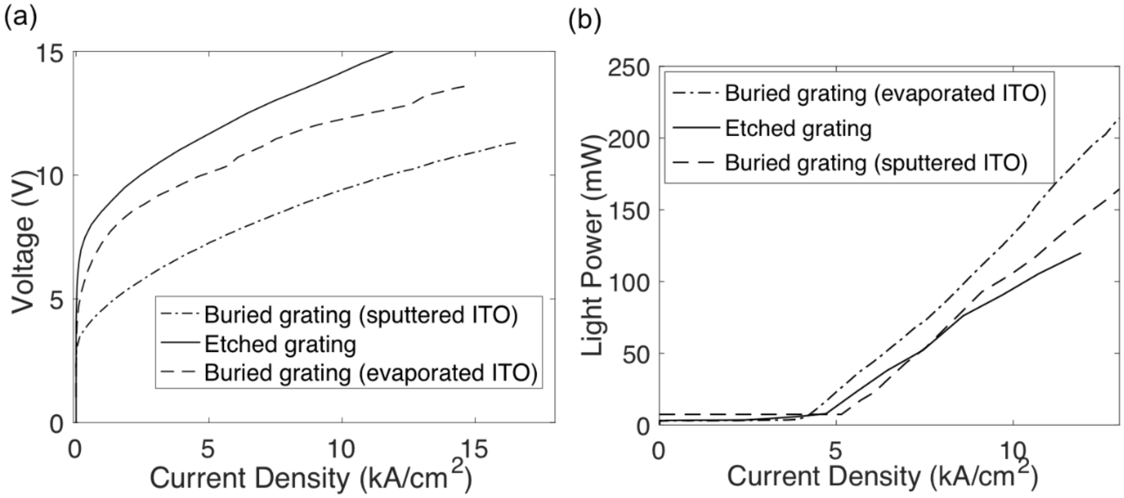

Figure 4-2 Solid-source ECR deposition system (MES-AFTY AFTEX-7600R). Substrate holder rotates during deposition and the temperature was varied by a ramp heater.

method to deposit smooth ITO by ebeam evaporation, during our second-generation development of DFB-LDs, electron cyclotron resonance (ECR) sputtering was also experimented as an alternative to deposit high-quality ITO. Microwave electron cyclotron resonance (ECR) plasma enhanced sputtering is an advanced deposition technique developed during the last decade. [2-4] Ionization and excitation led by a microwave ECR discharge can create a very low working pressure (10^{-5} Pa), and in an atmosphere of high reactivity of the molecular gas. A number of examples of the beneficial influence of the microwave ECR plasma enhancement of the sputtering discharge on the deposition of various types of thin films can be found in the literature. [6-8] As shown in Figure 4, comparing the L-I-V curves of the LDs with etched and buried grating structure, we find a significant reduction (~37%) in the threshold voltage from about 10.8 V to 6.5 V in the new design with e-beam evaporated imbedded grating structure, which can be attributed to the better protection of p-GaN contact layer. However, the improvement of sputtered imbedded gratings is not as significant. It is highly possible that the high RF sputtering have damaged the contact due to atoms bombarding, yet more study is needed to understand the detailed mechanisms. A reduction of the damage can be expected from a lower RF power deposition. Moreover, annealing has been shown to be effective to slightly recover the degraded voltage performance.

We can also see an increase in power output and slope efficiency for both imbedded gratings compared to etched gratings and such results can be attributed to lower optical loss (in the etched grating structure, part of the metal pad is in contact with p-GaN along the top edges of the ridge for current conduction) and better current spreading from the covered ITO layer.

B. Grating design

There are many different types of grating. Uniform grating is the one that we used in the first-generation DFB-LDs, and it is the easiest to be fabricated and can also be fabricated using conventional i-line lithography. In general, due to the symmetricity of the design, such type of DFB is antiresonant, and therefore there is no solution at the Bragg frequency. No discrimination can be created from such a design therefore asymmetrical facet has to be used for single mode emission. The phase differences arising from the cleaved facets could be significant enough to enhance the mode suppression properties but often lead to low yield. Gain-coupled DFB can be a solution to such an issue by introducing imaginary part into the

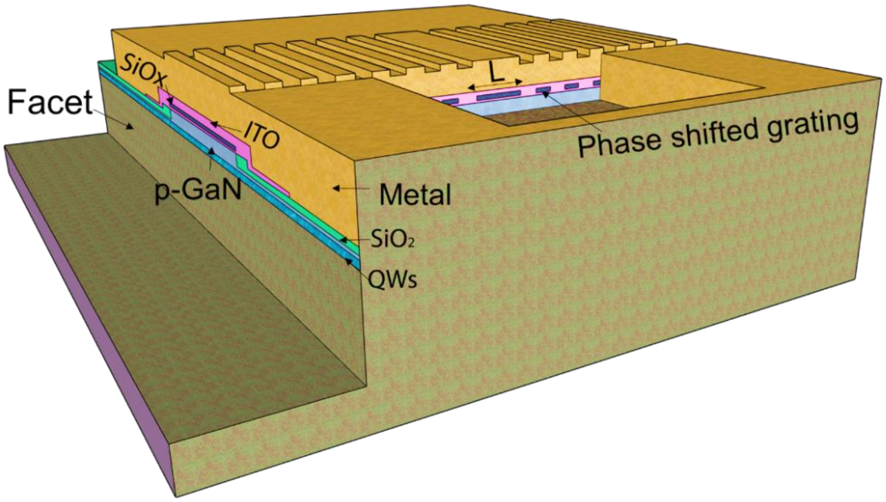

Figure 4-3 The 3D Schematic views of an etched grating with a phase shifted grating design. The L denotes the shift length located in the center of the cavity.

refractive index perturbation. For example, the grating could consist of alternate sections of index n_1 and index $n_2 = n_1 + jn_i$; (by definition, $n_i = g\lambda/(4\pi)$ for added gain). Then, the reflection r at each discontinuity, $r = jn_i/(2n_1)$, and the net grating reflection, r_g, at the Bragg frequency can be purely imaginary, and thus pure gain coupling can be realized. Even though

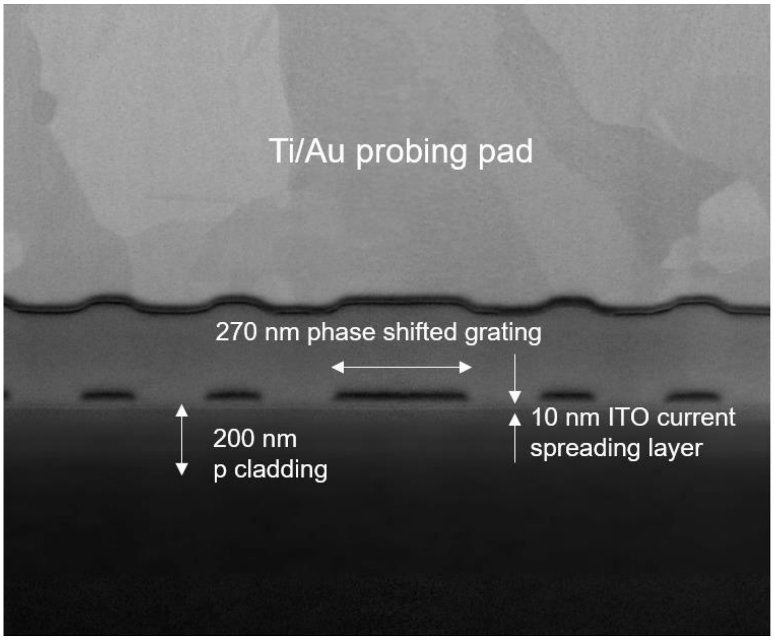

Figure 4-4 Focused ion beam imaging of a third order grating with a λ/4 shift in the center of the cavity.

such approach is possible, gain-coupled DFB-LDs often requires either the direct regrowth or loss coupled into the active region, which unavoidably increases the complexity of the structure. On the other hand, phase shift grating design has been widely used in conventional InP or GaAs DFB-LDs. By inserting a quarter wavelength grating into the center of the cavity, the threshold solution can be existing near the Bragg condition.

To better compare the properties of DFB-LDs with and without phase shifts, numerical simulations are firstly conducted based on transfer matrix method and traveling wave laser model (TWLM) and Lumerical software, where more details can be found in Ref. 19 and 20. The Figure 4-5 shows how the threshold gain and mode suppression ratio could vary due to the gradual increase of the grating length, implying the performance improvement from a standard to a quarter-wave-shifted design.

In our experiments, the quarter-wavelength shift DFB grating was fabricated following the similar process flow as the previously introduced embedded grating one. A shift was added into the middle of the cavity during ebeam lithography writing process. Three grating designs were studied in the experiments, the reference sample with first order grating and 250 nm

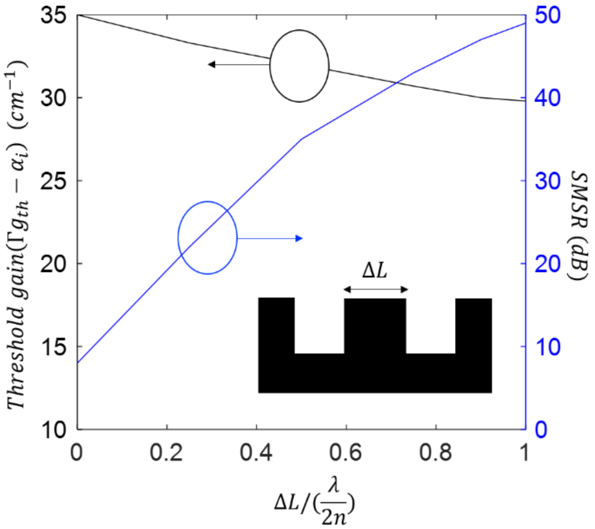

Figure 4-5 Dependence of side mode suppression ratio and threshold modal gains for the first mode as the length of the shift (ΔL) in the center of the cavity varies.

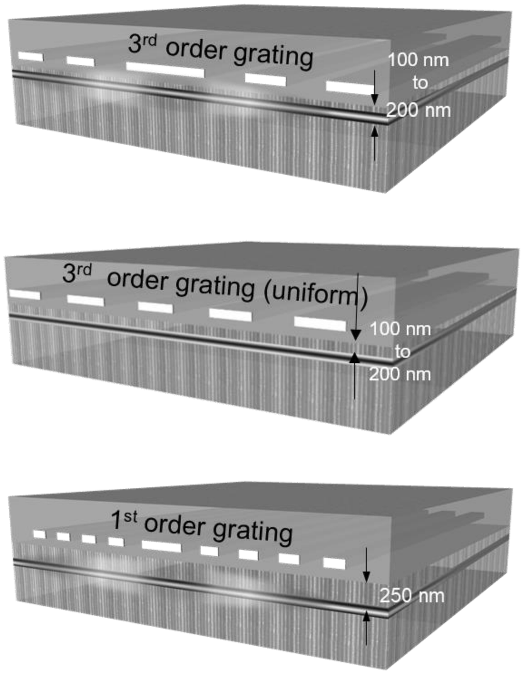

Figure 4-6 Three grating designs used in our experiments.

thick p-GaN cladding, the modified 3rd order grating sample with 200 nm thick p-GaN cladding with and without phase shifted grating. (Figure 4-6) Typical spectral and light–current–voltage (L–I–V) characteristics of the fabricated DFB-LDs at room temperature are shown in Fig. 4-10 (a). A pronounced impact was observed on both the spectra and light output characteristics resulting from the variations in the grating design. We found that by thinning the p-GaN cladding layer and increasing the grating order, the threshold current density increased from 2.7 kA/cm^2 to 3.8 kA/cm^2 and the threshold voltage decreased from 5.9 V to 5.5 V. The 0.4 V voltage improvement in the third-order grating contributed from the thinner 200 nm p-cladding layer is consistent with previous reports on 250 nm p cladding layer GaN laser diodes. The slope efficiency also slightly decreased from 0.9W/A to 0.81 W/A. In general the operating voltage (V_{op}) and output power of all the devices in this work have been significantly improved compared to the previous results on blue DFB-LDs with etched gratings [19], indicating the superiority of the embedded grating as an approach to protect the delicate p-GaN contact layer. On the other hand, a slight yet consistent difference on the threshold current was observed with and without a λ/4 shift. Furthermore, the optical output power rolled off at higher current densities due to self-heating. The maximum power output was more than 500 mW for first order DFBs, and more than 400 mW for the third-order ones regardless of the phase shifts.

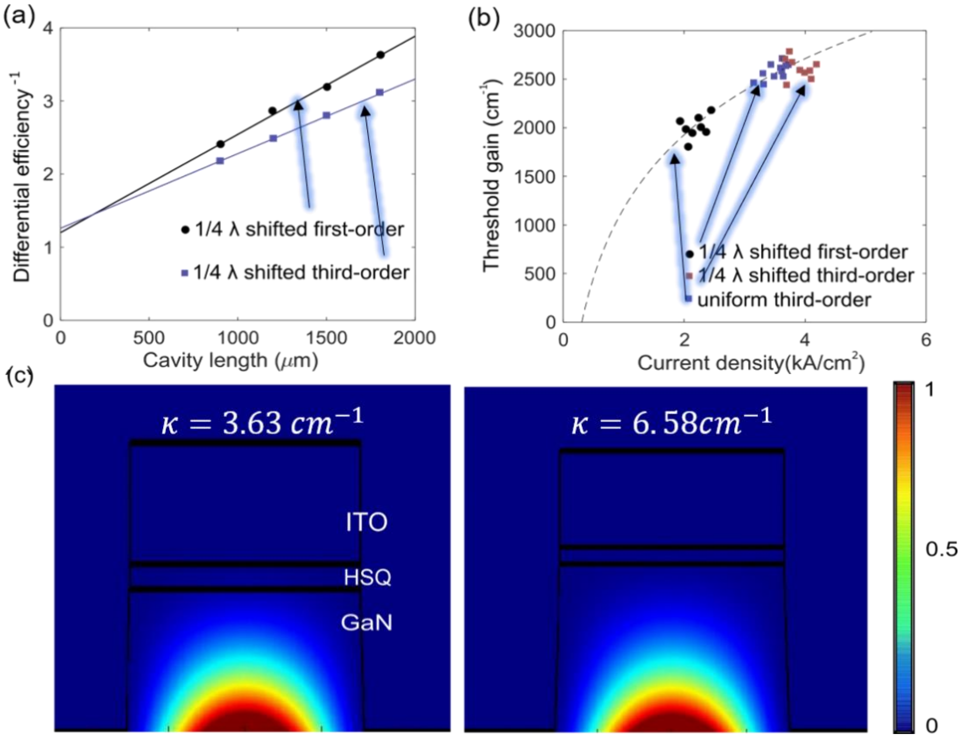

Figure 4-7 (a) The inverse differential efficiency of different LDs as a function of cavity length. (b) Gain threshold versus injected current density for different DFB-LDs' designs. The dashed lines are the two parameters exponential fits. (c) The FEM simulation of the mode profiles showing the fundamental mode penetrates into the HSQ layer for the third-order (left) and first-order (right) designs. Here we assume the refractive indices of ITO, HSQ, and GaN to be 2, 1.4 and 3.4 respectively. The κ values on the bottom represent the calculated coupling constants of two structures.

To determine the LDs' internal parameters, the dependence of output power versus injection current on cavity lengths was examined. Characteristics of the LDs with cavity lengths varied from 900 to 1800 μm were evaluated. The mirror loss $\langle\alpha_m\rangle$ can be expressed in terms of cavity length L and the mean mirror intensity reflection coefficient R as $<\alpha_m>=1/L\cdot In(1/R)$, and then the reciprocal differential efficiency ($1/\eta_d$) can be expressed as:

$$\frac{1}{\eta_d} = \frac{<\alpha_i>}{\eta_i In(\frac{1}{R})} L + \frac{1}{\eta_i} \quad \text{(4-1)},$$

where $<\alpha_i>$ is the internal loss and η_i is the injection efficiency. By fitting the $1/\eta_d$ at different L, we can obtain $<\alpha_i>$ and η_i. A linear fitting to$1/\eta_d$ versus L was used to extract η_i and $<\alpha_i>$ from the intercept and the slope, respectively. The injection efficiency and the optical loss for each sample were extracted from the intercept and the slope using cavity length method as shown in Fig. 4-7(a). In such extrapolation, we assume the uncoated facet reflectivity of all three samples is 0.18, which was based on simulated modal refractive indexes. From the extrapolation, we found that the internal loss increased from about 14 cm^{-1} to 19 cm^{-1} as we switched from first order grating to the third order grating with thinner p-GaN. Considering that the grating material HSQ itself has very low absorption coefficient at visible wavelengths, and should have no significant impact on the internal loss, we conclude that such difference arises from the deeper optical mode penetration into the lossy ITO layer due to the reduced thickness of p-GaN cladding layer. To verify such effect, segmented contact measurement was also conducted as shown in Fig 4-8. The amplified spontaneous emission (ASE) spectra for$_i$ $\Gamma g-<\alpha_i>$ under different injection current densities are shown in Figs. 4-8(a) and (b), respectively. The $<\alpha_i>$ can be derived from the stable plateau formed at the long wavelength side of the spectra and it was measured to be around 19 cm^{-1} for a 250 nm p-cladding layer laser, which agrees well with the $<\alpha_i>$ of 16 cm^{-1} obtained from the cavity length analysis above. As the thickness reduces from 250 to 200 nm, the optical loss increases to 25 cm^{-1}. This observation agrees with the previous work that shows reducing the p-GaN cladding layer could lead to an efficiency degradation. Such effects are likely to be more

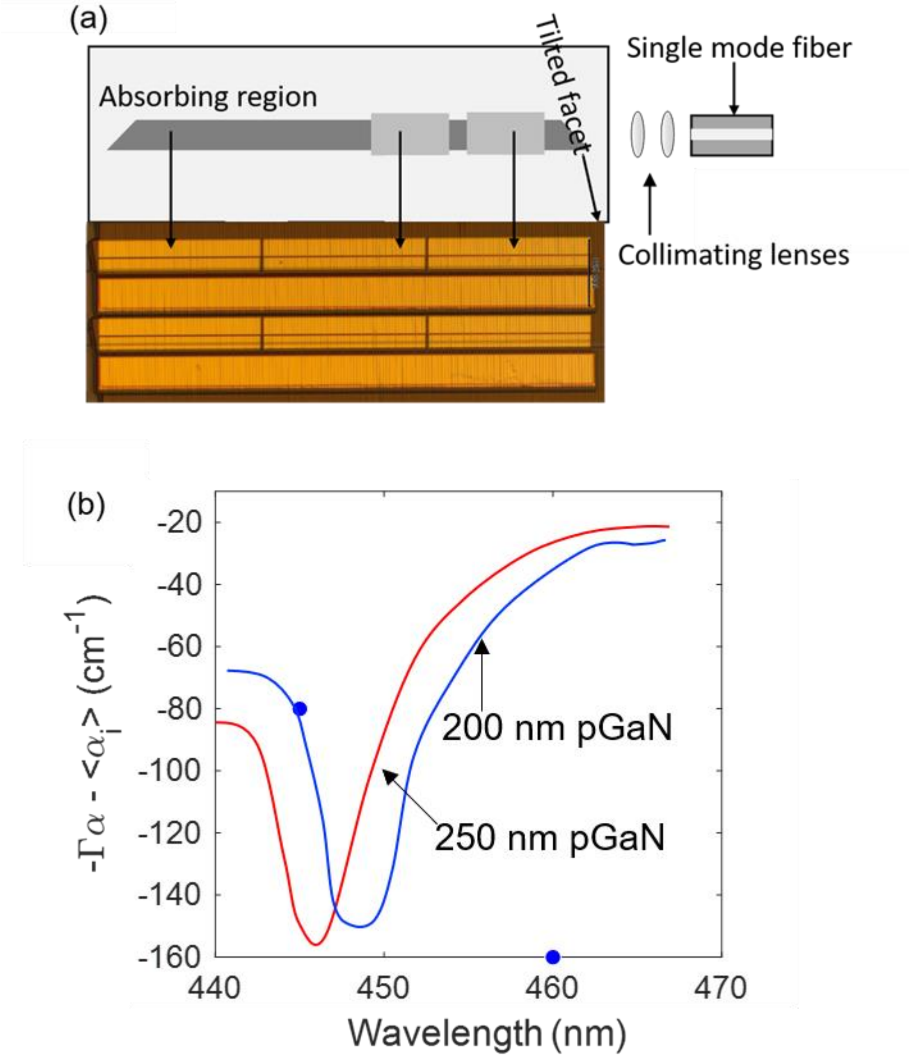

Figure 4-8 (a) Top-view illustration of the segmented contacts structure and optical setup, (b) absorption curves of LDs with a 250 nm and a 200 nm p-GaN thickness measured at 2 kA/cm^2.

prominent here due to the low-temperature ITO deposition method used for the first 10 nm deposition. Simulated optical mode profile simulations further shows that if the additional 5 cm^{-1} loss originated entirely from ITO absorption, the material absorption coefficient would have to be 3000 cm^{-1}, rather high for ITO at this wavelength and implying that there is a significant room for improvement. Finite Element Method (FEM) simulations (Fig. 4-7) and the refractive index difference method [13] further reveal that even with a higher mode overlap

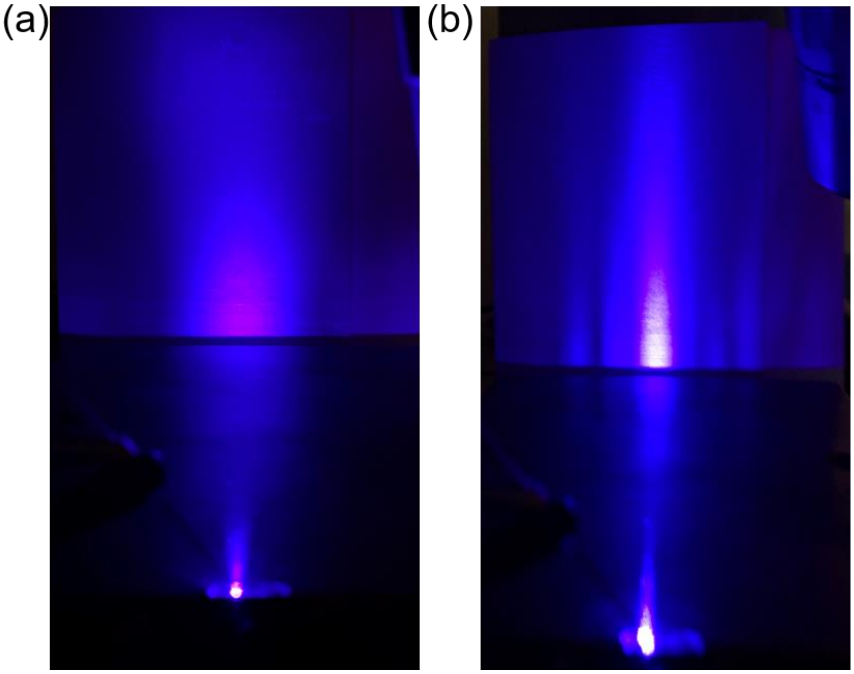

Figure 4-9 Far field patterns of a HSQ embedded DFB-LD with 3 um wide ridge (a) and 15 um wide ridge(b). For wider ridge lasers, the high order side modes can be clearly seen, while the pattern for narrow ridge exhibits a gaussian shape.

from the thinner p-GaN cladding layer, the product of the coupling coefficient and cavity length of the third-

order DFB-LD (~0.65, for a 1800 μm cavity) is still lower than the reference first-order one (~1.2). Such difference in κ due to grating order difference allows us to analyze the impact of *κL* on the performance of the lasers. As κ increases, the stopband of reflectance also widens, which often results in a worse mode suppression due to a flatter mirror loss curve[13] and can also account for the SMSR differences we observed in Fig. 4-10. On the other hand, the increased reflectance will in turn cause a decrease in the total mirror loss and the laser threshold, which explains the threshold current different. Other than indirect estimation of

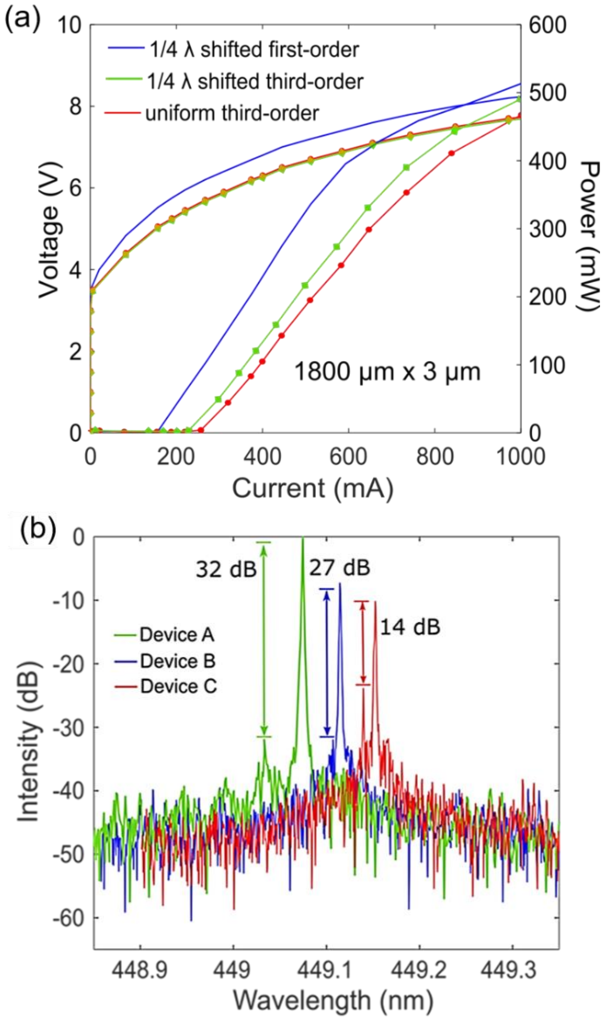

Figure 4-10 CW light–current–voltage characteristics (a) and spectra (b) of 3 μm by 1800 μm DFB-LDs with different grating orders and phase-shifted lengths.

the coupling coefficient from simulation, previous studies also show that other methods such as green function-based fitting of ASE spectrum could give a better insight. [22] Accurately characterizing the grating coefficient κ directly from the device, however, remains difficult.

For that reason, to further understand the effect of κ and phase shift on the spectrum and the threshold current variations, we compared the material gain of the different LDs as a function of the injected current, which can be readily obtained as the product of the injection efficiency and the threshold current density. When the material gain is plotted as a function of the injected current density, as in Fig. 4-7(b), the points can be fitted to the two parameter exponential curve through the approximation, $J = J_{tr} \exp(g_{th}/g_{oN})$ where J_{tr} is the transparency current density and g_{0N} is a material gain coefficient for the QWs, assuming the recombination at threshold is dominated by spontaneous recombination. Furthermore, the threshold modal gain can also be given as: $g_{th} = m/\Gamma\ (\alpha_i+\alpha_m)$ where m is the number of quantum wells, and Γ is the optical mode confinement (1.04 % per quantum well) and can be obtained from numerical mode solver simulation. Using this approach and the extracted values from Fig. 3(a), a material gain coefficient of around 2150 cm^{-1} per quantum well and J_{tr} of 0.57 kA/cm^2 was extracted for both first-order (black) and third order (red) LDs, which is comparable to what we previously observed in mirror loss difference due to the extra $\lambda/4$ shift can be extracted to be 0.4, which could be useful information to characterize the grating and coupling properties in future experiments. Based on such extracted threshold difference for phased-shifted grating, the κL for the third order grating can be calculated using the transmission spectrum method[13] to be ~0.55, which is very close to what we estimated using the refractive index difference method (0.65). Based on that, the coupling constant of the third-order grating therefore can be determined to be around 3.1 cm^{-1}.

C. Polished facets and Beam profile characterization

It has long been known that laser oscillators using stable resonators will typically oscillate in lowest and possibly higher-order Hermite-gaussian transverse modes due to it has the lowest energy; and it is also well recognized that the lowest-order or TEM_{00} mode from such a stable cavity provides an ideal beam profile both for analytical and for many practical purposes. When the ridge width is small, the diode lasers are limited in maximum power due to catastrophic optical damage at the output facets, yet the increase of the ridge with often is highly susceptible to free-carrier-induced self-focusing, which causes chaotic beam filamentation. This filamentation results in a massive degradation in beam quality that causes difficulties when trying to couple the beam into optical fiber or in any other applications that require low-loss coupling. Meanwhile, grating design, due to the introduction of refractive perturbation, often has an impact lateral confinement, ending up reshaping the mode profile. DFB-LDs, due to its applications, also find many uses that require fiber coupling. It is thus important to understand the beam quality of the DFB-LDs with surface gratings, etched or imbedded. One notorious fact about the lasers with etched facets is the vertical far field pattern as shown in Figure 4-9. Due to the limitation of the CAIBE etching tool, a "wing" will remain next to the etched facets after dry etching as illustrated in Figure 4-9. Such remaining parts will not only affect the laser performance, but seriously degrade the mode quality due to the interference caused by the beam reflection from the substrate. In the experiment, we first observed the far field patterns of the lasers rom both grating designs. Single transverse mode lasing was observed in all the 3 um laser diodes with surface grating as indicated by the far field patterns and high-resolution transverse scanning with a multi-mode fiber. To have a better understanding of the beam profile, far field pattern it not good enough since low-intensity side mode can theoretically exist. To verify the mode profile, the two-dimensional comprehensive beam quality factor (M^2) was measured. Since we do not have an accessible beam profiler, an 2D spatial scanning of the beam intensity using an optical mode fibre was experimented as shown in the Fig. 4-11. The scanning confirms the single lateral mode emission as observed from far field patterns. More specifically, transverse linear scanning of the beam mode also reveals a beam divergence half angle of 9.6° and beam quality (M^2) of 1.35.

Previous simulation shows that the loss can be very high when ridges are less than 2 um due to high sidewall loss from the surface recombination, [12] and can be considered as supporting single mode emission only. Interestingly, while almost all 15 um laser diodes

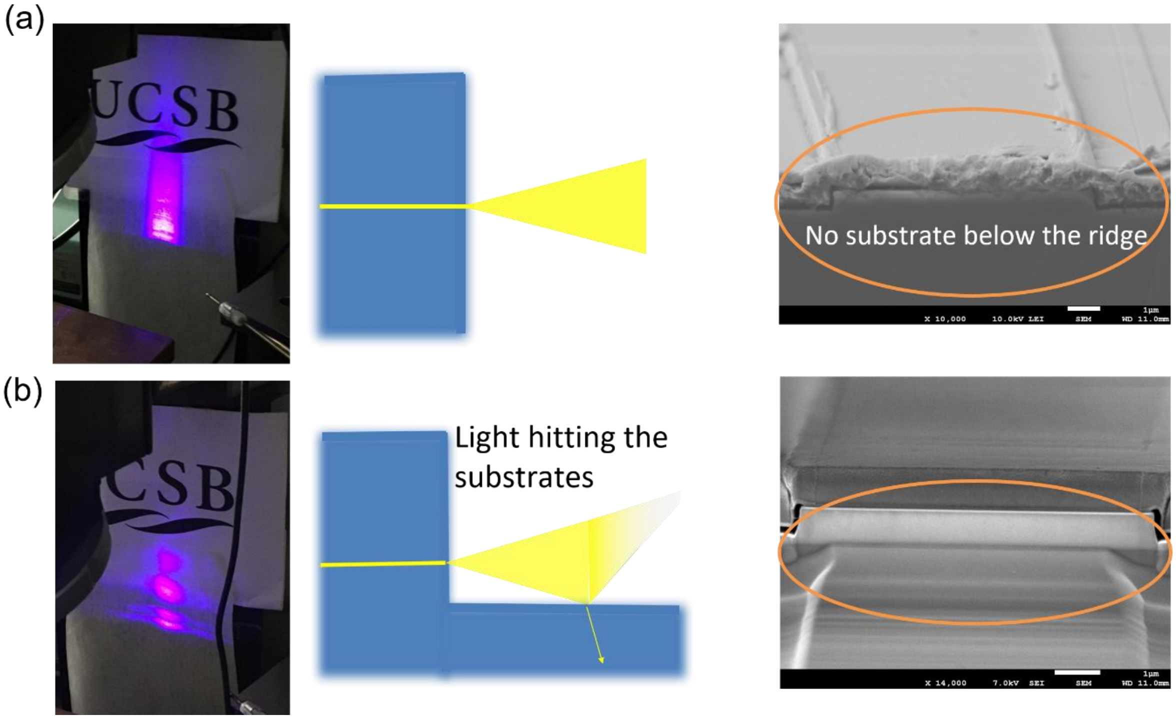

Figure 4-11 (a) the far field pattern from a polished laser diode with no substrate wing below the ridge and (b) from an etched facet laser diode where part of laser beam is reflected and causes interference.

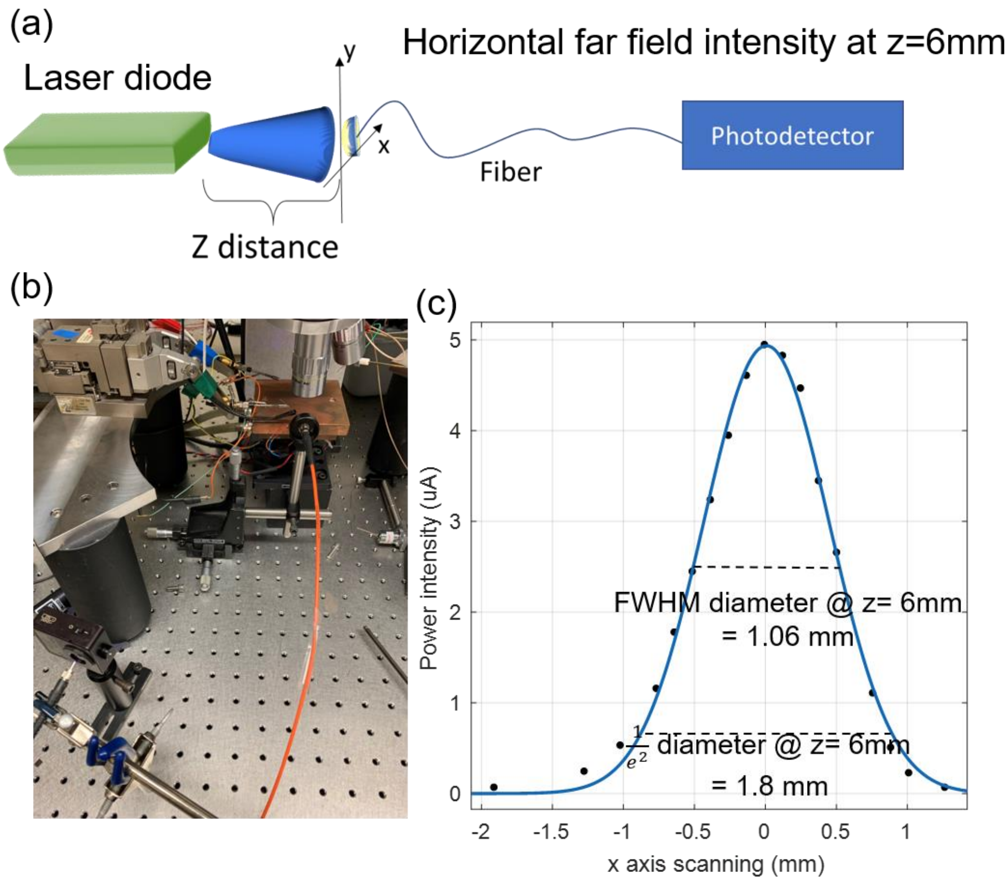

Figure 4-12 (a) the setup for characterization of laser beam profile and (b) a photo of a laser being tested diode (c) shows the far field horizontal light intensity at the distance of 6 mm to the laser facet.

exhibit multi-mode emission, the 8 um ones with etched grating stay in the single mode even at a high current. It is important to note that even though the 8 μm wide ridge supports multiple lateral modes, a single lateral mode was observed in the far field pattern, as shown in Fig. 5(d) when current density was no greater than 6.5 kA⁄cm^2. Such single lateral mode operation and strong suppression of the higher order modes can be attributed to the high optical loss near the metal contact along the edges of the ridge, as shown in Fig. 4-13. Simulations [Fig. 4-13] also confirm that the optical loss of the second order mode (24.9 cm^{-1}) is more than twice as large as the fundamental mode (11.5 cm^{-1}), thus the higher order modes were largely suppressed.

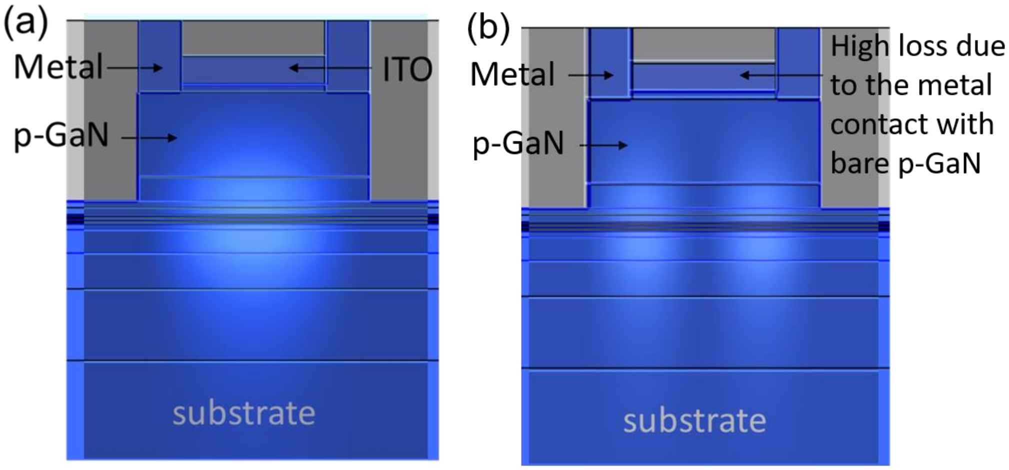

Figure 4-13 Cross-section (along the grating direction) view of the structure for simulating the fundamental, (a) and second order, (b) mode profiles simulated by Fimmwave. The second order modes are pushed to the sides of ridges and closer to the top metal contacts and thus suffer higher optical losses.

Another important issues to be addressed is the interference pattern caused by the substrate wing due to the nature of etched facets. Cleaving the unwanted area works on other III-V materials or even conventional c-plane GaN, yet often fails on GaN of semipolar orientation due to the absence of a clear cleavage plane. One possible solution to this is polishing away the wings after the laser is fabricated. As an alternative, mechanical polishing has also been shown to be a feasible process for fabricating mirror facets for semipolar LDs. [18] A dicing saw was first used to separate the laser bars and the facets were formed using mechanical polishing by an Allied High Tech MultiPrep tool on diamond lapping paper. [22] To make sure the verticality of the polishing process, the laser bar needs to be sandwiched between two clamping Si bars which were diced at the same time with the laser. Figure 4-14 describes the process of such polishing process. It is worth noting that when the wings are reduced to less than 15 um long, the interference induced stripe pattern start to transition to a circular shape as shown in Fig 4-14 (c-e).

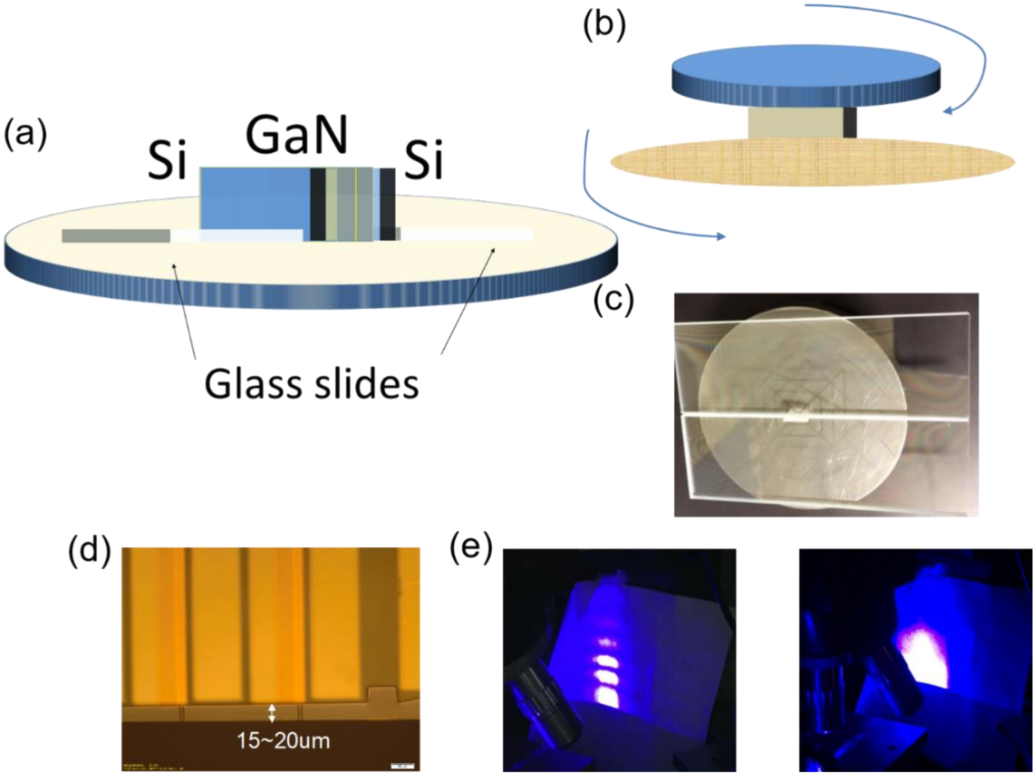

Figure 4-14 (a) the setup for characterization of laser beam profile and (b) a photo of a laser being tested diode (c) shows the far field horizontal light intensity at the distance of 6 mm to the laser facet.

Furthermore, such methods of removing the substrate wings can also be extended to polishing facets. [15,16] Compared to etched facets, polished facets in general have a smoother and more vertical profile. As shown in the Fig. 4-15, the entire GaN samples have also been polished and the facets are smooth. More specifically, during the polishing process, a diamond pad with 6 μm grit size was first used to grind the edge of the substrate (wing) up to less than 40 μm. Then the pad was replaced with a 3 μm grade pad to slowly polish the wings up to around 10 μm away from the facets. Metal smearing due to the

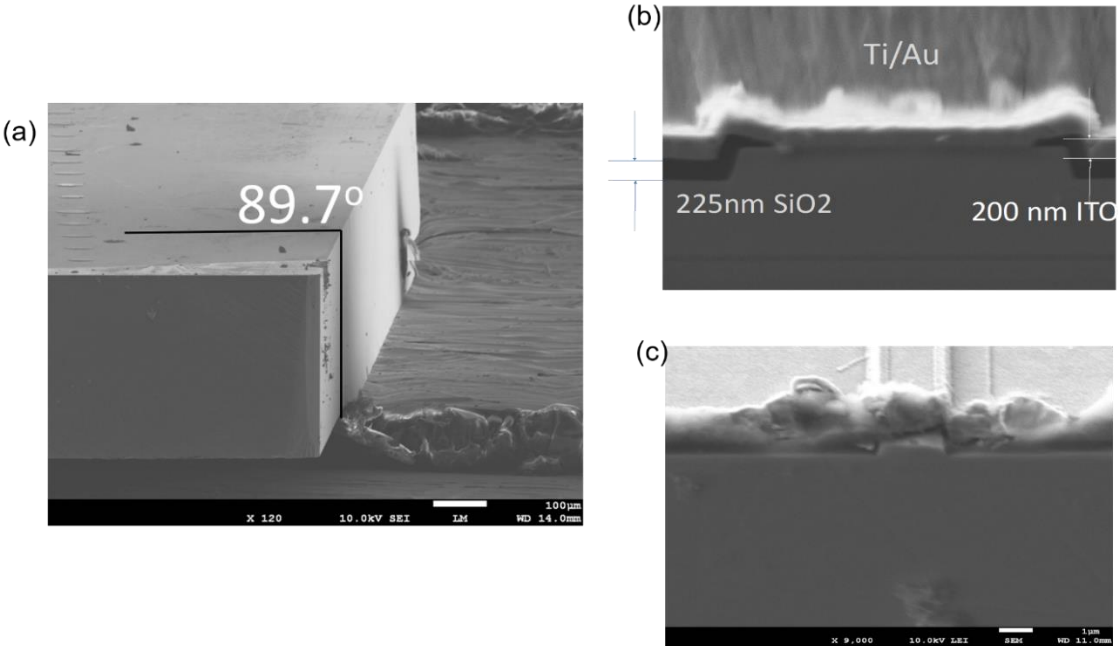

Figure 4-15 (a) SEM image of an entire polished substrate, the polishing angle is close to 90 deg (b) The cross-sectional SEM image of polished facet laser diode (c) shows the metal smearing caused by over-polishing

lapping process could happen and therefore it is important to stop the polishing right before the metal.

Similar polishing process was also applied to substrate thinning, where 6 µm and 3µm pads were also used first. Different from facet polishing, to keep the backside more smooth and reduce the possible cracks and damage layers caused by mechanical forces, another 1 µm diamond pad was used followed by 0.3 µm Al_2O_3 pad polishing. Then the backside was cleaned in BHF and dry etched in Cl_2 at least 10 µm to fully remove all the damaged layers before depositing the backside contact.

D. Spatial Hole Burning effect

High performance DFB-LDs with good single longitudinal mode (SLM) property and narrow linewidth are very important for high-speed optical communication systems. In the well-known phase-shifted DFB semiconductor lasers, when the injection current is high or the grating coupling coefficient is large, spatial hole burning (SHB) can affect their performance seriously. More specifically, a high κ has been generally associated with SHB especially in phase-shifted DFB-LDs.

The consideration of spatial hole burning is important because this nonlinearity has a strong effect on various performance aspects of DFB lasers. It has been found both experimentally [5] and theoretically [15] that lasers can become multimoded at low or moderate power levels due to strong spatial hole burning. Moreover, it can give rise to a less

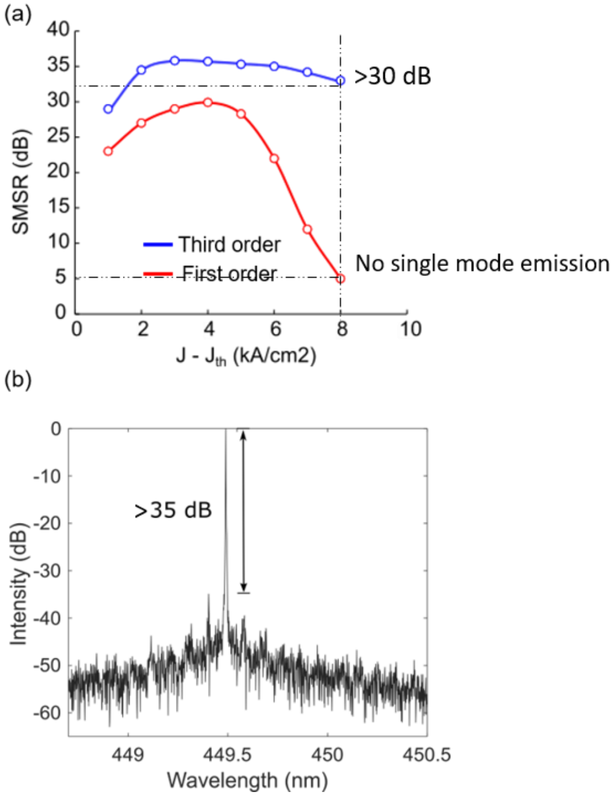

Figure 4-16 (a) the SMSRs of different grating order DFB-LDs as a function of current density minus threshold current density. (b) high-resolution CW spectrum of a phase-shifted third-order grating DFB-LD at a high current density flat FM response [16], an increased linewidth [17], and nonlinearities of the P-1 curve. The latter prop-erty is crucial in analog systems where low harmonic dis-tortion is desired [18]. This means that spatial hole burning corrected yield gives information of the percentage of lasers with, e.g., low harmonic distortions and not only of the SLM yield. As expected, the SMSR first slowly goes up as a result of current injection. As shown in Fig 4-16, for lasers with a first-order grating, the SMSR drops quickly at high current densities (> 7 kA/cm^2) while such degradation is less severe when a high-order grating is used possibly due to a much lower coupling constant.

References

[1]. J. Dai, X. Xie and X. Zhang, Physical Review Letters 97, (2006).

[2]. V. Ménoret, R. Geiger, G. Stern, N. Zahzam, B. Battelier, A. Bresson, A. Landragin and P. Bouyer, Optics Letters 36, 4128 (2011).

[3]. Y. Chi, D. Hsieh, C. Tsai, H. Chen, H. Kuo and G. Lin, Optics Express 23, 13051 (2015).

[4]. I. Ushijima, M. Takamoto, M. Das, T. Ohkubo and H. Katori, Nature Photonics 9, 185-189 (2015).

[5]. P. Hammond and R. Hughes, Nature Physical Science 231, 59-60 (1971).

[6]. W. Liang, V. Ilchenko, D. Eliyahu, A. Savchenkov, A. Matsko, D. Seidel and L. Maleki, Nature Communications 6, (2015).

[7]. C. Lin and C. Shank, Applied Physics Letters 26, 389-391 (1975).

[8]. L. Mahler, A. Tredicucci, F. Beltram, C. Walther, J. Faist, H. Beere, D. Ritchie and D. Wiersma, Nature Photonics 4, 165-169 (2010).

[9]. Z. Wang, B. Tian, M. Pantouvaki, W. Guo, P. Absil, J. Van Campenhout, C. Merckling and D. Van Thourhout, Nature Photonics 9, 837-842 (2015).

[10]. S. Masui, K. Tsukayama, T. Yanamoto, T. Kozaki, S. Nagahama and T. Mukai, Japanese Journal Of Applied Physics 45, L1223-L1225 (2006).

[11]. J. Kang, H. Wenzel, E. Freier, V. Hoffmann, O. Brox, J. Fricke, L. Sulmoni, M. Matalla, C. Stölmacker, M. Kneissl, M. Weyers and S. Einfeldt, Optics Letters 45, 935 (2020).

[12]. T. Slight, S. Stanczyk, S. Watson, A. Yadav, S. Grzanka, E. Rafailov, P. Perlin, S. Najda, M. Leszczyński, S. Gwyn and A. Kelly, Applied Physics Express 11, 112701 (2018).

[13]. L. Coldren, S. Corzine and M. Mašnović, Diode Lasers And Photonic Integrated Circuits (Wiley, Hoboken, N.J, 2012).

[14]. M. Okai, N. Chinone, H. Taira and T. Harada, IEEE Photonics Technology Letters 1, 200-201 (1989).

[15]. M. Okai, T. Tsuchiya, K. Uomi, N. Chinone and T. Harada, IEEE Journal Of Quantum Electronics 27, 1767-1772 (1991).

[16]. P. Zhou and G. Lee, Applied Physics Letters 58, 331-333 (1991).

[17]. W. Scheibenzuber, U. Schwarz, R. Veprek, B. Witzigmann and A. Hangleiter, Physical Review B 80, (2009).

[18]. S. Mehari, D. Cohen, D. Becerra, S. Nakamura and S. DenBaars, Optics Express 26, 1564 (2018).

[19]. A.J. Lowery, A. Keating, and Casper N. Murtonen, IEEE JOURNAL OF QUANTUM ELECTRONICS, 28, 9 (1992)

[20]. Lumerical Website, "https://support.lumerical.com/hc/en-us/articles/360047024294-DFB-laser-using-travelling-wave-laser-model-TWLM-"

[21]. T. Uusitalo, H. Virtanen and M. Dumitrescu, Optical and Quantum Electronics 49, (2017).

[22]. H. Wenzel," IEEE Journal of Selected Topics in Quantum Electronics 9, 865-871 (2003).

[23]. S. Mehari, D. Cohen, D. Becerra, S. Nakamura and S. DenBaars, Japanese Journal Of Applied Physics 58, 020902 (2019).

[24]. K. David, G. Morthier, P. Vankwikelberge, R. Baets, T. Wolf and B. Borchert, IEEE Journal Of Quantum Electronics 27, 1714-1723 (1991).

[25]. L. Ge, O. Malik and H. Türeci, Nature Photonics 8, 871-875 (2014).

V. Highly polarized light emitting diodes with surface gratings

A. Inspirations and simulations

Unlike the very recent advent of GaN laser diodes, InGaN light-emitting diodes (LEDs) have been widely used for a long time in applications such as display technologies, automotive lighting systems and general illuminations. [1-3] Specifically, polarized light sources are very useful since it can significantly improve the efficiency of these applications by offering an improved contrast due to a reduced glare, and a high-energy efficiency display that operates through the spatial modulation of polarized light. [4,5] However, common light sources are usually unpolarized since the electric field of the light emitted has no preferred orientation. Polarized white light has been traditionally implemented based on some low-efficiency approaches that requires external optical components or fluorescent films, resulting in a significant optical power loss due to the absorption or reflection effects. [6,7] Therefore, it has been of great interest to realize monolithic polarized emission light sources.

Several methods have been proposed to increase the polarization ratio (PR) of the emission light. Growing LEDs on semipolar or nonpolar orientations is a straightforward way to enhance the polarization due to the separation of the top two valence bands caused by the anisotropic strain. [8-12] The light emitting from nonpolar GaN-based LEDs can be fully polarized, but the indium incorporation efficiency in nonpolar GaN orientation is very low, and thus the application is limited. [12] Moreover, switching to semipolar orientated QWs has shown to exhibit a higher indium incorporation efficiency followed by an enhanced PR ranging from 0.25 to 0.4. [12-15] A higher PR remains highly desired for high-efficiency display applications.

Surface plasmons (SPs) can potentially enhance both the quantum efficiency and polarization properties of nitride LEDs. [16-20] By using nano-scale metallic patterns, the SPs will provide strong enhancement in light emission and extraction when the extinction band of the SPs is close to the bandgap emission energy. By utilizing grating enhanced SPs with InGaN/GaN multiple quantum wells (MQWs), the light can be coupled into intrinsic polarized SPs modes, resulting in the generation of polarized light. Zhang et al. reported a high polarization degree of 54% from InGaN green MQWs using SPs. [16] However, only photoluminescence (PL) emission of the polarized light so far has been demonstrated, [16] and the electroluminescence (EL) has yet been realized due to the complications caused by direct etching into GaN during the formation of grating patterns. Shen et al. presented an enhanced polarized light output of InGaN LEDs using metal grating SPs through forming p-GaN grooves and using Ag. Nevertheless, Ag is form a reliable ohmic contact to p-GaN and direct etching into p-GaN leads to damages in the p-GaN and MQWs, resulting in a degradation of the EL performance. [20] To the best of authors' knowledge, there is still no reports about the two or more than two different colors of SPs coupling for GaN-based LEDs. In this Chapter, we are going to demonstrate a viable approach to realize highly polarized electrically driven monolithic white semipolar micro-LEDs (µLEDs) based on dual-color surface plasmons (DSPs) by combining an indium tin oxide (ITO) grating with Al coated SPs and dual-color quantum wells. Compared to the previous works, this proposed DSPs design exhibits several unique advantages: (1) ITO grating technology exhibits very good ohmic contact and high transparency without introducing any damage to p-GaN or MQWs, [21] which allows the excellent electrical operation; (2) Theoretical simulation reveals that DSPs can be realized, which will widely broaden the SPs coupling wavelength; (3) We experimentally demonstrated single chip white semipolar µLEDs with a significant enhancement of the PR enabled by DSPs by grown on low-cost and scalable semipolar/sapphire template. Moreover, the fabricated monolithic white µLEDs was employed in a visible-light communication (VLC) system, which is very important application of III-nitride semipolar µLEDs that shows a fast decay time and a high modulation speed.

Electromagnetic fields at the metal dielectric interface can be enhanced by the collective excitation of free electrons at metal surfaces. The interactions between the photons and the coherent oscillation of free electrons on a metal surface formed surface plasmon polaritons (SPPs). The resonance occurs when the difference in momentums between the SPPs and the parallel component of the incident wave vector can be balanced by the lattice vector of periodic corrugation on the metal surface. Compared to the waves perpendicular to the grating direction, the propagation of the waves along the grating direction is not significantly affected by the SPs as a result of the forbidden boundary conditions at the interface and penetration of the SPs fringing field into the semiconductor. Such difference in the propagation leads to a strong deviation between transverse electric (TE) and transverse magnetic (TM) light and thus a high polarization ratio. For SPPs propagating along the GaN/Al interface, the coupling depth can be expressed as

$$z = \frac{\lambda}{2\pi}[(\varepsilon'_{GaN} - \varepsilon'_{metal})/\varepsilon'^{2}_{metal}]^{1/2} \text{ (5-1)}$$

where ε'_{GaN}, ε'_{metal} and λ represent the real parts of the dielectric constants of the semiconductor and metal, and the SPP wavelength, respectively. [20] Therefore, by carefully optimizing the z (positions of the QWs with different emission wavelength) and λ, broadband dual-color SPs coupling can be realized. It can also be expected that the geometry of the narrow groove plasmonic nano-gratings has a substantial effect on which wavelength the dip in the plasmon resonance occurs.

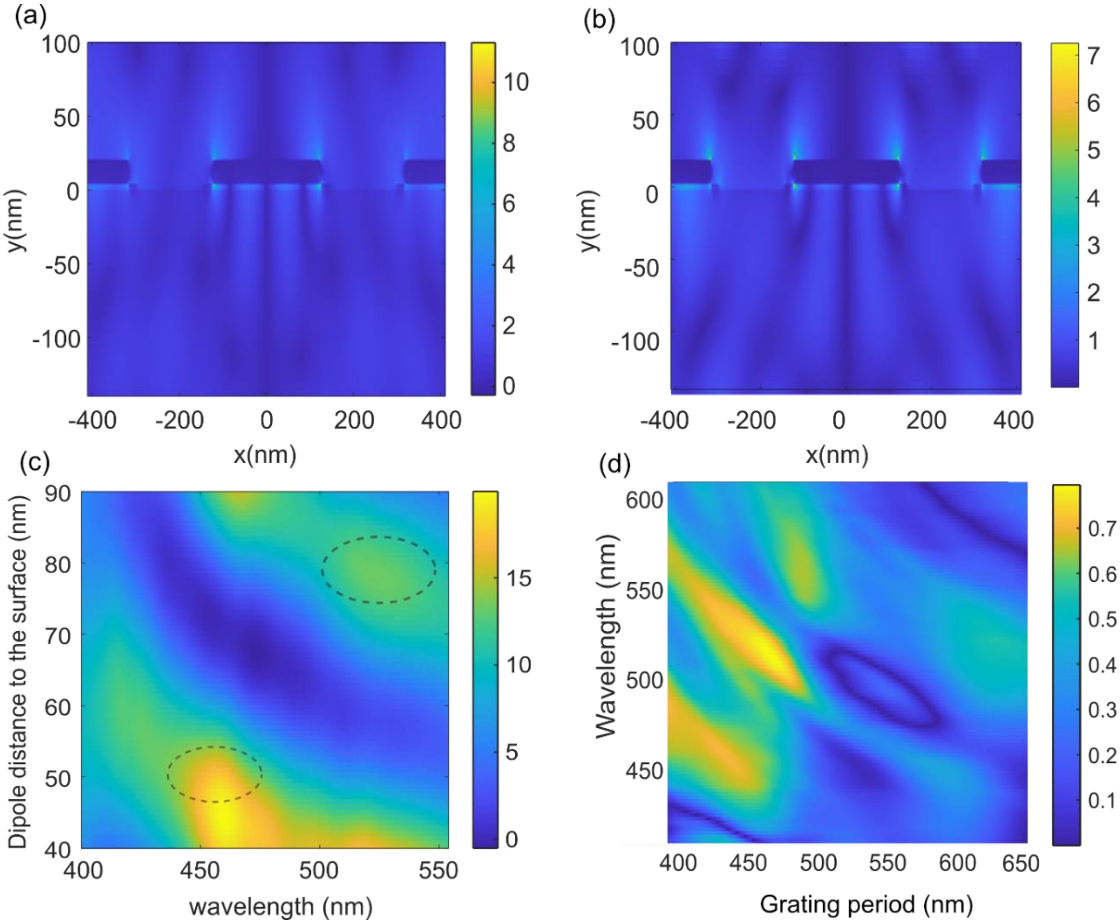

Figure 5-1 Electric field distribution of the width for grating period of 440 nm at dipole emission wavelength of (a) λ = 450 nm and (b) λ= 530 nm; (c) Dipole's Purcell factor dependence of emission wavelength and quantum well location. Black circles imply the location and targeted wavelength of the design; (d) Simulated polarization ratio as a function of the ITO grating period and the emission wavelength.

To quantitatively understand the dual-color surface plasmon coupling with ITO gratings, Lumerical Solution [19] software is used to simulate the SPs properties of the Al-covered ITO gratings, through implementing finite-difference time-domain (FDTD) algorithm by numerically solving Maxwell's equations. The 3D simulation set-up is shown in

Fig. 1(a). The perfect matched layers (PML) approach is used at the top and bottom to provide absorption boundary conditions. The dimension of the simulation region is set to be 8 times the grating period in x direction, and 2 μm and 1 μm in y and z directions, respectively, where the grating period *p* is varied from 400 to 500 nm in the simulation. The far field monitor at the top is located 300 nm above the grating structure. To simulate the polarization effect, we assume the dipoles are oriented in plane, where ϕ and φ are equal to 0° approximately and the θ is dependent on polarization degree of the emitted light due to the semipolar nature of the substrate. (Fig. 1(a)). The spontaneous emission is represented by radiations from two dipole sources with distinct wavelengths (450 nm and 530 nm) located at the center of the two QWs, respectively. The dielectric function of InGaN, GaN, ITO and aluminum used through the simulation can be found from Ref. [22] and [23]. Simulation shows that the intensity of electric field at the emission wavelengths (Fig. 1(b) and 1(c)) has a strong enhancement near the metal/semiconductor interface, while the field decays evanescently as the distance from the interface increases. The elliptical shapes are typical of the excited SPs modes at the interface of Al/GaN, which leads to the high transmittance for the TM electric field. It is also clear that at shorter wavelengths the SP modes are less confined and have higher local intensity, indicating the SPs coupling with blue emission is stronger and more efficient. Based on Fig.1(b) and (c), both blue and green MQWs must be within 100 nm from the surface to achieve a decent polariton coupling. Next, to maximize the SPs coupling for each MQW, the optimal distances of the dual-color MQWs (d_1, d_2) to the grating surface (Fig. 1(a)) need to be simulated. Because such distinct localization of optical energy densities extends into the active region, the radiative recombination rate of the MQWs can be enhanced due to the Purcell effect. [19] In our simulation with grating structure, the Purcell factor as a function of distance to the surface and wavelength is plotted in Fig. 1(d). Due to the limitation of MQW growths and the current spreading of p-GaN, the QWs cannot be too close to the surface grating, and thus to maximize the Purcell factor and coupling between SPs modes and the MQW areas, the distances to the surface (d_1, d_2) were chosen 55 nm and 75 nm for blue and green MQWs, respectively. Finally, the polarization ratio was calculated as the ratio of the transmittance of TE to the TM waves and plotted in Fig. 1(e). When the grating period is between 400 to 500 nm, high polarization ratio of TE to TM can be achieved at two distinct wavelengths simultaneously.

B. Device fabrication and performance

Guided by such simulation results, the semipolar monolithic white micro-LEDs devices were fabricated on top of chemo-mechanical polished high material quality 4-inch semipolar (20-21) GaN/sapphire templates provided by Saphlux Inc. grown by metal-organic chemical vapor deposition (MOCVD). Details of the template growth and characterization can be found in the literatures. [24-26] Trimethylgallium (TMGa), triethylgallium (TEGa), trimethylindium (TMIn), Trimethylaluminum (TMAl), ammonia (NH_3), disilane (Si_2H_6), and bicyclopentadienyl (Cp_2Mg) sources were used as precursors and dopants. The epitaxial structure was consisted of a 1.5-μm Si-doped n-type GaN (3×10^{18} cm^{-3}), 30 pairs $In_{0.06}Ga_{0.94}N$/GaN (2-nm/2-nm) superlattices, a 3-nm $In_{0.25}Ga_{0.75}N$ QW, a 10-nm GaN barrier, a 3-nm $In_{0.14}Ga_{0.86}N$ blue QW, a 10-nm GaN spacer, a 15-nm p-type AlGaN electron blocking layer, and p-type GaN/p+GaN (50-nm/5-nm) with a Mg concentration of 4×10^{19} and 2×10^{20} cm^{-3}, respectively.

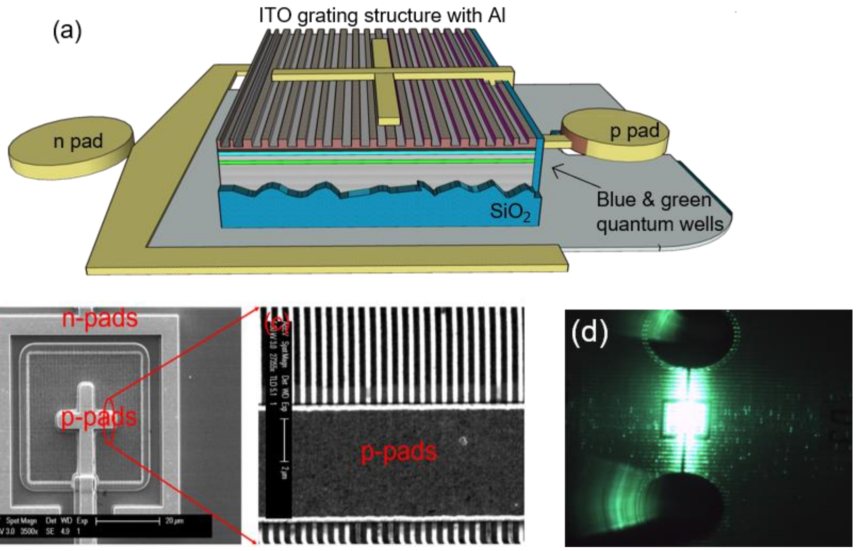

Figure 5-2 (a) SEM images of the fabricated ITO grating enhanced DSPs µLEDs with a size of 40×40 µm2; (b) Enlarged SEM image of grating ITO; (d) EL image of the ITO grating enhanced DSPs µLEDs at 1 mA.

Firstly, 150 nm ITO was deposited using electron-beam evaporation. Gratings of ITO with a period varied from 250 to 450 nm were formed using electron-beam lithography. A 10-nm thin Al metal was deposited on top of the grating ITO. Silicon tetrachloride ($SiCl_4$) was then used to etch the n-GaN layer in a reactive-ion etching chamber. An omnidirectional reflector (ODR) consisting of SiO_2 and tantalum pentoxide stacks with an aluminum oxide cap layer was deposited using ion beam deposition and 25-nm SiO_2 was deposited on the LEDs sidewalls for passivation by atomic-layer. Finally, metal contact consisting of Al/Ni/Au (500/100/500 nm) was evaporated for n-GaN ohmic contacts and n/p-pads. Fig. 3(a) is the scanning electron microscopy (SEM) image fabricated 40×40 μm^2 ITO grating enhanced DSPs µLED. The enlarged ITO grating pattern is shown in the SEM image of Fig. 3(b). The ITO grating period is measured to be ~400 nm, which also shows a very good uniformity. In this experiment, the grating period was varied from 360 nm to 590 nm, to investigate the effect of the grating period on the properties of the polarization of the devices. Fig. 3(c) demonstrates the morphology of the Al-coated layer by SEM, which shows an Al nanoparticle with a size of around 25 nm. Moreover, Fig. 3(d) presents the electrically luminous image of the 40×40 μm^2 µLED at an injection current of 1 mA under CW operation, exhibiting a very uniform white emission. Consequently, for the first time, such DSPs design by combining ITO grating and Al coating enables the electrical operation of the LEDs, indicating a promising and viable approach as compared to the previous reported Al or Ag SPs/grating designs. [16, 20]The optical polarization ratio is obtained by $\rho = (I_{x'} - I_{y'})/(I_{x'} + I_{y'})$, where $I_{x'}$ and $I_{y'}$ are the maximum and minimum integrated intensities of the emission spectra when we align the polarizer along the x'-direction and y'-direction, respectively. The x'- and y'-directions for (20-21) µLED is along [1-210] and [10-1-4], respectively.[13] Fig. 4(a)

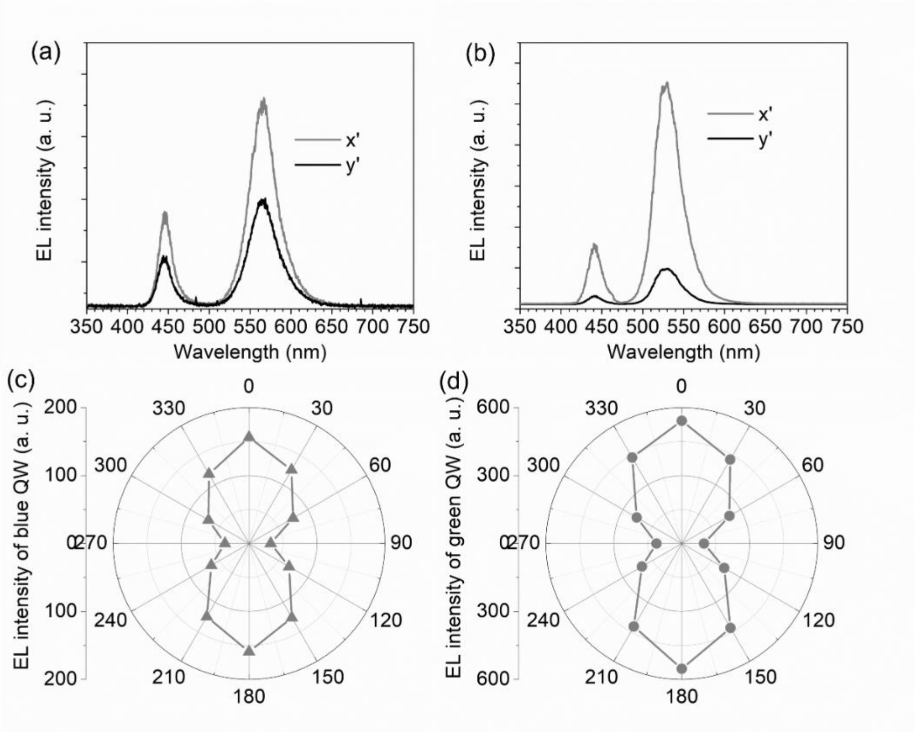

Figure 5-3 EL spectra along x^'-direction and y^'-direction for (a) reference µLEDs and (b) ITO grating enhanced DSPs µLEDs; EL intensities as a function of polarization angle for (c) blue emission and (d) green emission.

shows the EL emission spectra along x'- and y'-directions for reference μLEDs without grating enhanced SPs. The PR for the blue and green QWs was calculated to be 0.24 and 0.28, respectively, followed by an average PR of 0.26.[24] Those PR values agree well with the previous report. [12, 13] It is worth noting that the EL spectrum along the x'-direction of the ITO grating enhanced DSPs μLEDs is much stronger than that along the y'-direction in Fig. 4(b), suggesting a strong polarization enhancement as a result of the grating. The PR of the blue and green peaks is significantly increased to 0.71 and 0.68, respectively. The average PR is calculated to be 0.70, which is enhanced by 1.7-folds as compared to the reference LEDs. Such high PR in the monolithic white LEDs would be undoubtedly beneficial for reducing the energy loss in LCDs application. Detailed EL intensity as a function of rotation angle from 0 to 360 degree with a step of 30 degrees for the blue and green peaks were also demonstrated in Figs. 4(c) and 4(d), respectively. When the angle of the polarizer was rotated from 0 to 2π, maximum and minimum of EL intensities are obtained, corresponding to the relative magnitude of TE- and TM-polarized emission, respectively. A period of 180 degree was obtained for TE and TM polarized emission intensity showing a symmetric characteristic.

The optical polarization ratio is obtained by $\rho = (I_{x'} - I_{y'})/(I_{x'} + I_{y'})$, where $I_{x'}$ and $I_{y'}$ are the maximum and minimum integrated intensities of the emission spectra when we align the polarizer along the x'-direction and y'-direction, respectively. The x'- and y'-directions for (20-21) μLED is along [1-210] and [10-1-4], respectively.[13] Fig. 4(a) shows the EL emission spectra along x'- and y'-directions for reference μLEDs without grating enhanced SPs. The PR for the blue and green QWs was calculated to be 0.24 and 0.28, respectively, followed by an average PR of 0.26.[24] Those PR values agree well with the previous report. [12, 13] It is worth noting that the EL spectrum along the x'-direction of the

ITO grating enhanced DSPs μLEDs is much stronger than that along the y'-direction in Fig. 4(b), suggesting a strong polarization enhancement as a result of the grating. The PR of the blue and green peaks is significantly increased to 0.71 and 0.68, respectively. The average PR is calculated to be 0.70, which is enhanced by 1.7-folds as compared to the reference LEDs. Such high PR in the monolithic white LEDs would be undoubtedly beneficial for reducing the energy loss in LCDs application. Detailed EL intensity as a function of rotation angle from 0 to 360 degree with a step of 30 degrees for the blue and green peaks were also demonstrated in Figs. 4(c) and 4(d), respectively. When the angle of the polarizer was rotated from 0 to 2π, maximum and minimum of EL intensities are obtained, corresponding to the relative magnitude of TE- and TM-polarized emission, respectively. A period of 180 degree was obtained for TE and TM polarized emission intensity showing a symmetric characteristic.

In order to verify the polarization dependence on the applied current and period width, the PR of the blue peak (blue curve) and green peak (green curve) versus the ITO grating periods varied from 250 to 480 nm was plotted in Fig. 5(a). As the current increases, the emission spectrum shifts and leads to a lower polarization ratio for both wavelengths. Such shifts are, however, partly balanced by the change of refractive index of ITO caused by increased carrier density, which leads to a flattening trend as at high current densities. One can see a few SPs resonance features in each curve with the increasing wavelength with an increasing period as shown in Fig. 5(b). We see that the PR of blue and green QWs shows approximately the similar trends a function of grating period. At a period of around 420 nm, both the green and blue polarization ratios reach the peak while the maximum of green QW (68%) is slightly lower than the blue QW (71%) possibly due to the farther QWs and a weaker coupling. Overall, experimental data has shown good agreement with the FDTD numerical simulation results, indicating that by precisely controlling the emission wavelength of the QWs and the period of the grating, light of both wavelengths can be highly polarized simultaneously. Angular measurement of the intensity distribution from the emission of such grating µLED has also been conducted. Fig. 5(c) shows that the light emission cone is confined to the 40 degree region. Moreover, Fig. 5(d) shows the output power-current-voltage (L-I-V) characteristics for the reference µLED and DSPs µLED with a size of 40×40 μm^2. Both samples show good p-n junction properties, and the light output power lineally increases with the injection current. It is worth pointing out that the output power of the DSPs µLED was increased to 0.041 mW from the 0.023 mW of the reference µLED, which is enhanced by 78%. Such enhanced output power can be explained by the DSPs coupling with the InGaN QWs, which increases the radiative recombination efficiency. When the SPs couples with the InGaN QWs, the exciton energy in the QWs will be transferred into SPs at the metal surface if the emission energy matches the energy of SPs, resulting in a large density of states with a fast coupling rate as well as a higher electron-hole radiative recombination. [20, 25, 26] Also, the forward voltage is raised from 4.3 to 5.6 V at 0.3 mA (20 A/cm^2) for DSPs µLED, which can be possibly resulted from the reduced current injection and worse current spreading due to the grooved ITO layer. Optimizing the ITO grating design would be our future work to further reduce the voltage penalty.

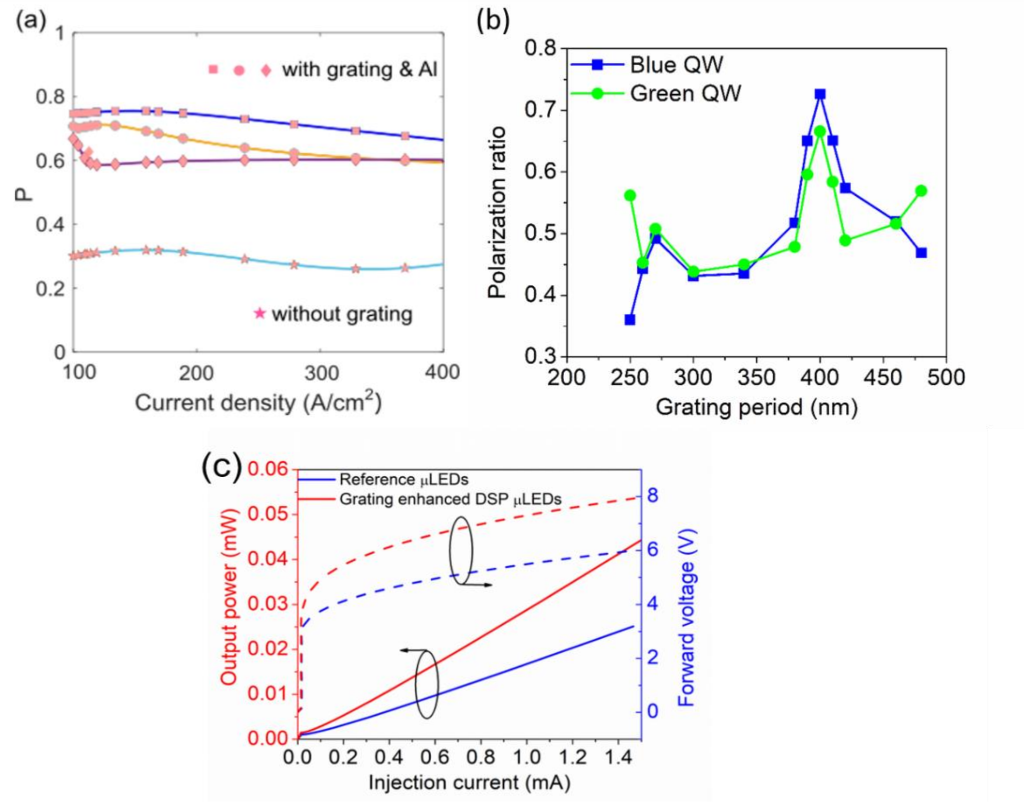

Figure 5-4 Polarization degree of the ITO grating enhanced DSPs semipolar μLED (hexagonal, square and circular markers represent λ = 450 nm, 530 nm and the average of the two, respectively) and the reference semipolar μLED at different current densities; (b) Measured calculated polarization ratio of the blue and green emission as a function of ITO grating periods. (c) Comparison of L-J-V characteristics between reference μLED and ITO grating enhanced DSPs μLED.

C. High speed characterization

The frequency response is essential for evaluating the high-speed operation performance. In this section, the measurement of modulation bandwidth of those μLEDs in the VLC system was carried. A Microwave Network Analyzer was used to measure the frequency response of μLEDs through a high-speed RF microprobe. RF signals generated by the network analyzer was directly modulated on top of a DC bias baseline using a bias tee. The signal of the LEDs was transmitted to a high-speed silicon (UPD-200-UP) photodiode with 2GHz bandwidth and then amplified by an amplifier (SHF 88 A) and fed back to the network analyzer. Before collecting the real data, the response of the photo detector (PD) and the amplifiers were first calibrated by a 450 nm high-power laser to measure the frequency response of µLEDs accurately. The magnitude of the measured frequency response was then normalized by dividing the output amplitude obtained at the PD by the reference noise level at the PD in the frequency domain. The measured maximum -3dB bandwidth is 620 MHz at an injection current density of ~1.4 kA/cm^2. The modulation bandwidth (*f*) at -3dB can be expressed by

$$f = \frac{\sqrt{3}}{2\pi}\left(\frac{1}{\tau_r} + \frac{1}{\tau_{nr}} + \frac{1}{\tau_{RC}}\right) \text{ (5-2)}$$

where τ_r, τ_{nr} and τ_{RC} is radiative recombination lifetime, nonradiative recombination lifetime and RC constant time. τ_r equals to $\frac{\sqrt{B}}{N}$, where *B* and *N* is the radiative recombination coefficient and the carrier density, respectively. *N* can be obtained by $\frac{J}{qd}$, where *J*, *q* and *d* is current density, elementary charge, and thickness of QWs, respectively. Since the radiatve recombination plays the dominant role, *f* can be given as:

$$f = \frac{\sqrt{3}}{2\pi}\left(\sqrt{\frac{BJ}{qd}} + \frac{1}{\tau_{RC}}\right) \text{ (5-3)}$$

From Fig. 5(b), the 3 dB bandwidth firstly increases linearly with the injection current density and then saturates.[27] This can be well explained from Eq. (3): under low-level current injection, the 3dB bandwidth is almost linearly increasing with *J*, indicating that the bandwidth is mainly dependent by the carrier lifetime instead of RC delay; at a very high injection current density, τ_{RC} plays the dominant role, resulting in the saturation of modulation bandwidth. A size dependent modulation bandwidth was also observed in Fig. 5-5 by comparing the results from 100×100 µm^2 to 40×40 µm^2 devices. As the size decreases, τ_{RC} decreases, leading to a higher modulation bandwidth.[28] It is worth noting that such a 620 MHz 3dB bandwidth can theoretically reaches near 1.24 Gbit/s under non-return-to-zero on-off keying modulation scheme, and can even achiever higher rate under more complicated modulation methods.[29] Since the carriers' radiative recombination occurs in both blue and green QWs, the modulation bandwidth is reduced due to a thicker *d*. Thus, a higher modulation bandwidth is expected using single QW structure. We note that the advantage of such QWs design is that it can overcome the slow frequency response of the yellow phosphor since the white light is required for the common VLC system, although the modulation bandwidth speed is sacrificed.

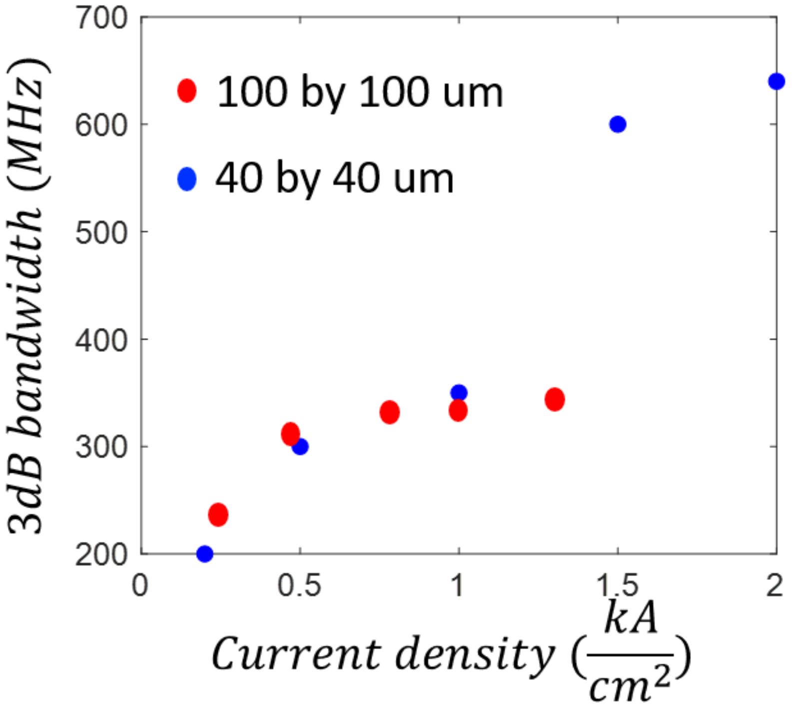

Figure 5-5 3 dB modulation bandwidth vs current deisnty of different sizes of the µLED.

References:

[1]. S. Nakamura, Science, 28, 956, 1998.

[2]. E. F. Schubert, J. K. Kim, Science, 308, 1274, 2005.

[3]. Y. Narukawa, M. Ichikawa, D. Sanga, M. Sano, T. Mukai, J. Phys. D: Appl. Phys., 43, 354002, 2010.

[4]. P. Yeh and C. Gu, Optics of Liquid Crystal Displays (Wiley, New York, 2010).

[5]. E. Matioli, S. Brinkley, K. M. Kelchner, Y. L. Hu, S. Nakamura, S. P. DenBaars, J. S. Speck, C. Weisbuch, Light: Science & Applications, 8, e22, 2012.

[6]. M. C. Chou, C. Y. Lin, B. L. Lin, C. H. Wang, S. H. Chang, W. C. Lai, K. Y. Lai, and Y. C. Chang, ACS Nano, 12, 8748, 2018.

[7]. N. F. Gardner, J. C. Kim, J. J. Wierer, Y. C. Shen, and M. R. Krames, Appl. Phys. Lett., 86, 111101, 2005.

[8]. H. Li, M. S. Wong, M. Khoury, B. Bonef, H. Zhang, Y. C. Chow, P. Li, J. Kearns, A. A. Taylor, P. De Mierry, Z. Hassan, J. S. Speck, S. Nakamura, S. P. DenBaars, Opt. Express, 27, 24154, 2019.

[9]. H. Masui, A. Chakraborty, B. A. Haskell, U. K. Mishra, J. S. Speck, S. Nakamura, and S. P. DenBaars, Jpn. J. Appl. Phys., 44, L1329, 2005.

[10]. Y. Zhao, S. Tanaka, Q. Yan, C.-Y. Huang, R. B. Chung, C.-C. Pan, K. Fujito, D. Feezell, C. G. Van de Walle, J. S. Speck, S. P. DenBaars, and S. Nakamura, Appl. Phys. Lett., 99, 051109, 2011.

[11]. H. Masui, H. Yamada, K. Iso, S. Nakamura and S. P. DenBaars, J. Phys. D: Appl. Phys. 41, 225104, 2008.

[12]. Y. Zhao, Q. Yan, C.-Y. Huang, S.-C. Huang, P. S. Hsu, S. Tanaka, C.-C. Pan, Y. Kawaguchi, K. Fujito, C. G. Van de Walle, J. S. Speck, S. P. DenBaars, S. Nakamura, and D. Feezell, Appl. Phys. Lett. , 100, 201108, 2012.

[13]. S.J. Kowsz, E.C. Young, B.P. Yonkee, C.D. Pynn, R.M. Farrell, J.S. Speck, S.P. DenBaars, and S. Nakamura, Opt. Express, 25, 3841, 2017.

[14]. H. Li, P. Li, H. Zhang, Y. C. Chow, M. S. Wong, S. Pinna, J. Klamkin, J. S. Speck, S. Nakamura, and S. P. DenBaars, Opt. Express, 28, 13569, 2020.

[15]. H. Li, M. Khoury, B. Bonef, A. I. Alhassan, A. J. Mughal, E. Azimah, M. E. A. Samsudin, P. De Mierry, S. Nakamura, J. S. Speck, S. P. DenBaars, ACS Appl. Mater. Interfaces, 9, 36417, 2017.

[16]. G. Zhang, X. Guo, F.-F. Ren, Y. Li, B. Liu, J. Ye, H. Ge, Z. Xie, R. Zhang, H. H. Tan, and C. Jagadish, ACS Photonics, 3, 1912, 2016.

[17]. M. Ma, D. S. Meyaard, Q. Shan, J. Cho, E. F. Schubert, G. B. Kim, M.-H. Kim, and C. Sone, Appl. Phys. Lett., 101, 061103, 2012.

[18]. M. C. Chou, C. Y. Lin, B. L. Lin, C. H. Wang, S. H. Chang, W. C. Lai, K. Y. Lai, and Y. C. Chang, ACS Nano, 12, 8748, 2018.

[19]. Chen, H., Fu, H., Lu, Z., Huang, X., And Zhao, Y. Optics Express, 24, 856, 2016.

[20]. K.C. Shen, C.-Y. Chen, H.-L. Chen, F.C. Huang, Y.-W. Kiang, C. C. Yang, and Y.-J. Yang, Appl. Phys. Lett., 93, 231111, 2008.

[21]. H. Zhang, D. A. Cohen, P. Chan, M. S. Wong, S. Mehari, D. L. Becerra, S. Nakamura, and S. P. DenBaars, Opt. Lett., 44, 3106, 2019.

[22]. K. Okamoto, I. Niki, A. Shvartser, Y. Narukawa, T. Mukai, and A. Scherer, Nature Materials, 3, 601, 2004.

[23]. R. J. Moerland and J. P. Hoogenboom, Optica, 3, 112, 2016.

[24]. M. Khoury, H. Li, P. Li, Y. C. Chow, B. Bonef, H. Zhang, M. S Wong, S. Pinna, J. Song, J. Choi, J. S Speck, S. Nakamura, and S. P DenBaars, Nano Energy, 67, 104236, 2019.

[25]. B. Leung, D. Wang, Y.-S. Kuo, K. Xiong, J. Song, D. Chen, S. H. Park, S. Y. Hong, J. W. Choi, J. Han, Appl. Phys. Lett., 104, 262105, 2014.

[26]. J. Song, J. Choi, C. Zhang, Z. Deng, Y. Xie, J. Han, ACS Appl. Mater. Interfaces, 11, 33140, 2019.

[27]. M.S. Islim, R.X. Ferreira, X. He, E. Videv Xie, S. Viola, S. Watson, S. Bamiedakis, N. Penty, R.V. White and I.H. Kelly, Photonics Res., 5, A43, 2017

[28]. J. McKendry, D. Tsonev, R. Ferreira, S. Videv, A. Griffiths, S. Watson, E. Gu, A. Kelly, H. Haas, and M. Dawson, in IEEE Summer Topicals Meeting Series (SUM), 2015

[29]. M. S. Islim and H. Haas, ZTE Commun. 14, 29–40, 2016

Appendix

A. Process flow for 1st generation DFB-LDs with an etched grating

Step	Equipment	#	Process Step	Notes
Surface Clean and Reactivation				
Remove Indium	Acid Bench	1	1:3 HNO_3:HCl (aqua regia) hotplate at 225 °C, 5-10' repeat 2x	Mix HCl & HNO_3, bring to boil, then add sample
Clean	Solvent bench	2	(Optional) Scrub samples in tergitol with swabs to get rid of any residual scum	
	Solvent bench	3	3' Ace, 3' Iso, 2' DI (sonicate on high) N2 dry	
Reactivate	RTA	4	Reactivate 15' at 600 °C N2/O2 (or use MOCVD lab furnace 600C 15 min N2/O2)	
P-Contact Formation ITO (Skip if using Pd/Au, Must use ITO if p-GaN is less than ~650 nm)				
ITO Deposition	Solvent bench	5	1min Ace, 1min Iso, 1min DI, N2 dry	
		6	Dehydration bake on hotplate at ≥110 °C for ≥2', cool 1'	
	UV Ozone	7	1200 s (~6 Å/min)	
	Acid Bench	8	Etch sample in HCL 15 mins	Removes Oxide, Do immediatley prior to ITO dep
	E Beam #2 (with heater) ~4-5hrs	9	Deposit 180 nm ITO with Si monitor Temp using 2-step temperature techqniue, first deposit 12 nm ITO at 50C and then immediately increase the temperatute to depostion 330C max (current heater set to **800C**) O2 flow: starting from~30sccm and ramp up to 45 sccm Tooling: **69.9-76** for accurate dep rate Keep the dep rate less than 0.3 A/s	Si Monitor #2
	Ellipsometer & AFM	10	Measure Si Monitor #2 thickness (Using model ITO-new) and make sure the RMS of the surface less than 1nm	Thickness:
Ridge Formation and SiO2 Deposition				

Gratings Fabrication	Solvent bench	11	1min Ace, 1min Iso, 1min DI, N2 dry	
		12	Dehydration bake on hotplate at ≥110 °C for ≥2', cool 1'	
	Asher #2	13	Plasma treatment (100W, 300mT Oxygen) for 1'	**Remove charge for better adhesion**
	PR Bench	14	Spin CSAR 1:1, 3kpm, 10kpm/s,30s	Using microfilter when dropping the CSAR
	Hot plate (with heater) ~4-5hrs	15	Hard bake 180C for 5 min	
	Ebeam lithography	16	Using the recipe#ITO-etch on ebeam lithography tool, use the holder 2E	It will take a long time (at least 5+ hours to write the whole piece)
Grating Development	Solvent bench	17	Development the grating in the solution MIKB:IPA 3:1 for 60s, and then immediately move to MIBK:IPA 9:1 solution for another 30s	Make sure the development solution is used within 5mins of mixture
Ridge Formation and SiO2 Deposition				
Ridges Litho	Solvent bench	18	3' Ace, 3' Iso, 2' DI (sonicate on high) N2 dry	
	PR Bench	19	Dehydration bake on hotplate at ≥110 °C for ≥2', cool 1'	
		20	Spin **LOL 2000**, 2 krpm, 10 krpm/s, 30s (~250 nm thick)	mount small samples on blue tape
		21	Clean backside with EBR 100	if needed
		22	Bake on center of hotplate at **210 °C for 5'**, cool 1'	Actual center T ~194 °C
		23	Spin **955CM-1.8**, 3 krpm, 10 krpm/s, 30 s (~1.8 µm thick)	
		24	Clean backside with EBR 100	if needed
		25	Soft bake on hotplate **95 °C for 90 s**	
	Stepper #2 (30'+)	26	Load mask #1 TOPNV2 RIDGES	
		27	Load sample onto 2" 500 µm chuck with 180 µm shim	keep track of orientation sample was loaded in
		28	"EDIT TOPNV2" Check: die size and column number	verify key offset, pass shift
		29	"EXEC TOPNV2", PASS: "RIDGES"	
		30	Expose 0.75 s, focus = -1	
	PR Bench	31	Post-exposure bake on hotplate at **110 °C for 90 s**	

	Develop Bench	32	Develop in **726MIF for 65 s**, DI Rinse, N2 dry	
	Microscope	33	Inspect (0.3-0.5 um undercut on LOL 2000) develop more if necessary	
	UV Ozone	34	1200 s (~6 Å/min)	
Ridges Etch	RIE #5 (2+ hr)	35	Load bare carrier wafer	
		36	Run DAN_01 O2 clean: 20.5 sccm, 10', 5 mTorr, 150 W RF; BCl3/Cl2 pretreat: 20.5 sccm BCl3, 5.2 sccm Cl2, 3', 10 mTorr, 15 W RF; Cl2 etch conditions: 10.2 sccm, 2', 5mTorr, 200 W RF	no He cooling
		37	Repeat DAN_01 if desired	
		38	Load sample onto carrier wafer (no mounting oil)	
		39	Set etch depth in DAN_05 (etc rate 120nm/min typical etch is 600nm) Run DAN_05 BCl3 pretreat: 10 sccm, 10', 2', 10 mTorr, 100 W RF; Cl2 Etch: 10 sccm, 5', 5 mTorr, 200 W RF	
		40	Soak sample in DI water, N2 dry	optional
	Microscope	41	Inspect	
SiO2 Dep & Liftoff	Sputter #3 (3+ hr, start at same time as RIE)	42	Load silicon calibration piece	
		43	Login: Earl Check and run recipe: COH_Ratetestdep for 2100'' (35')	
	Ellipsometer	44	Measure SiO2 on Si calibration thickness and index	should be ~ 125 nm (dark blue colored), n=1.47
	Sputter #3	45	Load sample(s) with silicon monitor	
		46	Calculate dep time for 225 nm SiO2. Update and run recipe: COH_SiO2 Sidewall Dep	
	Ellipsometer	47	Measure SiO2 on Si monitor thickness and index	should be ~ 225 nm (gold colored), n=1.47
	Solvent bench	48	Soak sample in NMP pre-heated to 80 °C for 15'	optional: place sample face-down in beaker
		49	Move sample to 2nd NMP pre-heated to 80 °C	

		50	Sonicate in bath at frequency: 8, intensity: 8, power: low, time 1-2min	
		51	swish for 30'' Iso, 30'' DI, N2 dry	
		52	Inspect, repeat steps 37–40 if necessary	use flouroscope
ITO Isolation Etch Litho	Solvent bench	53	1min Ace, 1min Iso, 1min DI, N2 dry	
	PR Bench	54	Dehydration bake on hotplate 110C 2min, let cool 1min	
		55	Spin **HMDS**, 3 krpm, 10 krpm/s, 30 s (let HMDS sit for 20s before spinning)	
		56	Spin **AZnLOF2020**, 3 krpm, 10 krpm/s, 30 s (~2.1 µm thick)	
		57	Clean backside of sample with EBR 100	
		58	Bake on hotplate at 110 °C for 90 s	
	Stepper ~30 mins	59	Load mask #2 - TOPNV2 PCONTS	
		60	Load sample onto 2" 500 µm chuck with 180 µm shim	
		61	Run "EX TOPNV2"	
		62	Pass: ITO	
		63	Stepper 2: Expose **0.2** s, focus **-6**,	Verify
	PR Bench	64	Post-exposure bake on hotplate at 110 °C for 60 s	
	Develop bench	65	Develop in AZ300MIF for 60 s	
		66	30 s x 3 rinse & dump DI, N2 dry	
	Microscope	67	Inspect, develop more if necessary	Visual check:
	UV Ozone	68	20 min (~6 Å/min)	
	Dektak	69	Dektak CONTACTS pad	Dektak pad:
(optional) ITO Isolation Etch	RIE #2 ~3hrs	70	Vent, use an Iso soaked wipe to clean chamber walls, top plate and platen	
		71	Pump down the chamber (DO NOT load samples)	
		72	O_2 clean > 30 min: 20 sccm O2, 125 mT, 500 V	
		73	MHA coat = 20 min: 4/20/10 sccm M/H/A, 75 mT, 500 V	
		74	Vent, load samples	
		75	MHA etch = 10 min (17 nm/min, 20% overetch): 4/20/10 sccm M/H/A, 75 mT, 350V	maybe insert weak 45' o2 etch after

				5 mins of MHA etching
		76	O_2 *in situ* descum = 10 min: 20 sccm O2, 125 mT, 300 V[f]	
	Solvent bench	77	Strip PR in NMP heated to 80 °C for 30+ min, agitate with pipette (it will take a long time to remove negative resist exposed to a dry etch)	
		78	Move sample to fresh beaker of NMP	
		79	Soak sample in NMP heated to 80 °C for 2 min, agitate with pipette	
		80	2 min Iso, 2 min DI, N2 dry	
	Microscope	81	Inspect carefully (PR is difficult to remove), repeat NMP and use ultrasonics on 'low' if necessary	
P-Pad Formation				
Contact Pads Litho	Solvent clean	82	2' in each ACE/ISO/DI swishing	
	PR Bench	83	Dehydration bake on hotplate ≥110 °C ≥2', cool 1'	
		84	Spin **HMDS**, 3 krpm, 10 krpm/s, 30 s (let HMDS sit for 20 s before spinning)	
		85	Spin **OCG825**, 3 krpm, 10 krpm/s, 30 s (~1.5 µm thick)	
		86	Clean backside of sample with EBR 100	
		87	Bake on hotplate at **95 °C for 2'**	
	MJB-3 aligner	88	Load sample onto one of the black chucks	
		89	Flood expose 1 s	
		90	Let sample outgas for 5' (VERY IMPORTANT)	
	PR Bench	91	Bake on hotplate at **95 °C for 2'** let cool 1'	
		92	Spin **955CM-1.8**, 3 krpm, 10 krpm/s, 30 s (~1.8 µm thick)	
		93	Clean backside with EBR 100	if needed
		94	Softbake on hotplate at **95 °C for 90 s**	
		95	Load mask #3 - TOPNV2 PADS	
		96	Load sample onto 2" 500 µm chuck with 180 µm shim	

	Stepper #2	97	"EDIT TOPNV2" Check: die size, column number, right alignment die position	
	(30+')	98	"EXEC TOPNV2", PASS: "PCONTS"	no pass shift
		99	Expose 0.4 s, focus= +2	
	Develop bench	100	Develop in **726MIF for 55-60s** (~2 µm undercut on OCG825), DI Rinse, N2 dry	
	Microscope	101	Inspect, develop more if necessary	
	UV Ozone	102	1200 s (~6 Å/min)	
p-Pad Dep	E-Beam #3 (2+ hr)	103	Deposit 150/10,000 Å Ti/Au	more gold could be better, 1 um is ebeam 3 limit
	Solvent bench	104	Place upside-down in NMP heated to 80 °C for 10'	
		105	Liftoff using pipette agitation	
		106	swish for 1' Iso, 1' DI, N2 dry	
	Microscope	107	Inspect, repeat steps 91-93 if necessary	
C+ Facet Formation				
C+ Facets Litho	Solvent bench	129	2' in each ACE/ISO/DI swishing	
	PR Bench	130	Dehydration bake on hotplate at ≥110 °C for ≥2', cool 1'	
		131	Spin **HMDS**, 3.5 krpm, 10 krpm/s, 45 s	
		132	Spin **SPR220-7.0**, 3.5 krpm, 10 krpm/s, 45 s (~6 µm thick)	
		133	Clean backside with EBR 100	if needed
		134	Soft bake on hotplate **115 °C for 120 s**	
	Stepper #2	135	Load mask #4 TOPNV2 CAIBE	
	(30+')	136	Load sample onto 2" 500 µm chuck with 180 µm shim	
		137	"EDIT TOPNV2" Check: die size, column number, right alignment die position	
		138	Under CAIBE pass, Y Pass Shift = +0.015 (first etch, shifts pattern DOWN and exposes the c+)	Adjust pass shift if p-pad alignment was off by more than 500 nm in Y. Must align to metal in Y
		139	"EXEC TOPNV2", Pass: "CAIBE"	
		140	Expose 1.35 s, focus= -1	
	PR Bench	141	Let sample **outgas for 35'** IMPORTANT	preheat the hotplates at 50 °C and 115 °C

	PR Bench	142	Post-exposure bake on hotplate at **50 °C for 60 s**, then immediately move to **115 °C for 90 s**	
	Develop Bench	143	Develop in **726MIF for 120 s**, DI rinse, N2 dry	Develop longer if PR residue seen (up to 4 mins is OK)
	Microscope	144	Inspect lithography. Check that facets mask aligned in y does not expose any metal. Check that it is the C+ side that is exposed for etching first	
	UV Ozone	145	1200 s (~6 Å/min)	
SiO2 Wet Etch1	Acid Bench	146	Etch piece of Si Monitor #1 in BHF (~200 nm/min)	
		147	Inspect monitor for hydrophobicity every 10-15s, record total etch time (should take 50 s – 1')	
		148	Etch sample in BHF for double the monitor etch time, DI rinse, N2 dry	
C+ Facets Etch	Oxford Ion Mill (3+ hr)	149	Mount samples on chuck with Cu tape such that facets to be etched (c+ side) face LHS	when chuck is mounted into system, it rotates 180°, so the facets will then face the beam
		150	Run: "Speck-Std_Ar_Cl2_3min_norotate_15x" 45', 15x3' etch steps with 14x5' cool steps ; Gases: Ar 5 sccm to Neutralizer; Ar 10 sccm to Beam; Cl2 20 sccm to Chamber; Beam etch source 200 mA Neutralizer, 200 W RF, 150 mA, 250 Vb, 500 Va; Platen drive "Posn", Platen "Cool" 10 C chiller, Chamber "heat" 40 C	etch rate 50-60 nm/min cools substrate and heats chamber walls
		151		
	Solvent bench	152	Strip mask in NMP heated to 80 °C for 10+', agitate with pipette	place sample upside-down in beaker
		153	Move sample to fresh beaker of NMP	
		154	Soak sample in NMP heated to 80 °C for 2', agitate with pipette	
		155	swish for 30'' Iso, 30'' DI, N2 dry	
	Microscope	156	Inspect that the surface is clean and that the correct side has been etched	
	Laser Microscope	157	Confirm the etch depth and profile	
C- Facet Formation				

C- Facets Litho	Solvent bench	158	1' Ace, 1' Iso, 1' DI, N2 dry	
	PR Bench	159	Dehydration bake on hotplate at ≥110 °C for ≥2', cool 1'	
		160	Spin **HMDS**, 3.5 krpm, 10 krpm/s, 45 s	
		161	Spin **SPR220-7.0**, 3.5 krpm, 10 krpm/s, 45 s (~6 µm thick)	
		162	Clean backside with EBR 100	if needed
		163	Soft bake on hotplate **115 °C for 120 s**	
	Stepper #2 (30+ min)	164	Load mask #4 TOPNV2 CAIBE	
		165	Load sample onto 2" 500 µm chuck with 180 µm shim	
		166	"EDIT TOPNV2" Check: die size, column number, right alignment die position	
		167	Under CAIBE pass, Y Pass Shift = -0.015 (2nd etch, shifts pattern DOWN and exposes the c-)	Adjust pass shift if p-pad alignment was off by more than 500 nm in Y. Must align to metal in Y
		168	"EXEC TOPNV2", Pass: "CAIBE"	
		169	Expose 1.35 s, focus= -1	
	PR Bench	170	Let sample **outgas for 35'** IMPORTANT	preheat the hotplates at 50 °C and 115 °C
	PR Bench	171	Post-exposure bake at **50 °C for 60 s**, then immediately move to **115 °C for 90 s**	
	Develop Bench	172	Develop in **726MIF for 120 s**, DI rinse, N2 dry	may need to dev more, 3-4 mins is ok
	Microscope	173	Inspect lithography. Check that facets mask aligned in y does not expose any metal. Check that it is the c- side that is exposed for etching	some resist in corners is normal NOT IN FRONT OF FACET
	UV Ozone	174	1200 s (~6 Å/min)	
SiO2 Wet Etch2		175	Etch piece of Si Monitor #2 in BHF (~200 nm/min)	
	Acid Bench	176	Inspect monitor for hydrophobicity every 10-15s, record total etch time (should take 50 s – 1')	
		177	Etch sample in BHF for double the monitor etch time, DI rinse, N2 dry	

C- Facets Etch	Oxford Ion Mill (3+ hr)	178	Mount samples on chuck with Cu tape such that facets to be etched (c- side) face LHS	(when chuck is mounted into system, it rotates 180°, so the facets will then face the beam)
		179	Run: "Speck-Std_Ar_Cl2_3min_norotate_15x" 45', 15x3' etch steps with 14x5' cool steps ;	etch rate 50-60 nm/min
	Solvent bench	180	Strip mask in NMP heated to 80 °C for 10+', agitate with pipette	place sample upside-down in beaker
		181	Move sample to fresh beaker of NMP	
		182	Soak sample in NMP heated to 80 °C for 2', agitate with pipette	
		183	swish for 30'' Iso, 30'' DI, N2 dry	
	Microscope	184	Inspect that the surface is clean and that the correct side has been etched	
	Laser Microscope	185	Confirm the etch depth and profile	
N-Contact Formation				
N-contact Dep & Liftoff	PR Bench	186	Mount sample upside down on Si wafer with a drop of AZ 4110	
		187	Bake on hotplate at 105 °C for >5'	
	E-beam #3 (1+ hr)	188	Deposit 500/1000/3000 Å Al/Ni/Au Wait 5' after Ni dep before rotating turret to Au pocket	Al rate < 3 A/s. Ni necessary for heat sink soldering
	Solvent bench	189	Soak sample in NMP heated to 80 °C until sample detaches from Si wafer	place upside-down in beaker. Do not try to slide or pry samples off
		190	2' Iso, 2' DI, N2 dry	
	Microscope	191	Inspect, repeat NMP if necessary	
Preliminary Testing	Test lab		Test devices prior to facet coating or Cu soldering	
HR Back Facet Coating				
Sample Dice	Solvent bench	192	3' Ace, 2' Iso, 1' DI, N2 dry	
	Gasonics	193	Recipe 2, multiple runs if desired	
	PR Bench	195	Dehydration bake on hotplate 110 °C 2', let cool 1'	
		197	Spin **SPR-3.0**, 3 krpm, 10 krpm/s, 30 s (~1.5 µm thick)	
		198	Clean backside of sample with EBR 100	
		199	Bake on hotplate at **95 °C for 2'**, let cool 1'	
	Packaging Lab	194	Place the sample on a 140C hotplate with melting wax	

	Develop bench	212	Develop in **726MIF for 60 s** (~2 µm undercut on OCG825), DI rinse, N2 dry	
	Dicing saw	213	Dice the sample into halves	
	Heat bath	214	Put the diced bars into NMP for 10+ hours	
	Si bar attachment	212	Carefully move the Silicon bar onto the laser bar and cover one side of the facet	
	Microscope	213	Observe to make sure that the other facet is not covered by any wax	
	ISO dip	214	Put the diced bars into Iso for 10 min	Clean any dusts/residues on the facets
Ge wet etch	Veeco IBD	217	Nakamura 12, pwd: "nitrides"	FACET COAT IS NOT STABLE
		218	Calibrate SiO2 dep rate on Si for 1200'' (tilt and rotate throughout), measure n and t in ellipsometry	~0.8 A/s, n=1.47
IBD cals		219	Calibrate Ta2O5 dep rate on Si for 1200'', measure n and t in ellipsometry	~1.2 A/s, n=2.27
		220	Calibrate SiO2-centered fabry-perot (λ/4n Ta2O5, λ/2n SiO2, λ/4n Ta2O5)	"12_LD_SiO2_FP_3PD_45deg"
	Filmetrics	221	Measure R vs. λ, "notch" is at λ/2n, adjust the SiO2 time for the refined dep rate	Repeat if off by >5nm
	Veeco IBD	222	Calibrate Ta2O5-centered fabry-perot (λ/4n SiO2, λ/2n Ta2O5, λ/4n SiO2)	"12_LD_Ta2O5_FP_3PD_45deg"
	Filmetrics	223	Measure R vs. λ and adjust Ta2O5 time	Repeat if off by >5nm
	Veeco IBD	224	Load samples the sample direction is very important(has to be perpendicular to the beam)	
		225	Calculate new dep times to account for field vs facet coverage ratio for 45 ° platen angle: SiO2 time = 1.55*(calibrated SiO2 time); Ta2O5 time = 2.30*(calibrated Ta2O5 time); grid cleans 15' in the beginning and 5' in between steps NOTE: Facet Coatings have had problems 2015-2016, consider process in BETA	HR coatings: start periods with λ/4n SiO2 then λ/4n Ta2O5
Back Facet Coating		226	Set number of periods (normally 5–8), run recipe	2 um facet etch depth allows for ~5 period DBR
	Solvent bench	227	Liftoff in NMP heated to 80 °C for 10+', agitate with pipette	
		228	Move sample to fresh beaker of NMP	

		229	Soak sample in NMP heated to 80 °C for 2', agitate with pipette	
		230	2' Iso, 2' DI, N2 dry	
	Microscope	231	Inspect, repeat NMP if necessary	
	Solvent bench	232	1' Ace, 1' Iso, 1' DI, N2 dry	
	PR Bench	233	Dehydration bake on hotplate ≥110 °C 2', let cool 1'	
Front Facet Coating		258	Set number of periods (normally 2 – 3 for HR/HR coating or single SiO2 for AR coating), run recipe	AR coatings: SiO2 single layer
	Si bar attachment	212	Carefully move the Silicon bar onto the laser bar and cover the other side of the facet	
	Microscope	213	Observe to make sure that the other facet is not covered by any wax	
	ISO dip	214	Put the diced bars into Iso for 10 min	Clean any dusts/residues on the facets
	Solvent bench	259	Liftoff in NMP heated to 80 °C for 10+', agitate with pipette	
		260	Move sample to fresh beaker of NMP	
		261	Soak sample in NMP heated to 80 °C for 2', agitate with pipette	
		262	2' Iso, 2' DI, N2 dry	
	Microscope	263	Inspect, repeat NMP if necessary	
Cu Heat Sink Mounting (Before testing CW)				
Heat Sink Mounting	Packaging Lab Dissecting Microscope	264	Materials: heater and probe mount, wide Cu stub mount, screw for stub, Pb Sn Ag solder foils, superior flux #3- (glutamic acid, HCl), optical table screws, razor blade, Q-tips	For cw testing. Parts in drawer to right of microscope
		265	file Cu stub to size of substrate with 400 grit sandpaper	
		266	screw down heater and probe setup to scope stage	
		267	screw stub to heater	
		268	place sized solder foil on stub and press foot pedal to start heater and melt foil, use some flux to help	takes ~90 s to heat up
		269	scrape solder and reflow until it stops migrating	remove foot from pedal because takes a while to cool

		270	let cool, add some more flux, then add sample	
		271	use probe mount to push down on the LD sample in the center of pattern to hold it in place	
		272	heat until reflow and wets, let cool	

B. Second generation of DFB-LDs with embedded surface grating

Step	Equipment	#	Process Step	Notes
Surface Clean and Reactivation				
Remove Indium	Acid Bench	1	1:3 HNO_3:HCl (aqua regia) hotplate at 225 °C, 5-10' repeat 2x	Mix HCl & HNO_3, bring to boil, then add sample
Clean	Solvent bench	2	(Optional) Scrub samples in tergitol with swabs to get rid of any residual scum	
	Solvent bench	3	3' Ace, 3' Iso, 2' DI (sonicate on high) N2 dry	
Reactivate	RTA	4	Reactivate 15' at 600 °C N2/O2 (or use MOCVD lab furnace 600C 15 min N2/O2)	
First layer of ITO deposition				
ITO Deposition	Solvent bench	5	1min Ace, 1min Iso, 1min DI, N2 dry	
		6	Dehydration bake on hotplate at ≥110 °C for ≥2', cool 1'	
	UV Ozone	7	1200 s (~6 Å/min)	
	Acid Bench	8	Etch sample in HCL 15 mins	Removes Oxide, Do immediatley prior to ITO dep
	E Beam #2 (with heater) ~4-5hrs	9	Deposit 10 nm ITO with Si monitor Temp using 2-step temperature techqniue, first deposit 6 nm ITO at 50C and then immediately increase the temperatute to depostion another 6 nm 330C max (current heater set to **800C**) O2 flow: starting from~30sccm and ramp up to 45 sccm Tooling: **69.9-76** for accurate dep rate Keep the dep rate less than 0.1 A/s	Si Monitor #2

	Ellipsometer & AFM	10	Measure Si Monitor #2 thickness (Using model ITO-new) and make sure the RMS of the surface less than 1nm	Thickness:
Grating formation				
Gratings Fabrication	Solvent bench	11	1min Ace, 1min Iso, 1min DI, N2 dry	
		12	Dehydration bake on hotplate at ≥110 °C for ≥2', cool 1'	
	Asher #2	13	Plasma treatment (100W, 300mT Oxygen) for 1'	**Remove charge for better adhesion**
	PR Bench	14	Spin HSQ 2%, 3kpm, 10kpm/s,30s	Using microfilter when dropping the CSAR
	Hot plate (with heater) ~4-5hrs	15	Softbake 90C for 1 min	
	Ebeam lithography	16	Using the recipe#ITO-embedded on ebeam lithography tool, use the holder 2E	It will take a long time (at least 5+ hours to write the whole piece)
Grating Development	Solvent bench	17	Development the grating in the 25% TMAH solution for 60s	Make sure the development solution is used within 5mins of mixture
Second layer of ITO deposition				
ITO Deposition	Solvent bench	5	1min Ace, 1min Iso, 1min DI, N2 dry	
		6	Dehydration bake on hotplate at ≥110 °C for ≥2', cool 1'	
	UV Ozone	7	1200 s (~6 Å/min)	
	Acid Bench	8	Etch sample in HCL 15 mins	Removes Oxide, Do immediatley prior to ITO dep

	E Beam #2 (with heater) ~4-5hrs	9	Deposit 150 nm ITO with Si monitor Temp using 2-step temperature techqniue, first deposit 12 nm ITO at 50C and then immediately increase the temperatute to depostion another 6 nm 330C max (current heater set to **800C**) O2 flow: starting from~30sccm and ramp up to 45 sccm Tooling: **69.9-76** for accurate dep rate Keep the dep rate less than 0.1 A/s	Si Monitor #2
	Ellipsometer & AFM	10	Measure Si Monitor #2 thickness (Using model ITO-new) and make sure the RMS of the surface less than 1nm	Thickness:
Ridge Formation and SiO2 Deposition				
Ridges Litho	Solvent bench	18	3' Ace, 3' Iso, 2' DI (sonicate on high) N2 dry	
	PR Bench	19	Dehydration bake on hotplate at ≥110 °C for ≥2', cool 1'	
		20	Spin **LOL 2000**, 2 krpm, 10 krpm/s, 30s (~250 nm thick)	mount small samples on blue tape
		21	Clean backside with EBR 100	if needed
		22	Bake on center of hotplate at **210 °C for 5'**, cool 1'	Actual center T ~194 °C
		23	Spin **955CM-1.8**, 3 krpm, 10 krpm/s, 30 s (~1.8 µm thick)	
		24	Clean backside with EBR 100	if needed

		25	Soft bake on hotplate **95 °C for 90 s**	
	Stepper #2 (30'+)	26	Load mask #1 TOPNV2 RIDGES	
		27	Load sample onto 2" 500 µm chuck with 180 µm shim	keep track of orientation sample was loaded in
		28	"EDIT TOPNV2" Check: die size and column number	verify key offset, pass shift
		29	"EXEC TOPNV2", PASS: "RIDGES"	
		30	Expose 0.75 s, focus = -1	
	PR Bench	31	Post-exposure bake on hotplate at **110 °C for 90 s**	
	Develop Bench	32	Develop in **726MIF for 65 s**, DI Rinse, N2 dry	
	Microscope	33	Inspect (0.3-0.5 um undercut on LOL 2000) develop more if necessary	
	UV Ozone	34	1200 s (~6 Å/min)	
Ridges Etch	RIE #5 (2+ hr)	35	Load bare carrier wafer	
		36	Run DAN_01 O2 clean: 20.5 sccm, 10', 5 mTorr, 150 W RF; BCl3/Cl2 pretreat: 20.5 sccm BCl3, 5.2 sccm Cl2, 3', 10 mTorr, 15 W RF; Cl2 etch conditions: 10.2 sccm, 2', 5mTorr, 200 W RF	no He cooling
		37	Repeat DAN_01 if desired	

		38	Load sample onto carrier wafer (no mounting oil)	
		39	Set etch depth in DAN_05 (etc rate 120nm/min typical etch is 600nm) Run DAN_05 BCl3 pretreat: 10 sccm, 10', 2', 10 mTorr, 100 W RF; Cl2 Etch: 10 sccm, 5', 5 mTorr, 200 W RF	
		40	Soak sample in DI water, N2 dry	optional
	Microscope	41	Inspect	
SiO2 Dep & Liftoff	Sputter #3 (3+ hr, start at same time as RIE)	42	Load silicon calibration piece	
		43	Login: Earl Check and run recipe: COH_Ratetestdep for 2100'' (35')	
	Ellipsometer	44	Measure SiO2 on Si calibration thickness and index	should be ~ 125 nm (dark blue colored), n=1.47
	Sputter #3	45	Load sample(s) with silicon monitor	
		46	Calculate dep time for 225 nm SiO2. Update and run recipe: COH_SiO2 Sidewall Dep	
	Ellipsometer	47	Measure SiO2 on Si monitor thickness and index	should be ~ 225 nm (gold colored), n=1.47
	Solvent bench	48	Soak sample in NMP pre-heated to 80 °C for 15'	optional: place sample face-down in beaker

		49	Move sample to 2nd NMP pre-heated to 80 °C	
		50	Sonicate in bath at frequency: 8, intensity: 8, power: low, time 1-2min	
		51	swish for 30'' Iso, 30'' DI, N2 dry	
		52	Inspect, repeat steps 37–40 if necessary	use flouroscope
ITO Isolation Etch Litho	Solvent bench	53	1min Ace, 1min Iso, 1min DI, N2 dry	
	PR Bench	54	Dehydration bake on hotplate 110C 2min, let cool 1min	
		55	Spin **HMDS**, 3 krpm, 10 krpm/s, 30 s (let HMDS sit for 20s before spinning)	
		56	Spin **AZnLOF2020**, 3 krpm, 10 krpm/s, 30 s (~2.1 µm thick)	
		57	Clean backside of sample with EBR 100	
		58	Bake on hotplate at 110 °C for 90 s	
	Stepper ~30 mins	59	Load mask #2 - TOPNV2 PCONTS	
		60	Load sample onto 2" 500 µm chuck with 180 µm shim	
		61	Run "EX TOPNV2"	
		62	Pass: ITO	
		63	Stepper 2: Expose **0.2** s, focus **-6**,	Verify
	PR Bench	64	Post-exposure bake on hotplate at 110 °C for 60 s	
	Develop bench	65	Develop in AZ300MIF for 60 s	
		66	30 s x 3 rinse & dump DI, N2 dry	
	Microscope	67	Inspect, develop more if necessary	Visual check:
	UV Ozone	68	20 min (~6 Å/min)	
	Dektak	69	Dektak CONTACTS pad	Dektak pad:
	RIE #2 ~3hrs	70	Vent, use an Iso soaked wipe to clean chamber walls, top plate and platen	

(optional) ITO Isolation Etch		71	Pump down the chamber (DO NOT load samples)	
		72	O_2 clean > 30 min: 20 sccm O2, 125 mT, 500 V	
		73	MHA coat = 20 min: 4/20/10 sccm M/H/A, 75 mT, 500 V	
		74	Vent, load samples	
		75	MHA etch = 10 min (17 nm/min, 20% overetch): 4/20/10 sccm M/H/A, 75 mT, 350V	maybe insert weak 45' o2 etch after 5 mins of MHA etching
		76	O_2 *in situ* descum = 10 min: 20 sccm O2, 125 mT, 300 V[f]	
	Solvent bench	77	Strip PR in NMP heated to 80 °C for 30+ min, agitate with pipette (it will take a long time to remove negative resist exposed to a dry etch)	
		78	Move sample to fresh beaker of NMP	
		79	Soak sample in NMP heated to 80 °C for 2 min, agitate with pipette	
		80	2 min Iso, 2 min DI, N2 dry	
	Microscope	81	Inspect carefully (PR is difficult to remove), repeat NMP and use ultrasonics on 'low' if necessary	
P-Pad Formation				
Contact Pads Litho	Solvent clean	82	2' in each ACE/ISO/DI swishing	

	PR Bench	83	Dehydration bake on hotplate ≥110 °C ≥2', cool 1'	
		84	Spin **HMDS**, 3 krpm, 10 krpm/s, 30 s (let HMDS sit for 20 s before spinning)	
		85	Spin **OCG825**, 3 krpm, 10 krpm/s, 30 s (~1.5 µm thick)	
		86	Clean backside of sample with EBR 100	
		87	Bake on hotplate at **95 °C for 2'**	
	MJB-3 aligner	88	Load sample onto one of the black chucks	
		89	Flood expose 1 s	
		90	Let sample outgas for 5' (VERY IMPORTANT)	
	PR Bench	91	Bake on hotplate at **95 °C for 2'** let cool 1'	
		92	Spin **955CM-1.8**, 3 krpm, 10 krpm/s, 30 s (~1.8 µm thick)	
		93	Clean backside with EBR 100	if needed
		94	Softbake on hotplate at **95 °C for 90 s**	
		95	Load mask #3 - TOPNV2 PADS	
		96	Load sample onto 2" 500 µm chuck with 180 µm shim	

	Stepper #2 (30+')	97	"EDIT TOPNV2" Check: die size, column number, right alignment die position	
		98	"EXEC TOPNV2", PASS: "PCONTS"	no pass shift
		99	Expose 0.4 s, focus= +2	
	Develop bench	100	Develop in **726MIF for 55-60s** (~2 µm undercut on OCG825), DI Rinse, N2 dry	
	Microscope	101	Inspect, develop more if necessary	
	UV Ozone	102	1200 s (~6 Å/min)	
p-Pad Dep	E-Beam #3 (2+ hr)	103	Deposit 150/10,000 Å Ti/Au	more gold could be better, 1 um is ebeam 3 limit
	Solvent bench	104	Place upside-down in NMP heated to 80 °C for 10'	
		105	Liftoff using pipette agitation	
		106	swish for 1' Iso, 1' DI, N2 dry	
	Microscope	107	Inspect, repeat steps 91-93 if necessary	
C+ Facet Formation				
	Solvent bench	129	2' in each ACE/ISO/DI swishing	
	PR Bench	130	Dehydration bake on hotplate at ≥110 °C for ≥2', cool 1'	
		131	Spin **HMDS**, 3.5 krpm, 10 krpm/s, 45 s	
		132	Spin **SPR220-7.0**, 3.5 krpm, 10 krpm/s, 45 s (~6 µm thick)	

C+ Facets Litho		133	Clean backside with EBR 100	if needed
		134	Soft bake on hotplate **115 °C for 120 s**	
	Stepper #2 (30+')	135	Load mask #4 TOPNV2 CAIBE	
		136	Load sample onto 2" 500 µm chuck with 180 µm shim	
		137	"EDIT TOPNV2" Check: die size, column number, right alignment die position	
		138	Under CAIBE pass, Y Pass Shift = +0.015 (first etch, shifts pattern DOWN and exposes the c+)	Adjust pass shift if p-pad alignment was off by more than 500 nm in Y. Must align to metal in Y
		139	"EXEC TOPNV2", Pass: "CAIBE"	
		140	Expose 1.35 s, focus= -1	
	PR Bench	141	Let sample **outgas for 35'** IMPORTANT	preheat the hotplates at 50 °C and 115 °C
	PR Bench	142	Post-exposure bake on hotplate at **50 °C for 60 s**, then immediately move to **115 °C for 90 s**	

	Develop Bench	143	Develop in **726MIF for 120 s**, DI rinse, N2 dry	Develop longer if PR residue seen (up to 4 mins is OK)
	Microscope	144	Inspect lithography. Check that facets mask aligned in y does not expose any metal. Check that it is the C+ side that is exposed for etching first	
	UV Ozone	145	1200 s (~6 Å/min)	
SiO2 Wet Etch1	Acid Bench	146	Etch piece of Si Monitor #1 in BHF (~200 nm/min)	
		147	Inspect monitor for hydrophobicity every 10-15s, record total etch time (should take 50 s – 1')	
		148	Etch sample in BHF for double the monitor etch time, DI rinse, N2 dry	
C+ Facets Etch	Oxford Ion Mill	149	Mount samples on chuck with Cu tape such that facets to be etched (c+ side) face LHS	when chuck is mounted into system, it rotates 180°, so the facets will then face the beam
	(3+ hr)	150	Run: "Speck-Std_Ar_Cl2_3min_norotate_15x" 45', 15x3' etch steps with 14x5' cool steps ;	etch rate 50-60 nm/min

		151	Gases: Ar 5 sccm to Neutralizer; Ar 10 sccm to Beam; Cl2 20 sccm to Chamber; Beam etch source 200 mA Neutralizer, 200 W RF, 150 mA, 250 Vb, 500 Va; Platen drive "Posn", Platen "Cool" 10 C chiller, Chamber "heat" 40 C	cools substrate and heats chamber walls
	Solvent bench	152	Strip mask in NMP heated to 80 °C for 10+', agitate with pipette	place sample upside-down in beaker
		153	Move sample to fresh beaker of NMP	
		154	Soak sample in NMP heated to 80 °C for 2', agitate with pipette	
		155	swish for 30'' Iso, 30'' DI, N2 dry	
	Microscope	156	Inspect that the surface is clean and that the correct side has been etched	
	Laser Microscope	157	Confirm the etch depth and profile	
C- Facet Formation				
C- Facets Litho	Solvent bench	158	1' Ace, 1' Iso, 1' DI, N2 dry	
	PR Bench	159	Dehydration bake on hotplate at ≥110 °C for ≥2', cool 1'	
		160	Spin **HMDS**, 3.5 krpm, 10 krpm/s, 45 s	

		161	Spin **SPR220-7.0**, 3.5 krpm, 10 krpm/s, 45 s (~6 µm thick)	
		162	Clean backside with EBR 100	if needed
		163	Soft bake on hotplate **115 °C for 120 s**	
	Stepper #2 (30+ min)	164	Load mask #4 TOPNV2 CAIBE	
		165	Load sample onto 2" 500 µm chuck with 180 µm shim	
		166	"EDIT TOPNV2" Check: die size, column number, right alignment die position	
		167	Under CAIBE pass, Y Pass Shift = -0.015 (2nd etch, shifts pattern DOWN and exposes the c-)	Adjust pass shift if p-pad alignment was off by more than 500 nm in Y. Must align to metal in Y
		168	"EXEC TOPNV2", Pass: "CAIBE"	
		169	Expose 1.35 s, focus= -1	
	PR Bench	170	Let sample **outgas for 35'** IMPORTANT	preheat the hotplates at 50 °C and 115 °C

	PR Bench	171	Post-exposure bake at **50 °C for 60 s**, then immediately move to **115 °C for 90 s**	
	Develop Bench	172	Develop in **726MIF for 120 s**, DI rinse, N2 dry	may need to dev more, 3-4 mins is ok
	Microscope	173	Inspect lithography. Check that facets mask aligned in y does not expose any metal. Check that it is the c- side that is exposed for etching	some resist in corners is normal NOT IN FRONT OF FACET
	UV Ozone	174	1200 s (~6 Å/min)	
SiO2 Wet Etch2		175	Etch piece of Si Monitor #2 in BHF (~200 nm/min)	
	Acid Bench	176	Inspect monitor for hydrophobicity every 10-15s, record total etch time (should take 50 s – 1')	
		177	Etch sample in BHF for double the monitor etch time, DI rinse, N2 dry	
C- Facets Etch	Oxford Ion Mill (3+ hr)	178	Mount samples on chuck with Cu tape such that facets to be etched (c- side) face LHS	(when chuck is mounted into system, it rotates 180°, so the facets will then face the beam)
		179	Run: "Speck-Std_Ar_Cl2_3min_norotate_15x" 45', 15x3' etch steps with 14x5' cool steps ;	etch rate 50-60 nm/min
	Solvent bench	180	Strip mask in NMP heated to 80 °C for 10+', agitate with pipette	place sample upside-down in beaker
		181	Move sample to fresh beaker of NMP	

		182	Soak sample in NMP heated to 80 °C for 2', agitate with pipette	
		183	swish for 30'' Iso, 30'' DI, N2 dry	
	Microscope	184	Inspect that the surface is clean and that the correct side has been etched	
	Laser Microscope	185	Confirm the etch depth and profile	
N-Contact Formation				
N-contact Dep & Liftoff	PR Bench	186	Mount sample upside down on Si wafer with a drop of AZ 4110	
		187	Bake on hotplate at 105 °C for >5'	
	E-beam #3 (1+ hr)	188	Deposit 500/1000/3000 Å Al/Ni/Au Wait 5' after Ni dep before rotating turret to Au pocket	Al rate < 3 A/s. Ni necessary for heat sink soldering
	Solvent bench	189	Soak sample in NMP heated to 80 °C until sample detaches from Si wafer	place upside-down in beaker. Do not try to slide or pry samples off
		190	2' Iso, 2' DI, N2 dry	
	Microscope	191	Inspect, repeat NMP if necessary	
Preliminary Testing	Test lab		Test devices prior to facet coating or Cu soldering	

HR Back Facet Coating				
Sample Dice	Solvent bench	192	3' Ace, 2' Iso, 1' DI, N2 dry	
	Gasonics	193	Recipe 2, multiple runs if desired	
	PR Bench	195	Dehydration bake on hotplate 110 °C 2', let cool 1'	
		197	Spin **SPR-3.0**, 3 krpm, 10 krpm/s, 30 s (~1.5 µm thick)	
		198	Clean backside of sample with EBR 100	
		199	Bake on hotplate at **95 °C for 2'**, let cool 1'	
	Packaging Lab	194	Place the sample on a 140C hotplate with melting wax	
	Develop bench	212	Develop in **726MIF for 60 s** (~2 µm undercut on OCG825), DI rinse, N2 dry	
	Dicing saw	213	Dice the sample into halves	
	Heat bath	214	Put the diced bars into NMP for 10+ hours	
	Si bar attachment	212	Carefully move the Silicon bar onto the laser bar and cover one side of the facet	
	Microscope	213	Observe to make sure that the other facet is not covered by any wax	
	ISO dip	214	Put the diced bars into Iso for 10 min	Clean any dusts/residues on the facets

Ge wet etch	Veeco IBD	217	Nakamura 12, pwd: "nitrides"	FACET COAT IS NOT STABLE
		218	Calibrate SiO2 dep rate on Si for 1200'' (tilt and rotate throughout), measure n and t in ellipsometry	~0.8 A/s, n=1.47
IBD cals		219	Calibrate Ta2O5 dep rate on Si for 1200'', measure n and t in ellipsometry	~1.2 A/s, n=2.27
		220	Calibrate SiO2-centered fabry-perot (λ/4n Ta2O5, λ/2n SiO2, λ/4n Ta2O5)	"12_LD_SiO2_FP_3PD_45deg"
	Filmetrics	221	Measure R vs. λ, "notch" is at λ/2n, adjust the SiO2 time for the refined dep rate	Repeat if off by >5nm
	Veeco IBD	222	Calibrate Ta2O5-centered fabry-perot (λ/4n SiO2, λ/2n Ta2O5, λ/4n SiO2)	"12_LD_Ta2O5_FP_3PD_45deg"
	Filmetrics	223	Measure R vs. λ and adjust Ta2O5 time	Repeat if off by >5nm
		224	Load samples the sample direction is very important(has to be perpendicular to the beam)	

	Veeco IBD	225	Calculate new dep times to account for field vs facet coverage ratio for 45 ° platen angle: SiO2 time = 1.55*(calibrated SiO2 time); Ta2O5 time = 2.30*(calibrated Ta2O5 time); grid cleans 15' in the beginning and 5' in between steps NOTE: Facet Coatings have had problems 2015-2016, consider process in BETA	HR coatings: start periods with λ/4n SiO2 then λ/4n Ta2O5
Back Facet Coating		226	Set number of periods (normally 5–8), run recipe	2 um facet etch depth allows for ~5 period DBR
	Solvent bench	227	Liftoff in NMP heated to 80 °C for 10+', agitate with pipette	
		228	Move sample to fresh beaker of NMP	
		229	Soak sample in NMP heated to 80 °C for 2', agitate with pipette	
		230	2' Iso, 2' DI, N2 dry	
	Microscope	231	Inspect, repeat NMP if necessary	
	Solvent bench	232	1' Ace, 1' Iso, 1' DI, N2 dry	
	PR Bench	233	Dehydration bake on hotplate ≥110 °C 2', let cool 1'	
Front Facet Coating		258	Set number of periods (normally 2 – 3 for HR/HR coating or single SiO2 for AR coating), run recipe	AR coatings: SiO2 single layer

	Si bar attachment	212	Carefully move the Silicon bar onto the laser bar and cover the other side of the facet	
	Microscope	213	Observe to make sure that the other facet is not covered by any wax	
	ISO dip	214	Put the diced bars into Iso for 10 min	Clean any dusts/residues on the facets
	Solvent bench	259	Liftoff in NMP heated to 80 °C for 10+', agitate with pipette	
		260	Move sample to fresh beaker of NMP	
		261	Soak sample in NMP heated to 80 °C for 2', agitate with pipette	
		262	2' Iso, 2' DI, N2 dry	
	Microscope	263	Inspect, repeat NMP if necessary	
Cu Heat Sink Mounting (Before testing CW)				

Heat Sink Mounting	Packaging Lab Dissecting Microscope	264	Materials: heater and probe mount, wide Cu stub mount, screw for stub, Pb Sn Ag solder foils, superior flux #3- (glutamic acid, HCl), optical table screws, razor blade, Q-tips	For cw testing. Parts in drawer to right of microscope
		265	file Cu stub to size of substrate with 400 grit sandpaper	
		266	screw down heater and probe setup to scope stage	
		267	screw stub to heater	
		268	place sized solder foil on stub and press foot pedal to start heater and melt foil, use some flux to help	takes ~90 s to heat up
		269	scrape solder and reflow until it stops migrating	remove foot from pedal because takes a while to cool
		270	let cool, add some more flux, then add sample	
		271	use probe mount to push down on the LD sample in the center of pattern to hold it in place	
		272	heat until reflow and wets, let cool	